UNIVERSITÀ DEGLI STUDI DI PADOVA

DIPARTIMENTO DI FISICA E ASTRONOMIA "G. GALILEI"

Corso di laurea magistrale in Astronomia

Tesi di Laurea Magistrale

GAS ACCRETION AND COUNTER-ROTATION IN DISK GALAXIES: N-BODY SIMULATIONS OF MERGERS WITH A DWARF GALAXY

Relatore: Prof. Alessandro Pizzella
Correlatrice: Dott.ssa Michela Mapelli

Laureando: Matteo Mazzarini
Matricola: 1084440

Anno Accademico 2015/2016

Contents

Chapter 1

Counter-rotation in disk galaxies and minor merger between a disk galaxy and a dwarf galaxy

Counter-rotation consists in the presence of two components of the same galaxy having opposite angular momenta projected on the sky. In many cases, the two angular momenta are found to be intrinsically anti-parallel to each other, so counter-rotation is really present in these galaxies. In other situations, it happens that the two components are not completely aligned and counter-rotation is not perfect (Bertola & Corsini 1999; Corsini 2014). If there is counter-rotation between two components in a galaxy, the one with the largest mass is the *prograde* component and it dictates the general sense of rotation of the galaxy. The other one is the *retrograde* component, it is less massive and it counter-rotates with respect to the prograde component. Counter-rotation was first discovered in the elliptical galaxies NGC 5898 (Bettoni 1984) and NGC 7097 (Caldwell et al. 1986), but it is only since the discovery of counter-rotation in the SB0 galaxy NGC 4546 (Galletta 1987) that further investigation has been made on this process.

In this thesis I will focus on counter-rotation in disk galaxies only. Disk galaxies include lenticuar type (S0) galaxies and spiral type (S) galaxies. More precisely, spiral galaxies can in turn be divided in S0/a, Sa, Sb, Sc and Sd galaxies. Intermediate classifications between these types are possible. For details about counter-rotation in elliptical galaxies, I refer the reader to the reviews by Rubin (1994b), Galletta (1996) and Bertola & Corsini (1999).

1.1 Forms and radial extension of counter-rotation

1.1.1 Forms of counter-rotation

Counter-rotation can involve gaseous and stellar components (Bertola & Corsini 1999; Corsini 2014). In some cases, two gaseous components only (*gas-versus-gas* couter-rotation) or two stellar components only (*stars-versus-stars* counter-rotation) are found

to be kinematically decoupled, while in other cases both types of component can be involved (*gas-versus-stars* counter-rotation).

- **gas-versus-stars counter-rotation:** this happens when a gaseous component and a stellar component in a galaxy have opposite angular momenta. An example is the SB0 galaxy NGC 4546 (Figure 1.1). As said above, this galaxy was the first disk galaxy in which counter-rotation was discovered. Galletta (1987) performs long-slit spectroscopic observations with the slit put along different position angles (PAs). He concludes that there is a gaseous disk counter-rotating with respect to the stellar disk.

- **stars-versus-stars counter-rotation:** this is the case in which two stellar components in a galaxy have opposite angular momenta. An example is provided with NGC 4550 (Figure 1.2). This is an E7/S0 galaxy (Sandage & Tammann 1981; de Vaucouleurs et al. 1991 classify it as SB0 uncertain). The kinematics of this galaxy is extremely interesting. By means of spectroscopic observations along the major axis of the galaxy, Rubin et al. (1992) analyze the kinematics of gaseous and stellar component in the inner 30% of the radial extension of the optical disk. They find that, apart from the prograde stellar disk, there is a secondary stellar component which counter-rotates with respect to it and that co-rotates with the retrograde gas disk. Another case of two disks of stars that counter-rotate in a galaxy is represented by NGC 7217. For this case, I refer the reader to Merrifield & Kuijken (1994).

- **gas-versus-gas counter-rotation:** this happens when two gaseous components have opposite angular momenta in the same galaxy (Figure 1.4). NGC 7332 is an example of galaxy in which two gaseous components counter-rotate with respect to each other. Fisher et al. (1994) perform spectroscopy observations of gas and stars along different PAs on the projected galactic disk. The kinematics of gas and stars obtained along the major axis (PA = 155°, 158°) unveils the presence of two gaseous components: one co-rotates with the main stellar component, the other counter-rotates with respect to it.

1.1.2 Radial extension of counter-rotation

In general, counter-rotation involves structures with a variety of radial extensions within a galaxy. This means that we can find counter-rotation in the *inner regions*, in the *outer regions* or *overall* the host galaxy (Bertola & Corsini 1999; Corsini 2014).

- **counter-rotation in the inner regions of the galaxy:** this is the case in which an inner structure - a nuclear disk, an inner ring or a small-scale disk - counter-rotates with respect to the main disk component of the galaxy. This case is well represented by NGC 3593. Bertola et al. (1996) perform both major-axis spectroscopy observations and photometry observations of the galaxy (Figure 1.3). The analysis of the kinematics of the galaxy along its major axis reveals

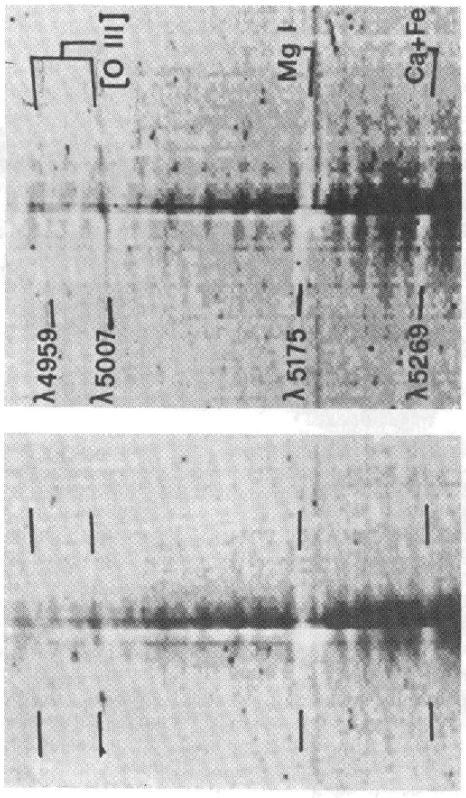

Figure 1.1: Long-slit spectra of NGC 4546 (Galletta 1987). For both figures, the direction of dispersion (i.e. along wavelengths; in Å) is the horizontal one (increasing from left to right), while the direction along the slit is the vertical one. *Upper* panel: major axis spectrum, going from South-West (SW; top) to North-East (NE; bottom). Gas emission lines ([OIII]$\lambda\lambda$4959, 5007, MgIλ5175, Ca,Feλ5269) are the bright ones, stellar absorption lines are the dark ones. Gas (stellar) lines are shifted towards higher (lower) wavelengths at SW, i.e. they are redshifted (blueshifted). The opposite happens at NE. This redshift (blueshift) of lines is due to the Doppler effect, for which receding (approaching) sources emit/absorb lines at redder (bluer) wavelengths with respect to the rest wavelength values of the lines. The galactic nucleus has a non-zero velocity along the line-of-sight. This means that the redshift/blueshift of lines has to be calculated from the wavelength values of lines in the nucleus. In this case, gas lines are approaching NE and are receding SW, while for stars it is the contrary. *Bottom figure*: minor axis spectrum, oriented at perpendicular PA with respect to the major axis. The lines are not shifted towards bluer/redder values. This is expected since velocity vectors of gas and stars have zero projection along the minor axis of the galactic disk.

that there are two stellar disks with opposite angular momenta. Moreover, they perform a photometric decomposition of the total surface brightness radial profile of the galaxy. They succeed in decomposing the profile into the contribution of a bulge and a nonexponential disk. The latter is in turn decomposed into a first exponential disk of scale length $r_1 = 40$ arcsec and a second exponential disk of scale length $r_2 = 10$ arcsec. The first, bigger disk is associated to the prograde stellar

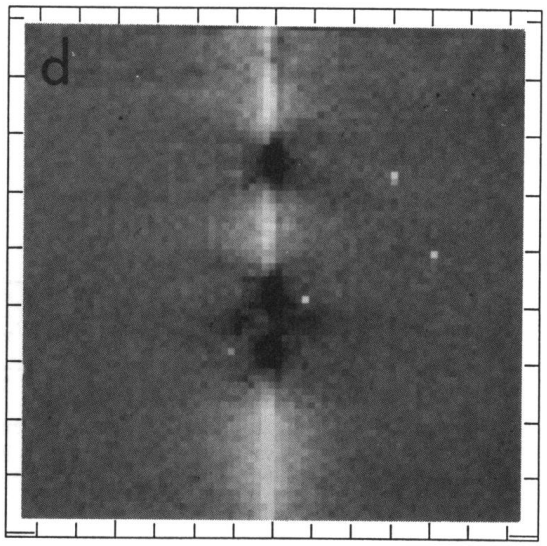

Figure 1.2: Major axis spectrum of NGC 4550 (Rubin et al. 1992). The horizontal direction is the direction of the slit (N to S). The vertical direction is the direction of the dispersion. The bright vertical line is the spectrum of the galactic nucleus. The dark features are stellar absorption lines. They match into the characteristic X-shape in correspondence to the galactic nucleus, due to the fact that one stellar component is receding on one side along the slit direction, the other is receding on the opposite side.

component while the second, smaller disk is associated to the counter-rotating stellar component.

- **counter-rotation in the outer regions of the galaxy:** this happens when a structure such as an external ring or the outer part of a disk counter-rotates with respect to the main disk component of the galaxy. For instance, NGC 4826, a Sab(s) galaxy (Sandage & Tammann 1981), hosts two counter-rotating gaseous disks, an internal one and a more extended and external one. This was shown by Braun et al. (1992) by means of observations of the emission by neutral hydrogen (HI) in the galactic disk. This result finds confirmation in the spectroscopic observations of ionized gas along the major axis of NGC 4826 (Rubin 1994a): at positions on the slit corresponding to the outer regions of the disk (at radii $r \gtrsim 1$ kpc), gas inverts its kinematics (Figure 1.4). In addition, Rix et al. (1995) find that the majority ($> 95\%$) of the whole stellar disk is streaming in same sense of rotation as the inner gaseous disk. Thus, it is the external gaseous disk that counter-rotates with respect to the stellar disk.

- **counter-rotation overall the galaxy:** this case happens when a radially extended structure counter-rotates with respect to the main disk component. NGC 3626 is an example of galaxy with extended counter-rotation (Figure 1.5). Ciri et al. (1995), performing spectroscopic observations along different PAs of NGC 3626,

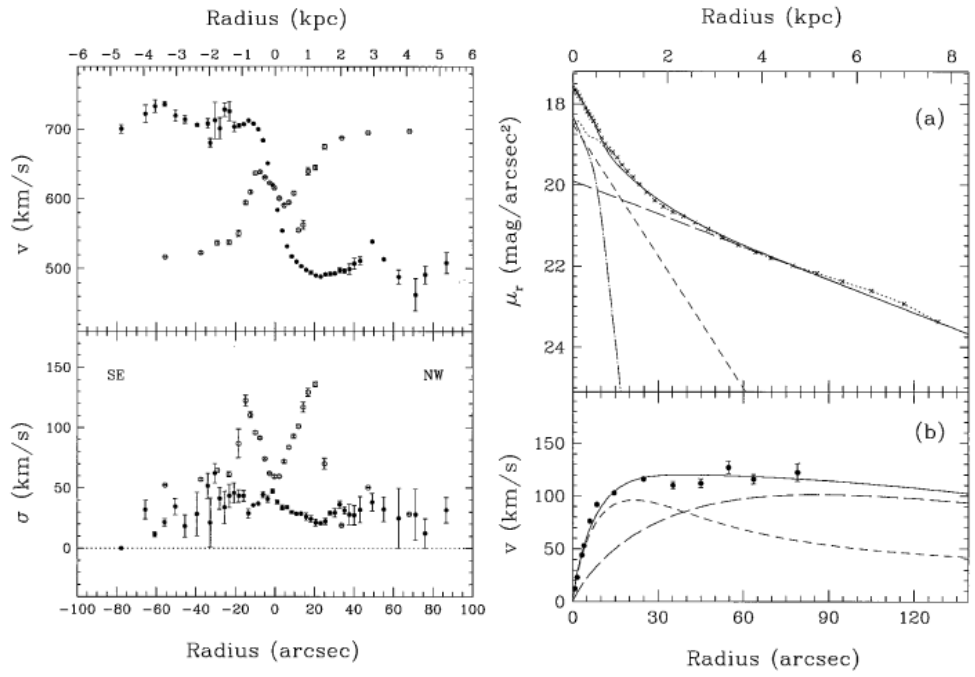

Figure 1.3: Example of counter-rotation in the internal regions in NGC 3593 (Bertola et al. 1996). *Left*: Line-of-Sight velocities V (*upper* panel) and velocity dispersions σ (*lower* panel) of stars (open circles) and gas (filled circles), both in km s^{-1}. For each side from the nucleus and within the inner 20 arcsec, instead of simply increasing its absolute value from the bulge to the outer regions, the velocity curve of stars is reversed. Correspondingly, the stellar velocity dispersions are increased in this region. *Right*: in the *upper* panel, photometric decomposition of the measured radial surface brightness profile (black dots) in the contributions of a bulge (dot-dashed curve), a smaller exponential disk (short-dashed curve) and of a larger exponential disk (long-dashed curve). The total contribution of the two disks is the continuous curve. The total fitted curve is the dotted curve. In the *lower* panel, observed gas velocities within the inner 90 arcsec from the galactic nucleus and the fitting curve (continuous curve) due to the combined contribution of the inner disk (short-dashed curve) and of the outer disk (long-dashed curve).

investigate the kinematics of its gas and stars. They find that the gaseous component is approaching in correspondence to the NW side along the major axis of the projected disk, while stars are approaching on the SE side. Moreover, counter-rotation is radially extended in this galaxy. These results find confirmation in the spectroscopic observations and the measurements by Haynes et al. (2000) and by Silćhenko et al. (2010). Again, in NGC 4546 Galletta (1987) finds that the counter-rotating gaseous disk is extended overall the galaxy. Finally, it must be noticed that even in NGC 4550 the two counter-rotating stellar disks have the same scale length (Rubin et al. 1992).

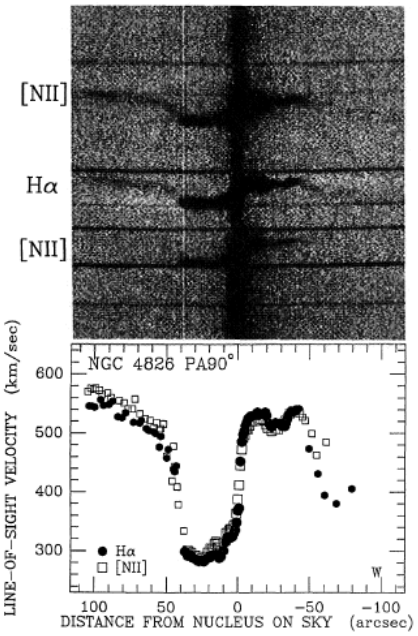

Figure 1.4: Example of external gas-versus-gas counter-rotation. Part of a figure from Rubin (1994a). *Upper* panel: optical spectrum along the major axis (PA = 90^o) of NGC 4826. The vertical direction is the direction of dispersion (Å, increasing upward), the horizontal direction is the distance from nucleus in the sky (in arcsec; rightward: from E to W). H$\alpha\lambda$6563 and [NII]λ6583 emission lines are visible. *Lower* panel: kinematic measurements of Hα (filled dots) and [NII] (empty squares) along the major axis. The vertical direction is the line-of-sight velocity (in km s^{-1}) direction. An inversion of gas velocity is observed at radius $r > 40$ arcsec.

1.2 Morphology of counter-rotation and interaction with the environment

How do galaxies with counter-rotation look like? Is their morphology disturbed? And their environments different from the ones surrounding galaxies with no counter-rotation?

1.2.1 Morphology

Galaxies with counter-rotation appear to have mostly an undisturbed morphology. Possible morphological disturbances may have apparent magnitudes between $B = 25$ and $B = 27$ (i.e. they are very faint) and can be detected with deep optical imaging only (Corsini 2014). One interesting fact is the absence of counter-rotation in late-type spiral galaxies. In fact, most of the spiral galaxies with counter-rotation are mainly S0/a galaxies or Sa galaxies, such as NGC 3593, NGC 3626 and NGC 4138.

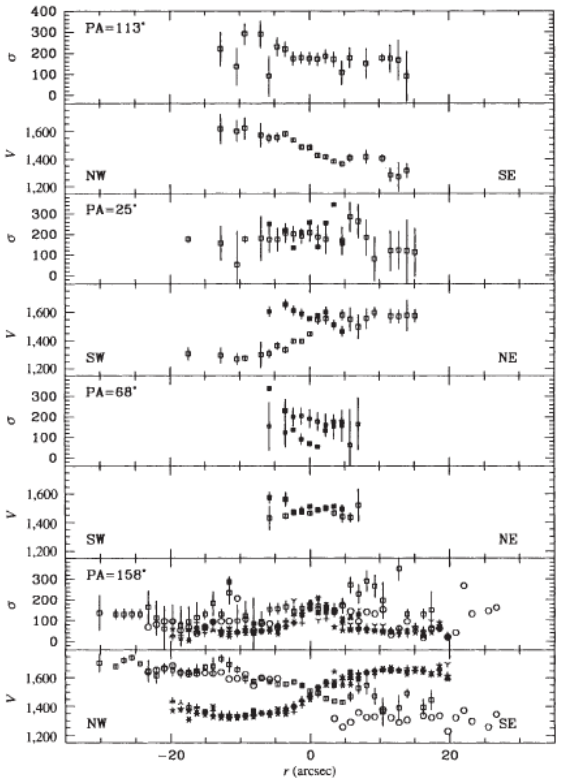

Figure 1.5: Example of extended gas-versus-stars counter-rotation in NGC 3626 (Ciri et al. 1995). From *top* to *bottom*: measurements of the line-of-sight velocity dispersion σ and velocity V (both in km s^{-1}) along PAs 113^o, 25^o, 68^o (minor axis) and 158^o (major axis). The horizontal direction is the projected distance (in arcsec) from the nucleus (rightward from NW to SE in the case of major axis). The velocity dispersion along the major axis shows the typical behavior consisting of an increase of turbulent motions (higher σ) corresponding to the positions in the bulge, while it decreases going outward since both stellar motions and gas motions generally are circular or quasi-circular motions. Stars are not a collisional component, so they have a higher velocity dispersion (higher σ) than gas (collisional component, obliged to stay on circular orbits).

1.2.2 Interaction with the environment

Bettoni et al. (2001) perform a statistical investigation on a sample of 49 galaxies hosting counter-rotation, along with a control sample of 43 galaxies with regular kinematics. They take into consideration different parameters, in particular the number of possible companions (up to a limit apparent magnitude $B_{lim} = 22$), their size and their concentration. They also search for possible bright companions within a maximum distance $R_{max} = 0.6$ Mpc and within differences of redshift velocities $\Delta V_{red} = 600$ km s^{-1}. They conclude that there is no significant difference between environments surrounding galaxies with counter-rotation and environments surrounding galaxies without counter-rotation. Only in case of galaxies that host gas counter-rotation solely, there is a weak tendency

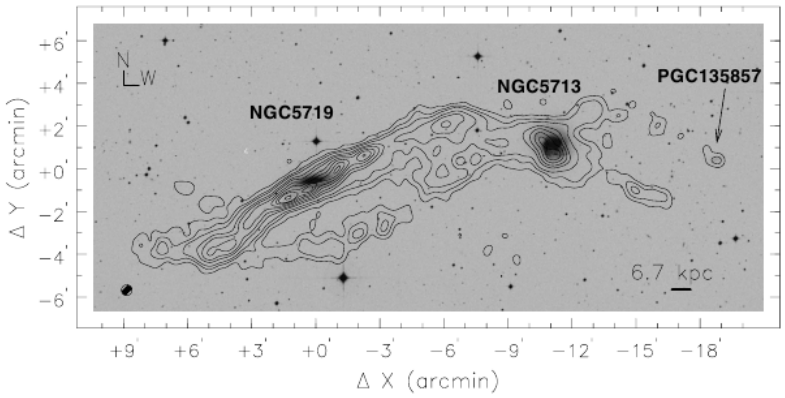

Figure 1.6: Part of a Figure from Vergani et al. (2007). Countour maps of the HI column density distribution of NGC 5719 and of NGC 5713 superimposed on a SDSS image of the two galaxies. The lowest contour level is at 7.0×10^{19} atoms cm^{-2}. The increment in density is 2.4×10^{20} atoms cm^{-2}. Positions along the x-axis and along the y-axis are in arcmin.

for them to be in regions with a low value of density of galaxies. Tidal interactions with other galaxies may be revealed through radio observations of the emission of neutral Hydrogen (HI) at 21 cm. This is the case of NGC 5719, an almost edge-on Sab galaxy which hosts a stellar counter-rotating disk and that is interacting with the nearby face-on Sbc galaxy NGC 5713 (Vergani et al. 2007; Figure 1.6).

1.3 Kinematics of counter-rotation

We can recognize some observational features in the kinematics of galaxies hosting counter-rotation. I will focus on *rotation curves*, on *velocity dispersions* and on the *Line-of-Sight Velocity Distribution* (LOSVD).

1.3.1 Rotation curve and velocity dispersion

Let us consider a disk galaxy and let us assume that we are observing it by means of spectroscopic observations along the major axis of its projected disk. We define rotation curve the velocity curve that we obtain by fitting the measured velocities of stars and gas in the galaxy.

What is the typical rotation curve of stars and gas? For a certain amount of gaseous mass or stellar mass orbiting on the disk, the *circular velocity* $V(r)$ describing its circular motion at distance r from the galactic nucleus is:

$$V(r) = \sqrt{\frac{GM(r)}{r}}, \tag{1.1}$$

with $M(r)$ the mass included within radius r. For a disk galaxy made of a stellar bulge, a less massive disk of stars and gas and a dark matter halo, the rotation curve of gas

and stars will increase from the nucleus to the outer limits of the bulge with a linear dependence on r, $V \propto r$, thus $M(r) \propto r^3$ from Equation (1.1). Then, circular velocity tends to a constant value towards the outer parts of the disk, since the dark matter mass gives dynamic support to the circular motions of stars and gas. Thus, in these regions $M(r) \propto r$. (Figure 1.7). In case that two stellar or two gaseous components counter-

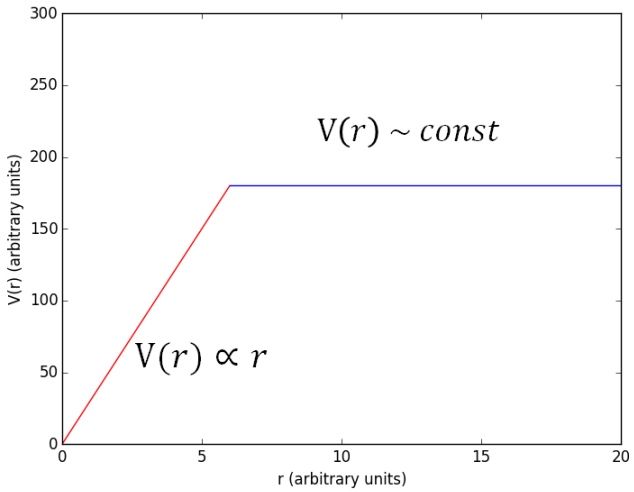

Figure 1.7: Plot showing the schematic behaviour of the rotation curve of gas and stars in the disk of a galaxy. The circular velocity V is plotted as a function of distance r from nucleus. V is assumed to be like in Equation (1.1). The red curve is the linear trend, where $V \propto r$, thus $M(r) \propto r^3$. The blue curve is the constant trend, where V is approximately constant on r. Thus, $M(r) \propto r$ in this portion of the curve.

rotate, the total velocity will decrease or will be inverted where the two counter-rotating components co-exist (Figure 1.8). In a disk galaxy, most gas is distributed on circular orbits. In fact, since it behaves as a collisional component, gas is forced to have circular motions in order to minimize the viscous frictions that could act on it otherwise. On the contrary, stars are a collisionless component, so they can have deviations from circular motions. Thus, it is expected that gas has greater rotation velocities than stars[1].

As to the velocity dispersion, stars have a higher projected velocity dispersion than gas, again because stars are a collisionless component. In the central regions of a galaxy, velocity dispersions of both gas and stars are accentuated, since motions are more turbulent in presence of the bulge. In case of counter-rotation between two stellar components or between two gaseous components, the resulting total projected velocity dispersion is greater where the two counter-rotating components co-exist (Figure 1.8).

[1] A clear example of this is given by the *asymmetric drift*. This mechanism is described in terms of a relation between the square value of the tangential component of the motions of stars (i.e. the one that determines their rotation) and the local value of radial dispersion of their motions. The greater is the radial dispersion, the lower is the tangential motion of stars (see e.g. Binney & Tremaine 2008).

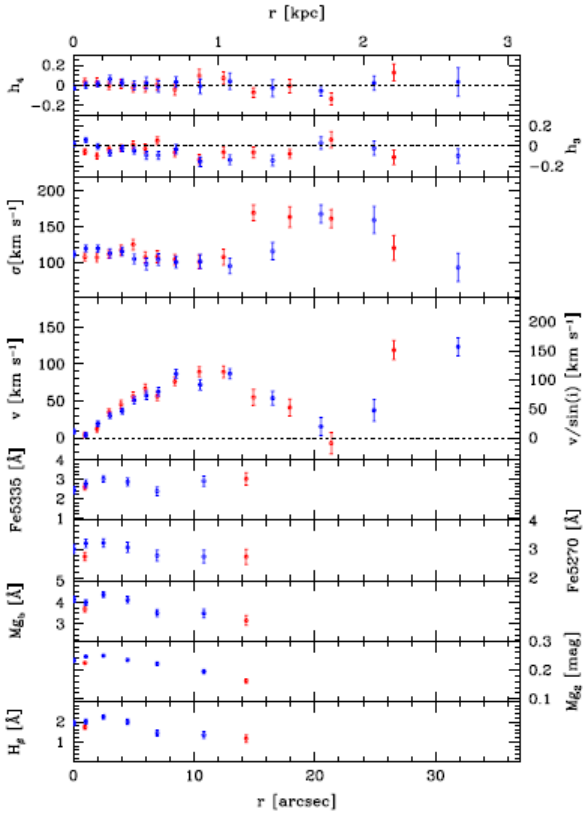

Figure 1.8: From *top* to *bottom*: radial profiles of Hermite polynomial coefficients h_4 and h_3, Line-of-Sight velocity dispersion σ, Line-of-Sight velocity v and unprojected velocity $v/sin(i)$ of stars (σ, v and $v/sin(i)$ are expressed in km s^{-1}) and of equivalent widths (in Å) of stellar absorption lines Fe$\lambda\lambda$5335, 5270, Mg$b\lambda$5178, Mg$_2\lambda$ and H$\beta\lambda$4861 for the galaxy NGC 4138 (Pizzella et al. 2014). The values of velocity and velocity dispersion are lower and higher, respectively, at radius $r \sim 21$ arcsec. This is the signature of a counter-rotating stellar component, which gives its major contribution at this distance from nucleus.

1.3.2 LOSVD

The LOSVD expresses the number of stars as a function of their projected velocities along the Line-of-Sight. Why are we interested in the LOSVD when studying counter-rotation?

The typical LOSVD for a single stellar component is Gaussian at first order. Whenever present, deviations from gaussianity are described with higher order Hermite polynomial terms of correction (Gerhard 1993 and Figure 1.8). If two stellar components counter-rotate, it is expected that, in correspondence to the position along the slit in which the two components co-exist, the LOSVD is no more Gaussian. In contrast, it shows a bimodal fashion, with two peak values of stellar velocities (Figure 1.9, Rix et al. 1992).

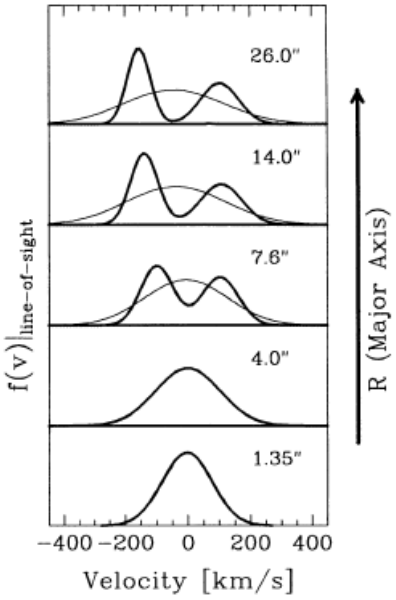

Figure 1.9: Gaussian fits (thin curves) and non-gaussian fits (thick curves) of the LOSVD along different positions on the major axis (direction indicated by the black arrow on the right side) of the projected disk of NGC 4550 (Rix et al. 1992). The horizontal direction is the velocity axis. The two fits are indistinguishable at inner radii (distance from nucleus $r <\sim 5$ arcsec) but are clearly different at higher distances from nucleus. This is due to the strongly decoupled motions of the two counter-rotating stellar components at these radii in NGC 4550.

1.4 Statistics of counter-rotation

It is useful to show the statistics of counter-rotation in S0 galaxies and the statistics of counter-rotation in S galaxies separately.

1.4.1 Statistics in S0 galaxies

Pizzella et al. (2004), taking into account a series of previous studies on the kinematics of 53 S0 galaxies, conclude that a percentage of galaxies corresponding to $32^{+19}_{-11}\%$ of the sample host counter-rotation. This statistics is consistent with a percentage of 35% found by Bertola et al. (1992), with a percentage of $(24 \pm 8)\%$ found by Kuijken et al. (1996) and with a percentage of $24^{+8}_{-6}\%$ found by Kannappan & Fabricant (2001). Moreover, Davis et al. (2011), by means of integral-field spectroscopy and radio observations of a sample of 111 fast-rotating early-type galaxies, find that gas is kinematically decoupled with respect to the stars in 40/111 galaxies ($\sim 36\%$) of the sample. They also obtain that molecular, ionized and atomic gas are always kinematically aligned, even when they are misaligned from the stars.

In contrast to the abundance of counter-rotation of gas in S0 galaxies, Kuijken et al. (1996) estimate that less than 10% of S0 galaxies host counter-rotation of stars with

respect to the main stellar component.

1.4.2 Statistics in spiral galaxies

Pizzella et al. (2004) perform spectroscopic observations along the major axis of 17 spiral galaxies, in order to study their kinematics. Including the results of previous studies on the kinematics of other spiral galaxies, they obtain a sample of 50 S0/a-Scd galaxies. They find that less than 12% of the galaxies in the sample host a counter-rotating gaseous disk, while less than 8% of the galaxies host a counter-rotating stellar disk. Kannappan & Fabricant (2001) analyze 38 Sa-Sbc galaxies. They estimate an upper limit of 8% on the fraction of spiral galaxies hosting a counter-rotating gaseous disk.

1.5 Origin of counter-rotation: the role of minor mergers

In this Section I present the models of formation of counter-rotation. Then, I discuss the possibility that minor mergers can lead to the formation of counter-rotating structures in galaxies and can impact on Star Formation.

1.5.1 Origin of counter-rotation

Models of formation of counter-rotation predict both an *external* and an *internal* origin of the process. In the first case, The mechanisms of *gas accretion*, *major merger* and *minor merger* fall within the first class, while processes connected to a bar (its *structure* and its *dissolution*) fall in the second one.

1.5.1.1 External origin of counter-rotation

These mechanisms predict that fresh gas comes from the environment. The acquired gas accretes onto the disk galaxy to form a counter-rotating structure.

- **gas accretion from the Inter-galactic Medium:** according to this mechanism, a certain amount of gas in the environment surrounding a galaxy falls and accretes onto the galaxy itself. Thus, a gaseous disk is formed in the host galaxy. If gas originally had an angular momentum opposite to the angular momentum of the galaxy, the gaseous disk will counter-rotate with respect to the main component of the galaxy.

  Thakar & Ryden (1996) studied the mechanism taking into account both episodic gas infall and continuous infall on the main galaxy. They showed that this mechanism is capable of building a stable counter-roating gaseous disk.

  In this model, the counter-rotating stellar component is formed only after gas is accreted onto the galaxy from the environment, so the predicted age of the stellar populations in the counter-rotating disk is lower than the age of the pre-existing stellar populations.

- **major merger:** this mechanism consists in the fusion of two galaxies with comparable masses. More precisely, being M_1 and M_2 the masses of the two galaxies, the mass ratio between them is greater than $M_2/M_1 \sim 1/3$. If the galaxies have opposite angular momenta, we have a retrograde major merger. If there are surviving structures after the merger, then counter-rotation may be observed in these structures.

  The model has been investigated by Puerari & Pfenniger (2001) by means of numerical simulations. They conclude that only under a narrow range of initial conditions major mergers are a viable mechanism to produce two counter-rotating disks. This idea is reinforced by Querejeta et al. (2015): performing N-body simulations, they prove that major mergers can destroy disks at first, but leftover debris can fuel their regrowth.

  This model predicts that stars in the counter-rotating component are younger or older than stars belonging to the prograde component, depending on the age of the two galaxies at the moment of the fusion. Simply, the older galaxy has the older stellar population. So, it is expected that in 50% cases the retrograde stellar component is older than the prograde stellar component.

- **minor merger:** this process consists in the fusion of a galaxy (the *main* galaxy) with a dwarf galaxy. The mass-ratio between the mass of the dwarf M_d and the mass of the main galaxy M_m is at maximum of order $M_d/M_m \sim 1/3$. If the dwarf galaxy has an orbital angular momentum that is anti-parallel to the rotational angular momentum of the main galaxy, the minor merger is *retrograde*. In this case, counter-rotating structures may form in the main galaxy.

  This model has been investigated in a variety of cases (e.g. Thakar & Ryden 1996, 1998; Mapelli et al. 2015, hereafter MRM15). I will discuss it in more detail later in this Section.

  This model predicts age differences between the retrograde and prograde stellar components in a similar way to the ones predicted by major merger.

Let us consider now the statistics showed in Section 1.4. The external acquisition of gas is the main explanation for the statistics presented in the previous Section. In fact S0 galaxies are not so rich in gas. This means that, whatever its mass is, acquired retrograde gas can build stable structures that are not disrupted by previously existing prograde gas. In particular, because of the dissipation of energy and thanks to the conservation of the angular momentum, acquired gas tends to accrete on a disk. Being z the direction orthogonal to the equatorial plane of the galaxy, in half cases (50%) the z-component of the angular momentum of gas is parallel to the rotational angular momentum of the S0 galaxy, while in the other half cases (50%) the z-component of the angular momentum of gas is anti-parallel to the rotational angular momentum of the S0 galaxy. This percentage of 50% is compatible with the percentage of 32^{+19}_{-11}% of cases with counter-rotation, within error bars. As gas counter-rotates in the disk, it forms stars and a counter-rotating stellar component originates from it. Since it is

more difficult to recognize and separate the kinematics of a retrograde stellar component from the kinematics of a prograde stellar component (Pizzella et al. 2004; Coccato et al. 2011), in much less cases a retrograde stellar component is detected. This is why the percentage of galaxies with stars-versus-stars counter-rotation is less than 10%.

In the case of S galaxies, pre-existing prograde gas is much more abundant within them. The acquired retrograde gas must be more massive than preexisting gas in order to create a stable counter-rotating disk (Lovelace & Chou 1996). This explains the low percentage of cases in which a S galaxy hosts counter-rotating gas (less than $\sim 12\%$). However, if the mass of the acquired retrograde gas is sufficient to dominate the pre-existing gas, then the counter-rotating stellar component generated from the retrograde gas is sufficiently abundant to be detected. As a consequence, the percentage of cases in which star-versus-star counter-rotation is found in a S galaxy (less than 8%) is not much lower than the percentage of cases with counter-rotating gas in S galaxies.

1.5.1.2 Internal origin of counter-rotation

In addition to the scenarios predicting an external origin of counter-rotation, there are also two theoretical mechanisms that involve processes internal to galaxies.

- **structure of a bar:** in a bar there are retrograde quasi-circular stellar orbits, called x4 orbits (Binney & Tremaine 2008). The stars on these orbits counter-rotate with respect to the other stars in the bar.

  The model was proposed by Wozniak & Pfenniger (1997) in order to explain the *waving pattern* observed in the rotation curves of SB0 galaxies by Bettoni (1989; Figure 1.10) and by Bettoni & Galletta (1997) as due to kinematic properties of the bar.

- **dissolution of a bar:** this mechanism predicts the dissolution of a bar in a galaxy as the origin of the presence of two counter-rotating stellar disks in the galaxy (Evans & Collett 1994). When the triaxial potential of the galaxy slowly dissolves and is redistributed into axi-symmetric shape, the orbits in the central bar are scattered and, since prograde and retrograde orbits are in principle equally distributed within the bar, stars form two identical counter-rotating disks.

  The model was proposed to explain the presence of two counter-rotating disks in NGC 4550. In particular, Evans & Collett (1994) find that the disks are identical in their structure and in their populations. However, Coccato et al. (2013) find that the retrograde component has a lower scale height and that the stellar population in the retrograde component is younger, less metal rich and more α-enhanced than the the stellar population in the prograde component. The difference in age of the two stellar populations is confirmed by the spectroscopy observations of the galaxy by Johnston et al. (2015).

  This model predicts equal ages of the two stellar populations, since the two disks are formed in an equal way.

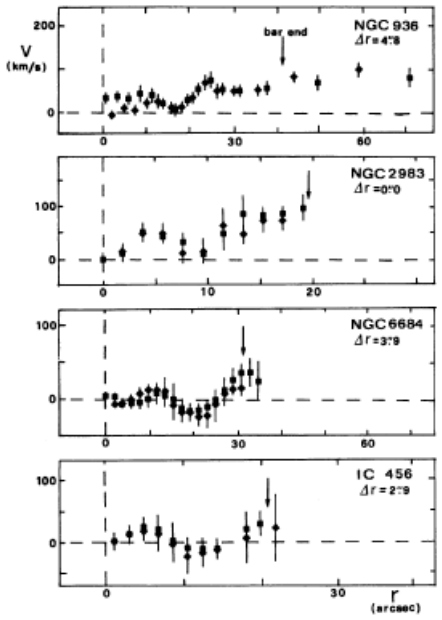

Figure 1.10: Extract from a Figure of Bettoni (1989). It shows measurements of stellar velocities in the bars of four out of the seven analyzed disk galaxies. From *top* to *bottom*: measurements on NGC 936, NGC 2983, NGC 6684 and IC 456. On x-axis the distance r (arcsec) from the symmetry point of each curve. On the y-axis the measured values of velocity V (in km s^{-1}). Each value of Δr indicates how much the symmetry point is distant from the nucleus of the corresponding galaxy. The so-called wavy pattern is clearly visible in each curve. In fact, all the velocity curves first increase going outward, then decrease at intermediate distances from the centre and in the end increase again in the outer regions. This can be explained as due to the presence of counter-streaming stars in the intermediate regions of the bars.

1.5.1.3 Remarks on the models of formation

Considering the statistics in Section 1.4 and given the previous models of formation of counter-rotation, it seems that S0 galaxies and, more in general, early-type disk galaxies are better candidates than S galaxies to acquire gas that can form stable counter-rotating structures (Pizzella et al. 2004). The lack of pre-existing gas in S0 galaxies seems to favor the building of counter-rotating gaseous disks without developing dissipative shocks or viscosity processes that would act against the formation of these structures. Thus, it is possible to understand why in late spiral galaxies there is no episode of counter-rotation discovered up to date. Simply, the over-abundance of gas in Sb/Sc galaxies and in later-type disk galaxies strongly contrasts the possible formation of counter-rotating gaseous disks after gas is acquired from the environment or through a merger. This is due to viscous forces between prograde and retrograde gas that would dissipate the counter-streaming gaseous disk immediately.

It is worth noting that, whenever a galaxy undergoes a retrograde major/minor

merger with another galaxy or acquires retrograde gas from the environment, in all cases these processes must be non-violent (Corsini 2014). In fact, as discussed in Section 1.2, there are no strong morphological disturbances in galaxies that host counter-rotation.

1.5.2 Minor merger: observations and evidences in support of the mechanism

Are minor mergers a valid explanation for counter-rotation in disk galaxies?

The fact that interactions between galaxies could be a mechanism capable of modifying their dynamical evolution and their structural properties had been already suggested by Alladin (1965). As to retrograde minor mergers, Braun et al. (1994) try to find an explanation for the counter-rotating mechanism in NGC 4826. Their conclusion is that the counter-rotating gas in NGC 4826 is of external origin. Expanding this result, Rubin (1994a) states that not only is the origin of the counter-rotating gas an external one, but also this gas can be the remnant of a merger between NGC 4826 and a dwarf galaxy.

Another example is represented by the Sa galaxy NGC 4138. Jore et al. (1996) measure the kinematics of the ionized gas in the galactic disk of NGC 4138 (ionized Hydrogen Hα and ionized Nitrogen [NII]). They find that gas counter-rotates with respect to the main stellar disk and co-rotates with an extended secondary stellar component. They conclude that gas accretion through a minor merger of NGC 4138 with a dwarf could be a possible explanation to the presence of counter-rotating gas. More recently, Pizzella et al. (2014) perform long-slit spectroscopy observations of NGC 4138 along its major axis. Having disentangled the kinematics of the two stellar components, they find that the secondary stellar component is younger, less metal-rich and more α-enhanced than the primary stellar component. This leads them to rule out the possibility of an internal origin of counter-rotation, in favor of an external one. They also confirm the possibility of a past minor merger between NGC 4138 and a dwarf galaxy as suggested by Jore et al. (1996).

In a review, Sancisi et al. (2008), after examining the results of HI observations on a sample of disk galaxies, argue in favour of the importance of minor mergers in the process of building counter-rotating structures such as retrograde bulges.

1.5.3 Minor mergers: N-body simulations and viability of the mechanism

As we can see, there are some observational evidences in support of retrograde minor mergers as a mechanism capable of building counter-streaming structures in galaxies. What do numerical simulations suggest about this scenario?

One of the past challenges was to understand whether or not a retrograde minor-merger could build counter-rotation in a disk galaxy without heating its disk. A first important attempt to model the process is done by Thakar & Ryden (1996) on spiral galaxies, by means of N-body simulations. They adopt a cold thin disk to model the disk component of the main galaxy. They conclude that it is not possible to form a massive counter-rotating disk through the minor merger between a spiral galaxy and a

gas-rich dwarf galaxy. In fact, only a very small dwarf galaxy can transfer gas onto the main galaxy without thickening the pre-existing gas disk. As a consequence, in order to obtain a massive counter-rotating gaseous disk it would be necessary that the main galaxy underwent many minor mergers within a Hubble time, this being a very unlikely scenario according to them.

However, Thakar et al. (1997) simulate the process again. They use a more compact and more massive primary disk to model the main galaxy. They find that not only minor merger is a successful mechanism in producing a counter-rotating gas disk in NGC 4138, but also the disk used to model NGC 4138 is much more resistant to heating than the cold thin disk used in Thakar & Ryden (1996). Furthermore, Thakar & Ryden (1998) run an N-body SPH simulation of minor merger between a spiral galaxy and a gas-rich dwarf galaxy. They obtain a thinner and smaller counter-rotating disk than the ones obtained in Thakar & Ryden (1996) and in Thakar et al. (1997). While it is possible for a disk galaxy to acquire gas through a minor merger, Lovelace & Chou (1996) point out that, more in general, in a galactic disk a certain amount of acquired retrograde gas drags the same mass of the pre-existing prograde gas inward because of friction and viscosity. Thus, it is necessary that the mass of the retrograde gas exceeds the mass of the prograde gas in order to obtain a stable counter-rotating gas disk.

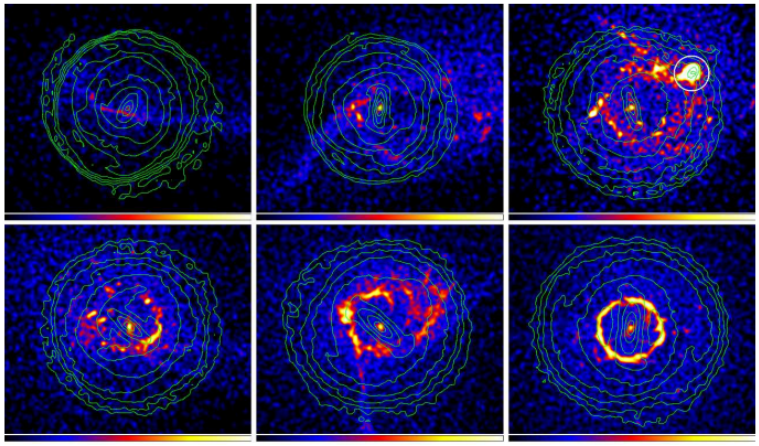

Figure 1.11: Projected density of gas (color-coded map) and of stars (green isocontours) of a S0 galaxy undergoing a retrograde minor merger with a dwarf gas-rich galaxy (Mapelli et al. 2015). From *top left* to *bottom right*: projected densities at 1, 2, 2.35, 3, 5 and 7 Gyr after the first periapsis passage. *Top right*: the white circle marks the nucleus of the dwarf galaxy remnant. Each panel measures 79×67 kpc^2. The authors succeeded in forming a counter-rotating gas ring.

Not only disks, but also other structures such as rings can form as a consequence of a minor merger (Figure 1.11). Balcells & González (1998) run N-body simulations of different minor mergers changing the mass ratio of the galaxies. They choose different initial conditions, in which the spins of the galaxies and their orbital angular momenta are not aligned. They find that with a mass ratio 1/3 it is possible to build a retrograde

bulge in the main galaxy through a minor merger. They also conclude that a variation of the orientations of the galaxies and of their angular momenta does not lead to significant changes in the evolution of the simulated systems, even if counter-rotating structures tend to form early in case of coplanar orbits[2] (Thakar et al. 1997). MRM15 perform N-body SPH simulations of a minor merger between an S0 galaxy and a gas-rich dwarf galaxy. They focus on the formation of rings both for prograde and retrograde cases. In Figure (1.11) I report some density maps for the retrograde case. In the case of the retrograde co-planar minor merger, the gas ring is more stable and more long-lived than the one in the prograde case. They also stress on the importance of the bar in the S0 galaxy as the cause of the earlier dissolution of the ring in the prograde case.

However, it must be noticed that the S0 galaxy used to perform these simulations is an ideal one, since it is completely gas-depleted. On the contrary, real S0 galaxies have a gas reservoir, though modest. Moreover, the number of minor mergers estimated through cosmological simulations is uncertain. Also, there could be a discrepancy between the number of minor mergers predicted by cosmological simulations and the observed one, since the same cosmological simulations are in disagreement with the observations of the number of major mergers experienced by disk galaxies (Bertone & Conselice 2009; MRM15).

1.5.4 Minor mergers: triggering Star Formation

Star Formation (SF) is the physical process by which a certain number of stars is generated from the collapse of a sufficiently dense gas cloud. Depending on the total amount of initial gas mass and on the way the collapse develops through time, it is possible to define an *Initial Mass Function* (IMF), representing the distribution in mass of the new born stars.

The Jeans criterion is generally used to decide whether SF is triggered or not in a gas cloud. Given a gas cloud of density ρ, with temperature T and with a mean molecular weight μ, the Jeans length can be expressed as:

$$\lambda_J = \sqrt{\frac{15 k_B T}{4\pi G \mu \rho}}, \tag{1.2}$$

where $G = 6.67 \times 10^{-8}$ dyne cm^2 g^{-2} is the gravitational constant and where $k_B = 1.38 \times 10^{-16}$ erg K^{-1} is the Boltzmann constant. This length is a critical length. In fact, if a perturbation with wavelength $\lambda > \lambda_J$ acts on the cloud, then the cloud is Jeans unstable, i.e. the cloud cannot keep the balance between its kinematic content and its gravitational content, so that it collapses and SF can be triggered. There are many ways in which a gas cloud can increase its density and in which its gravitational potential can overcome the kinetic energy. For instance, the cloud can be compressed by nearby

[2]The reason why coplanar retrograde orbits generate counter-rotating structures earlier is that in case of non-coplanar orbits the acquired gas spends an initial amount of time in dissipating the components of motion orthogonal to the disk of the main galaxy by means of viscous processes.

supernovae shock-waves, or by a collision with another gas cloud. For a definition of SF in numerical simulations, I refer the reader to the next Chapter.

Is minor merger a mechanism capable of re-activating SF in disk galaxies? Kaviraj et al. (2009) run simulations of minor mergers with different mass ratios between the main galaxies and the dwarf satellites, in order to study their impact on SF. They obtain that minor mergers are a mechanism statistically compatible with a large majority of the observed UV fluxes of star forming regions in S0 galaxies in the local Universe[3]. However, Salim et al. (2012) argue that the statistics in Kaviraj et al. (2009) relative to the number galaxies in which SF is powered by minor mergers is improbable. Instead, they analyze the UV and optical morphologies of a sample of 26 GALEX/SDSS Early Type galaxies (ETGs) galaxies at $z \sim 0.1$ to investigate the incidence of different mechanisms on SF. Comparing the optical extension and the UV-to-optical flux ratio of the galaxies in the sample with two respective control samples of ETGs, they conclude that the fraction of ETGs in which recent SF may have been triggered by minor mergers is only 20% of the sample. However, they state that the real fraction may be higher than the one found. They claim that almost the totality of actively star forming galaxies in the sample are S0 galaxies (Figure 1.12). Furthermore, its seems that minor mergers are compatible with an increase in SF for different structures in S0 galaxies, such as narrow rings, irregular rings and large disks.

The fraction of galaxies obtained in Salim et al. (2012) is compatible with a fraction equal to $0.1 \div 0.3$ found by Bertone & Conselice (2009).

MRM15 find that minor mergers with gas-rich dwarfs induce SF on gas-depleted S0 galaxies, even if they obtain lower levels of SF, namely $10^{-2} \div 10^{-3}\, M_{\odot}\ \mathrm{yr}^{-1}$, against the value of $0.5\, M_{\odot}\ \mathrm{yr}^{-1}$ found by Salim et al. (2012). Comparing their result with the results of observations of emissions at Medium Infrared by Polycyclic Aromatic Hydrocarbons in the nuclei of S0 galaxies and with the deep morphology observations of S0 galaxies (Duc et al. 2015), they conclude that minor mergers play in any case a non negligible role in re-activating SF in S0 galaxies.

While these results are in favor of a scenario in which early-type disk galaxies can in part rejuvenate their stellar content through minor mergers, the same cannot be said of spiral galaxies. Sancisi et al. (2008) find that if a S galaxy undergoes a minor mergers with a dwarf satellite, the mass of the gas introduced in the galaxy accounts for $\sim 1/10$ of the stellar mass rejuvenating through SF in the galaxy. More recently, Di Teodoro & Fraternali (2014) obtain that this fraction corresponds to $\sim 1/5$. As pointed out by MRM15, the reason for a greater impact of minor mergers on rejuvenation of S0 galaxies rather than S galaxies is because S galaxies have a larger gas reservoir by themselves. This reservoir triggers SF in many ways, so that minor merger is just one among many mechanisms that can power SF in S galaxies. In contrast, S0 galaxies have less gas and minor mergers can better impact on rejuvenation mechanisms of stellar populations.

[3]UV fluxes are associated with the activation of Star Formation.

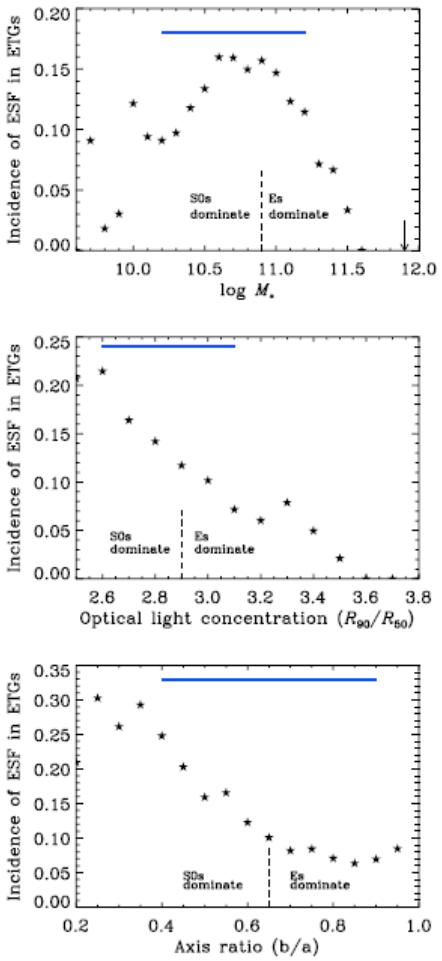

Figure 1.12: Incidence of extended SF in early-type galaxies versus the logarithmic galactic mass (*upper* panel), versus the optical light concentration (*middle* panel) and versus the apparent disk axis ratio (*lower* panel). Galactic masses are expressed in $M_{\odot}$. The optical light concentration is expressed as R_{90}/R_{50}, where R_{50} and R_{90} are the Petrosian radii containing the 50% and the 90% of the total galactic luminosity, respectively. It is evident that the majority of SF events happen in S0 galaxies. Figure from Salim et al. (2012).

1.6 Thesis: aim and contents

The aim of this thesis is to study the possibility to accrete counter-rotating gas on a disk galaxy through a minor merger with a dwarf galaxy. This is done by means of numerical simulations, using an N-body SPH code, ChaNGa. Also, another goal is to quantify the impact of different minor mergers on the process of SF in disk galaxies.

The thesis is structured as follows: in Chapter 2 I first present the general properties of numerical methods, introducing the SPH method and the tree-codes. Then, I introduce the N-body code ChaNGa and I describe some of its general properties. In Chapter 3 I

first present the galactic models and the initial orbital conditions generated for a test run in which I compare ChaNGa with another code, Gasoline. Then, I discuss the results obtained from this comparative test and I show the galactic models and the initial orbital conditions for a set of four simulations. These are the simulations run in order to study counter-rotation and SF. In Chapter 4 I show the results of the simulations. First, I focus on the rotation curves of gas in the main galaxy in three of four simulations. Second, I describe the properties of counter-rotating gas and I show the retrograde gas accretion history in two of these simulations. Third, I perform a study on SF in all simulations. Last, I show the results of a test on gas temperature and density distribution in one simulation. In Chapter 5 I first show the conclusions of the previous analysis and I compare the results obtained in this thesis with literature. Last, I discuss some possible developments of this research work.

Chapter 2

Introduction to indirect N-Body SPH simulations and to ChaNGa

An *N-body simulation* is the integration of the forces acting on a system of N particles over a finite amount of time and by means of numerical methods. N-body simulations are useful to reproduce the evolution of systems that cannot be solved analytically.

In astrophysical systems such as galaxies, the main force acting on each particle and due to all the others is the force of gravity. Given two particles i and j, the gravitational force $\vec{F}_{i,j}$ acting on particle i and due to particle j is given by the Newton equation:

$$\vec{F}_{ij} = -Gm_i m_j \frac{\vec{r_i} - \vec{r_j}}{|\vec{r_i} - \vec{r_j}|^3}\,, \tag{2.1}$$

where G is the gravitational constant, $\vec{r_i}$ and $\vec{r_j}$ are the radius vectors of the two particles and m_i and m_j are their masses.

Given a system of N particles, the total force acting on the i-th particle and due to all the other j-th particles $(i, j = 1, ..., N)$ is:

$$\vec{F_i} = \sum_{j \neq i} \vec{F}_{ij} = -\sum_{j \neq i} G\, m_j\, m_i\, \frac{\vec{r_i} - \vec{r_j}}{|\vec{r_i} - \vec{r_j}|^3}\,. \tag{2.2}$$

In this case, the typical N-body problem is represented by the system of $2 \times N$ equations:

$$\begin{cases} \dot{\vec{r_i}} = \vec{v_i} \\ \dot{\vec{v_i}} = \ddot{\vec{r_i}} = -\sum_{j \neq i} G\, m_j\, \frac{\vec{r_i} - \vec{r_j}}{|\vec{r_i} - \vec{r_j}|^3}\,, \end{cases} \tag{2.3}$$

with $\vec{v_i}$ being the velocity vector of the i-th particle and with the last group of N equations being the equations of motion due to gravitational force. Only for $N = 2$ and for the *restricted case* with $N = 3$ it is possible to find an analytical solution to this problem. For all the other cases, a numerical simulation must be used to integrate the system.

2.1 General properties of numerical methods

Numerical methods can be classified according to their *order*, their *scheme*, their *complexity* and the way gravity is treated (*direct* or *indirect* methods).

2.1.1 Order of numerical methods

It is possible to understand the meaning of "order" of a numerical method by using the *Taylor series expansion* of particle positions and velocities. Given a time t and a time-step Δt, the position $\vec{r}(t+\Delta t)$ and the velocity $\vec{v}(t+\Delta t)$ of each particle are calculated as Taylor series expansions of $\vec{r}$ and $\vec{v}$ around time t:

$$\vec{r}(t+\Delta t) = \vec{r}(t) + \sum_{\alpha=1}^{N} \frac{1}{\alpha!} \frac{d^\alpha \vec{r}(t)}{dt^\alpha} (\Delta t)^\alpha + O[(\Delta t)^{N+1}], \tag{2.4}$$

$$\vec{v}(t+\Delta t) = \vec{v}(t) + \sum_{\alpha=1}^{N} \frac{1}{\alpha!} \frac{d^\alpha \vec{v}(t)}{dt^\alpha} (\Delta t)^\alpha + O[(\Delta t)^{N+1}], \tag{2.5}$$

where $\vec{r}$(t) and $\vec{v}$(t) are the radius vector and the velocity vector of each particle at time t, respectively. N is the order of the method and $N+1$ is the order of the error associated to the method. For example, using a second-order method we have:

$$\vec{r}(t+\Delta t) = \vec{r}(t) + \frac{d\vec{r}(t)}{dt} \Delta t + \frac{1}{2} \frac{d^2\vec{r}(t)}{dt^2} (\Delta t)^2 + O[(\Delta t)^3], \tag{2.6}$$

$$\vec{v}(t+\Delta t) = \vec{v}(t) + \frac{d\vec{v}(t)}{dt} \Delta t + \frac{1}{2} \frac{d^2\vec{v}(t)}{dt^2} (\Delta t)^2 + O[(\Delta t)^3]. \tag{2.7}$$

2.1.2 Schemes of numerical methods

Numerical methods can be *implicit* or *explicit*.

2.1.2.1 Explicit scheme

A numerical method uses an explicit scheme if, starting from time t, it depends only on physical quantities defined at time t in order to calculate all the physical quantities at time $t + \Delta t$.

Example: explicit Euler method This is a first-order method. $\vec{r}(t+\Delta t)$ and $\vec{v}(t+\Delta t)$ are written starting from $\vec{r}$ and $\vec{v}$ calculated at time t and using their derivatives calculated at time t:

$$\vec{r}(t+\Delta t) = \vec{r}(t) + \frac{d\vec{r}(t)}{dt} \Delta t + O[(\Delta t)^2], \tag{2.8}$$

$$\vec{v}(t+\Delta t) = \vec{v}(t) + \frac{d\vec{v}(t)}{dt} \Delta t + O[(\Delta t)^2]. \tag{2.9}$$

Example: leapfrog method In this method, an intermediate time-step $(\Delta t)/2$ is required in order to calculate the physical quantities at time $t + \Delta t$.

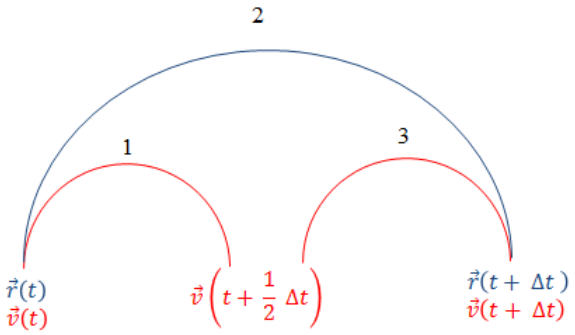

Figure 2.1: Scheme of leapfrog method using KDK and going from time t to time $t + \Delta t$ with intermediate time-step $\Delta t/2$ and with initial position $\vec{r}(t)$ and velocity $\vec{v}(t)$ and final position $\vec{r}(t + \Delta t)$ and velocity $\vec{v}(t + \Delta t)$. The two kicks are represented by red lines, the drift by a blue line. Black numbers 1, 2 and 3 represent the orders in which the corresponding transformations are executed, i.e. we have kick, drift and kick in order of execution. Positions are written in blue and are associated to the drift only. Velocities are in red and are associated to the two kicks.

The method can be developed following a sequence known as **Kick-Drift-Kick**[1] (Quinn et al. 1997), abbreviated "KDK". Here is a simplified scheme of KDK (Figure 2.1):

1) kick: the velocity is kicked to an intermediate value, i.e. $\vec{v}(t + \frac{1}{2}\Delta t)$ is calculated starting from $\vec{v}(t)$:

$$\vec{v}(t + \frac{1}{2}\Delta t) = \vec{v}(t) + \frac{1}{2}\Delta t\, \vec{a}(t)\,; \tag{2.10}$$

2) drift: the position is drifted. This means that $\vec{r}(t + \Delta t)$ is calculated starting from $\vec{r}(t)$:

$$\vec{r}(t + \Delta t) = \vec{r}(t) + \vec{v}(t + \frac{1}{2}\Delta t)\, \Delta t\,; \tag{2.11}$$

3) kick: the velocity is kicked to its final value $\vec{v}(t + \Delta t)$ starting from $\vec{v}(t + \frac{1}{2}\Delta t)$:

$$\vec{v}(t + \Delta t) = \vec{v}(t + \frac{1}{2}\Delta t) + \frac{1}{2}\Delta t\, \vec{a}(t + \Delta t)\,. \tag{2.12}$$

We finally obtain:

$$\vec{r}(t + \Delta t) = \vec{r}(t) + \vec{v}(t)\, \Delta t + \frac{1}{2}(\Delta t)^2 \vec{a}(t)\,; \tag{2.13}$$

[1] There is also a similar Drift-Kick-Drift leapfrog method. This is not discussed in this thesis.

$$\vec{v}(t+\Delta t) = \vec{v}(t) + \frac{1}{2}\Delta t\,\vec{a}(t) + \frac{1}{2}\Delta t\,\vec{a}(t+\Delta t)\,. \tag{2.14}$$

In order to integrate a Keplerian binary system it is better to employ the leapfrog method rather than the explicit Euler method. In fact, the former has a second-order dependence on Δt in the calculation of $\vec{r}$, so the error associated to this method is less than the one associated to explicit Euler method. Moreover, the leapfrog method grants a better energy conservation in the system.

2.1.2.2 Implicit scheme

A numerical method uses an implicit scheme if it depends on quantities defined at time $t + \Delta t$ in order to calculate them, starting from time t.

Example: backward Euler method This method uses an implicit scheme. In fact, $\vec{r}(t+\Delta t)$ and $\vec{v}(t+\Delta t)$ are written starting from $\vec{r}$ and $\vec{v}$ calculated at time t but using their derivatives calculated at time $t + \Delta t$:

$$\vec{r}(t+\Delta t) = \vec{r}(t) + \frac{d\vec{r}(t+\Delta t)}{dt}\,\Delta t + O[(\Delta t)^2]\,, \tag{2.15}$$

$$\vec{v}(t+\Delta t) = \vec{v}(t) + \frac{d\vec{v}(t+\Delta t)}{dt}\,\Delta t + O[(\Delta t)^2]\,. \tag{2.16}$$

2.1.3 Complexity of numerical methods

Given a system of N particles, the complexity of a numerical method is the number of operations required in order to integrate the system for a given time-step.

The complexity of a numerical method can be expressed as a function of N. In this case, the bigger N is, the greater is the number of operations required to integrate the system. It is important to choose a method with a low complexity to reduce computational times.

2.1.4 Treatment of gravity: indirect methods versus direct methods

Depending on the way gravity is treated, a *direct* N-body method or an *indirect* N-body method needs to be implemented. In this Section I discuss both direct methods and indirect methods, while in the following Sections of this Chapter I discuss indirect methods only.

Direct methods A direct method is a numerical method in which the force of gravity is calculated for all couples of particles in the system. For a system of N particles, the complexity of a direct method scales approximately as N^2. In fact, for each i-th particle ($i = 1, 2, ..., N$) it is necessary to calculate all $N - 1$ interactions with the other particles, hence $N(N-1)$ interactions must be calculated each time. This is approximatively N^2 interactions if $N >> 1$.

Direct methods are useful in case of *collisional systems*. In fact, in collisional systems the stellar density is very high and the strength of gravitational interactions between particles is not negligible. This means that the direct calculation of the gravitational interaction between particles is necessary in order to solve the system correctly.

Galactic nuclei and *star clusters* are examples of systems that need to be integrated with direct codes. In galactic nuclei there can be many strong gravitational interactions between stars and many 3-body encounters (interactions between a keplerian binary and a single star). In these systems the gravitational interaction rate scales as $\rho/v^3 > 1$, being ρ the mean density of the system and v the mean velocity module of the particles. For instance, assuming to have a globular cluster with central stellar mass density $\rho_{star} \sim 10^3 M_\odot$ pc^{-3} and with velocity dispersions $\sigma_{star} \sim 4$ km s^{-1}, the gravitational interaction rate scales as $10^3/64 \sim 16 > 1$ (in units of $M_\odot$ s^3 pc^{-3} km^{-3}).

In the case of close interactions, direct codes must have at least a 4^{th}-order accuracy. In fact, shorter time-steps are necessary to better describe the gravitational interaction between particles, taking into consideration its rapid variation. An example of direct method is the $4^{\text{th}} - order\ Hermite\text{-}Scheme$.

Indirect methods An indirect method is a method which does not calculate the gravitational interaction between all the couples of particles in a system. Instead, this method uses a *multipole expansion* of gravitational force in the case of distant particles. Thus, less calculations are done with the consequence that these methods have a lower complexity.

A paradigm for algorithms used in indirect methods is given by the *Barnes-Hut* tree-code, which is discussed in Section 2.5.

Indirect N-body methods are useful in case of collisionless systems. In these systems, stellar density is very low and there are no 3-body encounters or strong gravitational encounters. A collisionless system can be treated as a fluid and the gravitational interaction rate scales as $\rho/v^3 < 1$. This means that times between two consecutive gravitational encounters (also called *relaxation times*) are extremely long if compared with the typical dynamical time-scale of the system. Galaxies are an example of collisionless systems. In fact, both strong and weak gravitational interactions of stars, along with their possible geometrical impacts, are completely negligible within galaxies. For instance, in the solar neighborhood, assuming a stellar mass density $\rho_{star} \sim 0.4 M_\odot$ pc^{-3} and a velocity dispersion $\sigma_{star} \sim 30$ km s^{-1}, the gravitational rate goes as $\sim 0.4/30^3 \sim 1.5 \times 10^{-5} << 1$ (in units of $M\odot$ s^3 pc^{-3} km^{-3}).

2.1.5 Time-steps

The choice of the correct *time-step* is important to correctly run a simulation. In fact, shorter time steps will imply more calculations by the computer on which the simulation is run, while longer time-steps will not permit to reproduce processes requiring higher time resolution to be correctly described, such as 3-body encounters.

There are many techniques to implement time-steps in numerical methods. An example of these techniques is the *block* time-step algorithm.

Example: block time-step The aim behind the introduction of block time-steps is to group particles in discrete time blocks according to their time-steps.

Given a system with an initial time t_0 and given the i-th particle of the system, if its dynamical time-step Δt_i satisfies:

$$\left(\frac{1}{2}\right)^n < \Delta t_i < \left(\frac{1}{2}\right)^{n-1}, \tag{2.17}$$

for a certain $n \in \mathbb{N}$, the particle is inserted in the n-th block, and the corresponding block time-step is $\Delta t_n = (1/2)^n$. The advantage of using sub-multiples of 2 to define time-steps is that computers do calculations using binary representation of numbers. Furthermore, all the particles associated to the same block time-step will evolve at the same rate.

Now, let Δt_m be the minimum block time-step, for a certain m. The first update of position and velocity is done for the particles with block time-step Δt_m only. These are called *active particles*. The other particles are not updated in this step. Having updated the active particles, the new system time can be calculated and it is $t = t_0 + \Delta t_m$. Now, not only particles with block time-step Δt_m, but also particles with block time-step Δt_{m-1} are updated. The new system time is calculated again adding another Δt_m, and it is $t = t_0 + \Delta t_m + \Delta t_m = t_0 + \Delta t_{m-1}$. For all particles with block time-step less or equal than Δt_{m-1}, their dynamical time-step is calculated again. The procedure is then repeated until all the block time-steps with increasing value are covered and the corresponding particles are updated.

In collisional systems, the dynamical evolution of each particle can be very different from the evolution of the others. Moreover, each particle can have strong interactions with other particles. Block time-steps are introduced to solve the problem of the association of a time-step to each particle in collisional systems. In fact, if each particle is associated to a specific time-step that takes into account the specific dynamical evolution of that particle, the risk is to have many updates of particles at very different times, with the consequence that particles evolve in a unsynchronized way. By introducing block time-steps, particles are associated to time-steps that are sub-multiples of 2. Furthermore, the simulation time is always in a integer ratio to each sub time-step. The consequence is that calculations made by processors are eased.

2.2 Softening lenght

In this Section I introduce the concept of *softening length* (also called *softening radius*).

Let us consider a collisionless system and let us consider Equation (2.1) again.
If the distance between the two particles i and j tends to zero,

$$r_{ij} = |\vec{r_i} - \vec{r_j}| \to 0\,, \tag{2.18}$$

then Equation (2.1) diverges to infinite. If the particles of a system are treated as point objects, with no spatial extension, the behaviour described in Equation (2.18) is possible and spurious scatterings between the two particles are permitted.

The softening length ϵ is a radius greater than zero, introduced to modify Equation (2.1) in the following way:

$$\vec{F_{ij}} = -Gm_i m_j \frac{\vec{r_i} - \vec{r_j}}{(|\vec{r_i} - \vec{r_j}|^2 + \epsilon^2)^{\frac{3}{2}}} \,. \tag{2.19}$$

If Condition (2.18) is satisfied, there is still a ϵ^2 greater than zero at the denominator of Equation (2.19), so that the latter does not diverge to infinite. If implemented in collisionless systems, the softening radius prevents spurious scatterings are avoided. For a virialized system of N particles with virial radius R_{vir}, a good estimate of the softening length is:

$$\epsilon = \left(\frac{4\pi}{3} R_{vir}^3\right)^{\frac{1}{3}} N^{-\frac{1}{3}} \,. \tag{2.20}$$

Dehnen (2001) found a more accurate way to determine ϵ for a system that includes a Navarro-Frenk-White (NFW) dark matter halo (Navarro et al. 1996). He obtained the following expression:

$$\epsilon = 0.07 r_s \left(\frac{N}{10^5}\right)^{-0.23} , \tag{2.21}$$

with r_s being the scale radius of the NFW halo of the system.

It is worth noting that the introduction of the softening radius in the Newton equation modifies the physics of the problem for small distances between particles. In case $r_{ij} = |\vec{r_i} - \vec{r_j}| >> \epsilon$, i.e. for very distant particles, Equation (2.19) is not significantly different from Equation (2.1).

2.3 Gas treatment: Smoothed Particle Hydrodynamics

In this Section I discuss the differences between the simulation of stellar and dark matter particles and the simulation of gas particles. All differences arise from the fact that gas is a fluid. In fact, gravity is not the only force acting on gas, but other physical quantities such as pressure terms and viscosity terms give further contribution to determining the evolution of gas.

2.3.1 Fluid equations

Let us consider an element of gas in an infinitesimal volume around a point in space. It is possible to introduce the Euler equations in *local* form (i.e. in the neighbourhood of the point and at given time t):

$$\begin{cases} \frac{\partial \rho}{\partial t} + \nabla \cdot (\rho u) = 0\,; \\ \\ \frac{\partial \rho u}{\partial t} + \nabla \cdot (\rho u \otimes u) + \nabla p = -\rho \nabla \phi\,; \\ \\ \frac{\partial \rho u e}{\partial t} + \nabla \cdot [\rho u (e + p/\rho)] = -\rho u \cdot \nabla \phi\,, \end{cases} \tag{2.22}$$

where ρ is the gas density, u is the velocity of gas, ρu is the momentum density of the gas, ϕ is the gravitational potential of gas, $\nabla\phi$ is the acceleration of gas due to gravitational potential, e is the specific energy of gas (i.e. the energy per gas particle), ρe is the energy density of gas and p is the gas pressure.

If $\nabla\phi = 0$, the three equations are in a *conservative form*, since they express the conservation of three quantities, that are mass, momentum and energy of gas respectively. In systems such as galaxies, gas is affected by gravitational interactions with stars and with dark matter and $\nabla\phi \neq 0$. In this case, Equations (2.22) are not in conservative form.

A precise relation exists between gas pressure, energy density and velocity:

$$p = (\gamma - 1)\rho\left(e - \frac{1}{2}u^2\right), \tag{2.23}$$

being γ the gas adiabatic coefficient.

2.3.2 SPH method

Gas Equations (2.22) can be solved with a *Lagrangian* or a *Eulerian* approach (or even with some hybrid technique).

The Eulerian method consists in dividing space in cells through the use of a grid, and then in calculating all the quantities that represent the physical state of gas in each cell. The Lagrangian method consists in focusing on each particle of gas and in calculating all its quantities following its particular evolution.

The *adaptive mesh refinement* method (abbreviated AMR) and the *Smoothed Particle Hydro-dynamics* method (abbreviated SPH) are two possible numerical implementations of the Eulerian and of the Lagrangian method, respectively.

I discuss only SPH and I refer the reader to Teyssier (2002) for AMR.

2.3.3 Smoothing length

Given a system of N particles, the smoothing length of a particle is defined as the distance h within which the particle has a given number M of neighbours (with $M = 32, 64, ...$). The smoothing length is introduced to average (hence to "smooth") the properties of gas.

It may be asked how the introduction of the smoothing length in simulated gas systems affects the evolution of the systems themselves. To answer this question, we first

consider the case of a continuous distribution of gas, with all the physical quantities A of the system defined as functions of $\vec{r}$, $A = A(\vec{r})$. The **kernel function** $W(\vec{r}^{\,'} - \vec{r}^{\,''}, h)$ can be introduced, where $\vec{r}^{\,'}$ and $\vec{r}^{\,''}$ are the radius vectors of two generic points in the gas volume. The kernel function acts as a mask that averages and smooths the gas properties around a given point, taking into account the gas properties defined within a distance $2\,h$ from that point. In particular, given a point with radius vector $\vec{r}$, the kernel function $W(\vec{r} - \vec{r}^{\,'})$ is zero for each point with radius vector $\vec{r}^{\,'}$ such that $|\vec{r} - \vec{r}^{\,'}| > 2\,h$, otherwise it is different from zero. Then, the smoothed value of A calculated in $\vec{r}$ is:

$$\langle A(\vec{r})\rangle = \int W(\vec{r} - \vec{r}^{\,'}, h) A(\vec{r}^{\,'}) \mathrm{d}^3 r \,. \tag{2.24}$$

Thanks to W, the previous integral is a weighted mean of the physical quantity A within the sphere of radius $2\,h$ around $\vec{r}$.

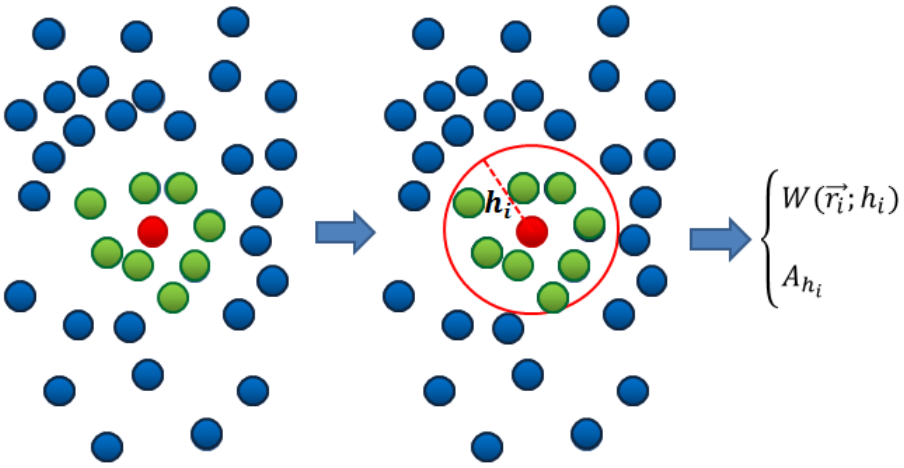

Figure 2.2: Scheme of the implementation of SPH for the discretized case of a sample of particles. The test particle, namely the i-th particle, is the red one. The green particles are the N nearest neighbours. For this example, I choose $N = 8$. *Left*: the 8 nearest neighbours are chosen. *Centre*: the radius h_i is calculated, taking into account that it must include the 8 nearest neighbours. Thus, the circular area associated to it (the area within the red circle) is defined. *Right*: the kernel function W within h_i can be calculated and the generic physical quantity A can be smoothed within h_i.

Moving to a discretized system of N particles, we obtain:

$$\begin{cases} \int \longrightarrow \sum \,, \\ W(\vec{r} - \vec{r}^{\,'}, h) \longrightarrow W(\vec{r_i} - \vec{r_j}, h_i) \,, \\ \langle A(\vec{r})\rangle \longrightarrow A_{h_i} = \sum_{j=1}^{N} m_j W(\vec{r_i} - \vec{r_j}, h_i) A_i \,, \qquad i, j = 1, 2, ..., N \,, \end{cases} \tag{2.25}$$

being $\vec{r_i}$ and $\vec{r_j}$ the radius vectors of the i-th and of the j-th gas particle, respectively, being m_j the mass of the j-th gas particle and being h_i the smoothing length of the i-th particle (Figure 2.2).

It is possible now to write the equations of motion for the i-th gas particle of the system, taking Euler equations into account:

$$\begin{cases} \dfrac{d\vec{r_i}}{dt} = \vec{v_i}\,, \\ \\ \dfrac{d\vec{v_i}}{dt} = -\dfrac{\nabla P_i}{\rho_i} + \vec{a}_{i,visc} - \nabla\phi_i\,. \end{cases} \tag{2.26}$$

where P_i is the pressure exerted on the i-th particle and where $\vec{a}_{i,visc}$ is the viscosity acceleration. Apart from $\vec{a}_{i,visc}$ all the physical quantities in the second group of Equations (2.26) are intended to be smoothed with the kernel function.

It is important to note that the viscosity term in the second group of Equations (2.26) is an artificial term. In fact, if the fluid is represented by a discrete distribution of particles, there is no natural viscosity acceleration, and this term needs to be inserted artificially. This is the case of SPH methods. In case of methods such as AMR, in which gas is treated as a continuous fluid, the viscosity emerges naturally from Equations (2.22).

The introduction of the smoothing length modifies the physics of a system in a similar way to the softening radius. However, differently from this one, the smoothing length needs the presence of a kernel to average and modify the physical properties of the system, while the softening radius can be simply inserted in Equation (2.1). As an alternative, for the case of the softening length one can use the Plummer kernel, which is an analogous version of the kernel function.

Having rewritten the equations of motion for gas, it is possible to integrate a system using the leapfrog method. Of course, having modified the equations of motion implies that the leapfrog method is now implemented considering the averaged properties of the fluid, with the addition of the artificial viscosity term.

2.4 Sub-grid physics

In this Section I introduce *sub-grid* physics in numerical simulations. All the physical processes that happen at scales lower than the resolution scale of the simulation are grouped under the term "sub-grid physics". These mechanisms are treated with some particular simplifications that permit to implement them correctly in numerical codes.

As an example, I discuss SF, *gas cooling* and *Supernova*(SN) mechanisms.

2.4.1 Star Formation

In a numerical simulation SF represents the mechanism by which part of the gas particles are converted to star particles, i.e. there is a process generating star particles at the expense of gas particles.

The general relation between the *Star Formation Rate* (SFR) and gas density was proposed by Schmidt (1959):

$$\Sigma_{SFR} = C\Sigma_{gas}^{n}\,, \tag{2.27}$$

where Σ_{SFR} is the surface mass density of the star-forming gas per unit time, C is a constant which depends from the observations and Σ_{gas} is the surface mass density of gas. Studying SF in 100 nearby galaxies, Kennicutt (1998) proposed a value 1.5 for n in Equation (2.27).

According to the implementation by Katz (1992; see also Stinson et al. 2006), in an N-body simulation the i-th gas particle of the system can be converted to a star particle if it satisfies all of the following conditions:

- the particle must be denser than a minimum threshold value $\rho_{min} \sim 0.1$ cm^{-3} (the precise value depends on the simulation);
- the particle is situated in an overdense region;
- the particle is part of a converging flow;
- the particle is unstable to Jeans criterion:

$$\frac{h_i}{c_i} > \left(\frac{1}{4\pi G\rho_i}\right)^{\frac{1}{2}}, \tag{2.28}$$

  where h_i is the smoothing length of the particle, c_i is the sound speed of the gas particle and ρ_i is the density of the gas particle.

Finally, only a small fraction of all the gas particles eligible for conversion are effectively converted. This fraction of particles are chosen by means of the following stochastic method by Stinson et al. (2006): if the i-th gas particle satisfies the previous four conditions, its probability p_i is estimated as:

$$p_i = \frac{m_i}{m_{star,i}}\left[1 - \exp\left(-c^*\frac{\Delta t}{t_{dyn}}\right)\right], \tag{2.29}$$

where m_i is the mass of the i-th gas particle, $m_{star,i}$ is the mass of the star particle potentially spawned from the i-th gas particle, c^* is an efficiency dimensionless factor, Δt is the time-step of the simulation and t_{dyn} is the dynamical time-scale of the particle. Then, if p_i is greater than a random number $r \in [0, 1]$, the i-th gas particle is converted to a star particle (Figure 2.3). The dependence of SFR on c^* is showed in Figure (2.4).

Some codes, such as ChaNGa, use a more refined technique to generate a star particle. In particular, whenever the gas particle matches all the previous conditions for conversion, only a fraction f of its mass is converted to a star particle. This avoids brutal conversion of a gas particle into a star particle. It is a good rule to keep $f \gtrsim 0.1$, in order to avoid spurious effects on the spawned star particle due to its too low mass.

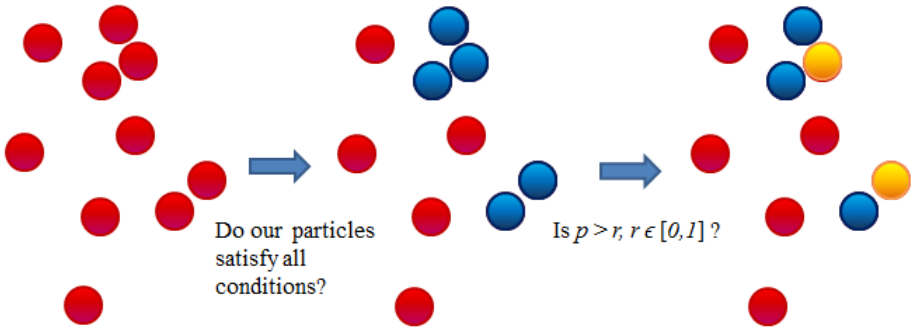

Figure 2.3: Scheme illustrating the conversion of a gas particle into a star particle. *Left*: initially we have a certain number of gas particles (red particles). *Centre*: if some particles satisfy the four conditions by Katz (1992), then they are eligible to be converted into star particles (blue particles). *Right*: among all the potentially convertible particles, only the ones with the corresponding p value higher than a random number r are truly converted into star particles (yellow particles).

What has been previously described can be applied only to large-scale simulations. In small scale simulations (like molecular clouds, star clusters or small galaxy simulations), where the mass of the gas particles is less than $\sim 1 M_{\odot}$ and the box size is less than ~ 1 kpc, other recipes must be used. In this case, the *sink particle* technique may be adopted. I do not discuss this technique here. For details about it, I refer the reader to Bate et al. (1995).

2.4.2 Gas Cooling

Gas cooling is the process by which gas loses energy (for example by emitting it in form of radiation) and lowers its temperature.

In numerical simulations, usually there are three alternatives to describe gas:

1) *adiabatic Equation of State* (EoS): gas does not exchange heat with the environment;

2) *thermal* EoS: gas temperature is constant;

3) *cooling/heating*: gas changes its temperature according to a cooling/heating function.

If the cooling option is active, a new equation containing the cooling function is added to gas equations:

$$\frac{de}{dt} = -\frac{P}{\rho}\nabla \cdot v - \frac{\Lambda(e,\rho)}{\rho}\,, \tag{2.30}$$

where e is the specific thermal energy, P and ρ are the gas pressure and density, v is the gas velocity and Λ is the cooling function.

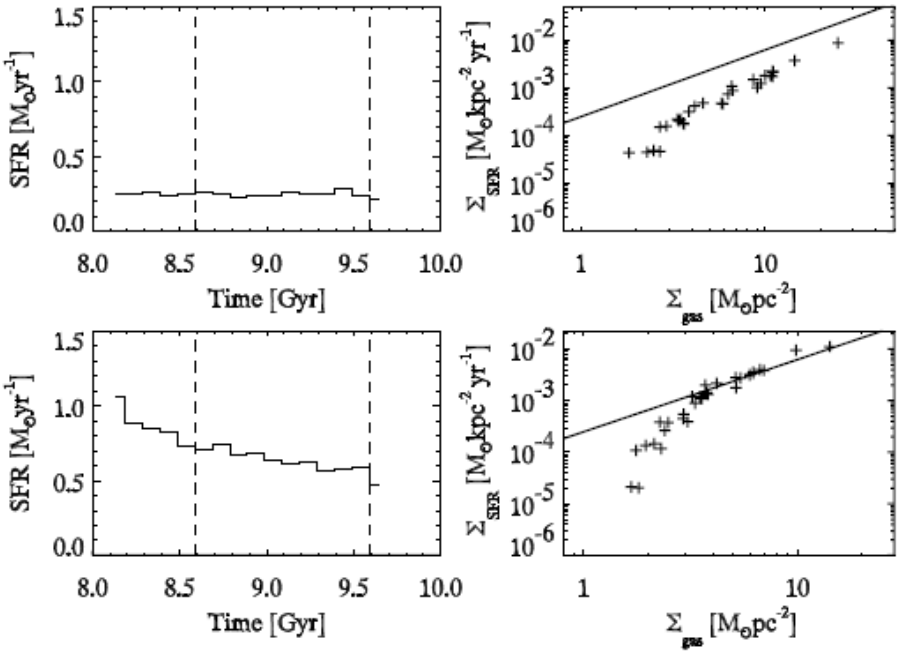

Figure 2.4: *Left-handed* panels: SFR (in $M_{\odot}\mathrm{yr}^{-1}$) as a function of time (in Gyr) for lower (*upper* panel) and higher (*lower* panel) values of the c^* constant appearing in Equation (2.29). *Right-handed* panels: surface SFR (in $M_{\odot}\mathrm{kpc}^{-2}\mathrm{yr}^{-1}$) as a function of gas surface density (in $M_{\odot}\mathrm{pc}^{-2}$) for lower (*upper* panel) and higher (*lower* panel) values of the c^* constant. Image from Stinson et al. (2006)

Sutherland & Dopita (1993) have described the main sources of cooling in low density astrophysical gas. I report their results for Collisional Ionization Equilibrium (CIE) conditions only.

2.4.2.1 Physical mechanisms contributing to cooling function

The main contribution to the cooling function is given by resonance lines. A first exception is given by ionized Iron (FeII) and neutral Hydrogen (HI), that dominate the contribution to the cooling function at temperatures lower than $T \sim 2 \div 3 \times 10^4$ K. An additional exception is represented by free-free processes, that dominate the contribution to the cooling function for temperatures higher than $T \sim 10^7$ K (Figure 2.5).

2.4.2.2 Chemical elements contributing to cooling function

Among the different chemical elements, as previously stated, Hydrogen and Iron (mainly HI and FeII, respectively) give the main contribution to the cooling function at temperatures lower than $\sim 2 \div 3 \times 10^4$ K. At temperatures ranging between 10^4 K and 10^5 K, Carbon (C) and Silicon (Si) give the main contributions to the cooling function. Oxygen

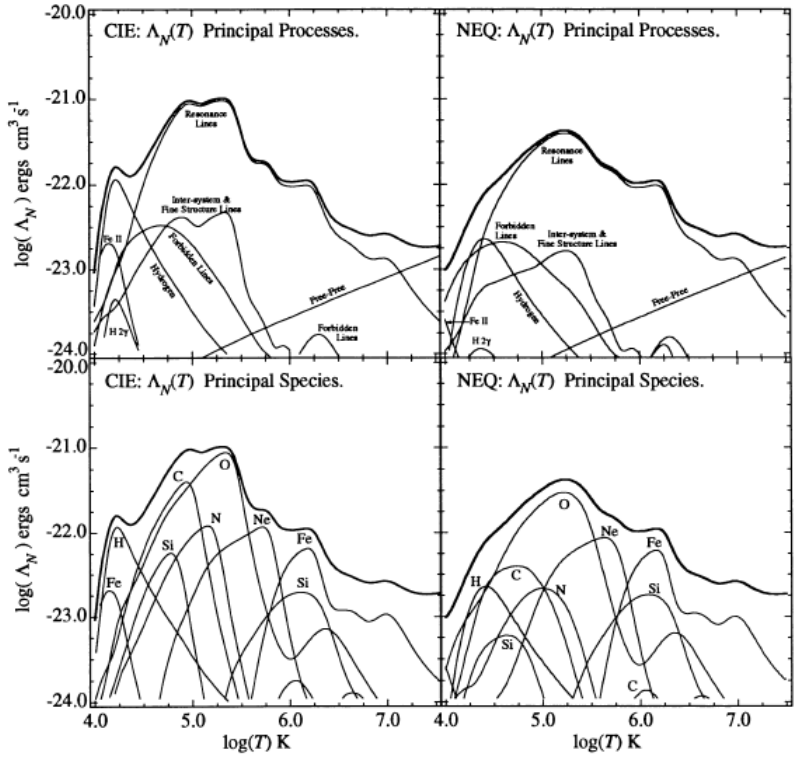

Figure 2.5: Dependence of the cooling function Λ (y-axis in all panels) on temperature (x-axis in all panels). *Top-left* panel and *bottom-left* panel: principal processes and principal species, respectively, that contribute to the cooling function, in chemical equilibrium condition. *Right* panels: the same as in left panels but in *Non EQuilibrium condition* (NEQ). In this case one is interested to the left panels, since non-equilibrium variations of chemical abundances are not considered in this thesis.

(O) dominates at $\sim 2 \div 4 \times 10^5$ K, with a minor contribution given by Nitrogen (N), while Neon (Ne), Si and, most of all, Fe dominate at higher temperatures.

2.4.2.3 Chemical composition of sources contributing to cooling function

The sources of gas cooling can be divided in three groups according to their chemical composition: *metals*, *non-metals*, *dust* and *molecules*.

- **metals:** the major contributions of metals to the cooling function are above a temperature of 10^5 K, with a lower temperature tail at $\sim 10^4$ K. Given a temperature T, the cooling function grows with increasing metallicity [Fe/H][2];

[2]The metallicity of a system is usually defined as the ratio between the abundance of Fe to the abundance of HI. This ratio is represented by the notation [Fe/H] and it is expressed in units of the same ratio calculated in the Sun.

- **non-metals:** the contributions of non-metals to the cooling function peak at $\sim 10^4$ K. They are given by H_2 and HI. For higher temperatures, only atomic hydrogen is the relevant non-metallic source of cooling. Both these contributions have a tail at lower temperatures between a little bit less than $\sim 10^3 \div 10^4$ K;

- **dust and molecules:** dust and molecules are the most relevant source of gas cooling below 10^3 K and in conditions of low metallicity. Typical molecules in astrophysics are CO, OI, O_2 and H_2O and hydrides (chemical compounds made with negative hydrogen ion H^-).

As a consequence of this, it is expected that no significant cooling takes place below 10^3 K in low density astrophysical gas, except for molecules and dust.

2.4.2.4 Time-scales for gas cooling

What are the typical time-scale values τ_{cool} for gas cooling? As shown in Figure (2.6), in CIE conditions time-scales are limited to a maximum value $\tau_{cool,max} \sim 10^7$ yr for temperatures slightly higher than $T \sim 10^8$ K. At temperatures ranging from a bit more than 10^4 K to 10^8 K the cooling is faster, with time-scales reaching a minimum of $\tau_{cool,min} \sim 10^3$ yr at $T \sim 3 \div 5 \times 10^2$ K for solar metallicity.

This implies that in galaxy-scale simulations or in cosmic-scale simulations, τ_{cool} is much less that the time-scale of the whole simulation ($\tau \sim 10^9$ yr).

2.4.3 Supernovae

Among all *Supernovae* (SN) types, only Supernovae II (SNII) are included in most sub-grid physics, since they are the most energetic and they can be a relevant mechanism in simulations.

Typically, the energy ejected by a SN is in the form of kinetic and thermal energy. In the case of galactic-scale simulations and of cosmological simulations kinetic energy is converted to thermal energy in less than 1 time-step, so that in the end the whole energy released by SN is considered as being in the form of thermal energy.

2.4.3.1 Algorithm for Supernovae

I briefly discuss the procedure to implement SN mechanisms in simulations according to Stinson et al. (2006).

First of all, each star particle is associated to a *Single Stellar Population* (SSP) recipe. A SSP is a model of stellar populations which contains different synthetic stars, each of them with its own mass given by the *Initial Mass Function* (IMF) associated to the modeled stellar population. In practice, each star particle is decomposed in stars that are distributed in mass according to a given IMF. Lifetimes of these stars are then calculated. Thus, it is possible to know the number of SN that explode at a given time t, that is $N_{SN}(t)$.

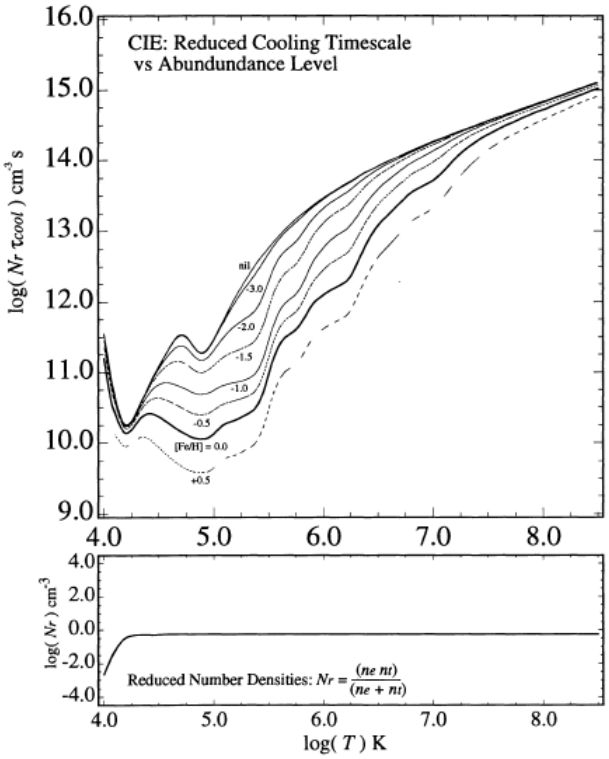

Figure 2.6: *Upper panel*: dependence of cooling timescale τ_{cool} (y-axis, in s) on gas temperature (x-axis, in K). Timescales are weighted with reduced particle density N_r (cm^{-3}) of gas. Different curves are related to different metallicities. Higher metallicities correspond to lower timescales. *Lower panel*: dependence of gas particle density on gas temperature for the same range of temperatures as in the upper panel. The reduced particle density is defined as in the formula expressed in the lower panel, where n_e is the total electron density and n_t is the total number density of ions.

At this point, the energy emitted by all the SN in a given star particle is redistributed between the surrounding gas particles according to a criterion. This criterion can change if we use SPH or mesh techniques. In case of SPH, the increase of energy received by the i-th gas particle is:

$$\Delta E_{SN,i} = \frac{m_i W(|\vec{r_i} - \vec{r}_{SN}|, h_{SN}) \Delta E_{SN}}{\sum_{j=1}^{N} m_j W(|\vec{r_j} - \vec{r}_{SN}, h_{SN}|)}\,, \tag{2.31}$$

where ΔE_{SN} is the energy released by SN in the star particle, m_i and m_j are the masses of the i-th and j-th gas particle respectively (with $i, j = 1, ..., N_{gas}$), $\vec{r_i}$, $\vec{r_j}$ and $\vec{r}_{SN}$ are the radius vectors of the i-th gas particle, of the j-th gas particle and of the star particle containing SN, respectively, h_{SN} is the smoothing length of the star particle and W is the kernel function already defined in Section 2.3.3.

If E_{SN} is the energy released by one SN explosion, the total energy ΔE_{SN} distributed

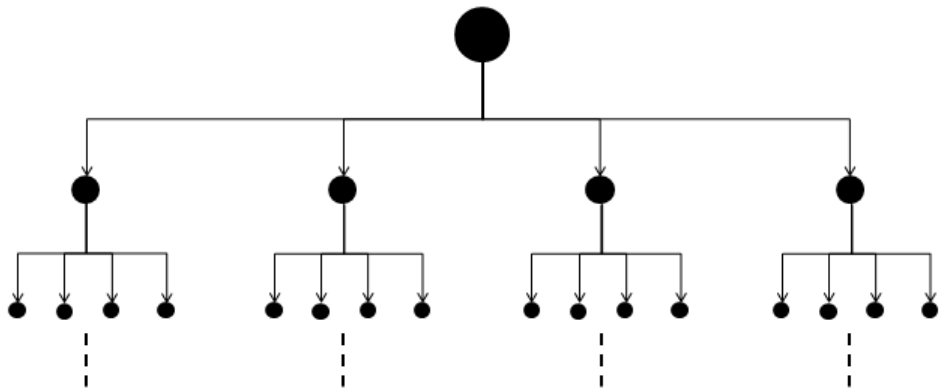

Figure 2.7: Illustration of the idea behind the division in sub-cells (nodes) for the case of a quad-tree. Each node (black dots) is divided in four sub-cells, that in turn become nodes that can be sub-divided in four sub-cells again. The dashed lines mean that the subdivisions can go on until the corresponding leaves of the tree are not reached. The first, bigger dot is the root of the tree.

to the neighbour gas particles by the N_{SN} SN in a star particle can be expressed as:

$$\Delta E_{SN} = E_{SN} N_{SN} = f 10^{51} \mathrm{erg} \tag{2.32}$$

where $f < 1$. Thus, only a fraction f of the total energy emitted by all the SN in a star particle is distributed between the gas particles.

2.5 Tree-codes

A *tree-code* is an N-body code that distributes all the particles of a simulation in sub-cells within the simulation box, in order to avoid the direct calculation of the force of gravity for all couples of particles. Tree-codes are used to simulate collisionless systems since, as already discussed in Section 2.1, in these systems collisions between particles are negligible and direct calculation of gravity is not necessary for distant particles.

The word "tree" means that the simulation box (the **root** of the tree) is divided in sub-cells (the **branches** of the tree, also called *nodes*) that in turn are divided in sub-cells, until the minimum-volume cells (the **leaves** of the tree) are reached. A good rule to go on with the division in sub-cells is to check if a minimum number of particles is still present in a cell. Depending on the number of sub-cells in each cell, the tree has a different name. For example, if each cell is divided in two sub-cells, the tree is called **binary tree**, while if each cell is divided in four sub-cells, the tree is called **quad-tree**. Each sub-cell in the tree is also called **node** of the tree (Figure 2.7).

A common implementation of tree-codes is the *Barnes-Hut* algorithm (Barnes & Hut 1986).

2.5.1 Barnes-Hut tree-code: implementation

Here is the general idea about how the Barnes-Hut tree-code works.

Let the i-th particle in the simulation be our test particle. If another particle, for instance the j-th particle, is sufficiently near to particle i, then the gravitational force acting on particle i and due to particle j is calculated, otherwise the particle j is added to a *interaction* list. All the particles added in this list are substituted with a particle of mass m equal to the sum of the masses of all the particles in the list and with position equal to the position of the mass centre of the particles in the list. Then, only the gravitational force acting on particle i and due to this single particle will be calculated.

In practice, a mathematical criterion is needed to decide when to calculate the gravitational force between two particles or when to put a particle in the interaction list. Let A be the test particle on which the force must be calculated. Let N_1 be the node in which particle A resides. Let N_2 be another node, containing some particles $B, ..., M$. Let s be the width of N_2 and let d be the distance between the centre of mass of node N_2 and particle A. Le θ be a parameter called *opening angle*, so that the following criterion can be introduced.

If s, d and θ satisfy:

$$\frac{s}{d} > \theta\,, \tag{2.33}$$

then all the particles in the node are added to the interaction list and the direct gravitational force on particle A due to them is not calculated. Otherwise, if Condition (2.33) is not satisfied, it means that the mass centre in node N_2 is sufficiently near to particle A if considered with respect to the dimension of node N_2 itself. In this case, it is said that the node N_2 is "opened", i.e. the calculation is repeated for all sub-cells within N_2 that contain particles. When a sub-cell of node N_2 is a leaf of the tree and its mass centre does not satisfy Condition (2.33), then all the single forces acting on A and due to all the corresponding particles in that sub-cell will be calculated.

Typical values of θ are near to 0.5. If $\theta = 0$ it means that no particle can be considered sufficiently distant to group it with others in the interaction list and so only direct force of gravity is calculated. In Figure (2.8) I present a simplified scheme which summarizes the method.

2.5.2 Barnes-Hut tree-code: complexity

The Barnes-Hut tree-code has a reduced complexity with respect to a direct N-body code. In fact, a direct N-body code has to calculate $N-1$ interactions for each of the N particles of the system and its complexity scales as $N(N-1)$, which is roughly N^2 for $N >> 1$. In contrast, the complexity of the Barnes-Hut algorithm scales as $NlogN$, so this code is faster and it requires less computations. This is a consequence of the introduction of the interaction lists that reduce the number of times gravity force has to be calculated for a given particle in the system.

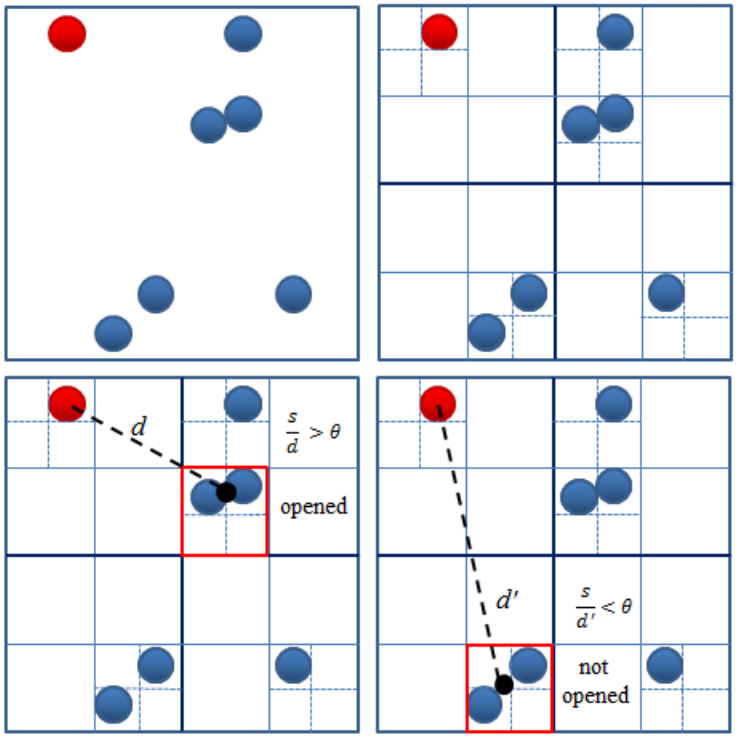

Figure 2.8: Scheme representing the node opening criterion and the tree division. In this example, I adopt a quad-tree and I associate a maximum number of particles per leaf equal to one. *Upper left-handed* panel: sample of particles in the simulation box. The red particle is the test particle on which we calculate gravity. *Upper right-handed* panel: the division of the root of the tree (the box) into quad-cells (the nodes; thick blue lines) and, in turn, the division of each quad-cell in four sub-cells (the leaves in this case; thin blue lines) and of the latter quad-cells into other sub-cells (thin short-dashed lines). *Lower left-handed* panel: the red empty square indicates the selected node. The black dot is the mass centre of the particles in the selected node, d is the distance of the mass centre from the test particle and s is the linear scale length of the selected node. In this case, s/d is greater than the opening angle θ and the node is opened (i.e. we directly calculate gravity due to each particle acting on the test particle). *Lower right-handed* panel: the selected node has a linear scale length again equal to s and the mass centre of its particles has a distance d' from the test particle. In this case, s/d' is less than θ and the node is not opened (i.e. particles are added to the interaction list).

2.5.3 Barnes-Hut tree-code: integration

A leapfrog method is mostly used to integrate the Barnes-Hut tree-code.

Since the Barnes-Hut tree-code is implemented for collisionless systems, 3-body encounters and other strong interactions are avoided and there is not the necessity of using block time-steps. Instead, a common time-step is used for all particles. This is defined as:

$$\Delta t = min\left[\Delta t_{max}, \left(\frac{2\eta\epsilon}{|a|}\right)^{\frac{1}{2}}\right], \tag{2.34}$$

where η is the accuracy parameter, ϵ is the softening radius, Δt_{max} is a user-provided maximum time-step (otherwise it has a default value given by the code) and a is called *Barnes-Hut acceleration* and it can be the mean acceleration of the particles or it can be the maximum acceleration of the particles.

The tree is not maintained the same through the whole simulation. Instead, it is updated after a certain number of steps. By doing this, it is possible to take into account the evolution of the system. For instance, if in a simulation two galaxies are far at start, the tree is structured considering that particles of one galaxy are too distant from particles of the other galaxy and so they interact through multipole expansion of gravitational interaction. As the two galaxies will have started approaching, particles of one galaxy will get near to particles of the other galaxy and the tree must be updated considering that gravity needs to be directly calculated for more couples of particles.

2.6 Other codes

The direct-summation scheme and the Burnes-Hut algorithm are not the only available algorithms for N-body codes. Other algorithms are the *Particle-Mesh* (PM) algorithm, the *Particle-Particle/Particle-Mesh* (PP/PM) algorithm and the *Fast-Multipole-Moment* (FMM) algorithm.

2.6.1 Particle-Mesh

The idea behind a PM code (Hohl 1978; Hockney & Eastwood 1988) is to discretize positions of particles in space before calculating the gravitational potential of a system. From the knowledge of the gravitational potential, it is possible to calculate the force acting on each particle and so it is possible to calculate position and velocity of each particle.

The Poisson Equation for the gravitational potential ϕ of a continuous distribution of mass density ρ is:

$$\nabla^2\phi = 4\pi\rho. \tag{2.35}$$

Now, let all the particles in the system be grouped in a spatial grid, called *mesh*. The centre of each cell in the mesh is called *mesh-point* of the grid. Each mesh-point has a mass density equal to the mass density of its cell. Then, Equation (2.35) can be solved on the discrete distribution of mesh-points obtained, instead of using a continuous distribution of mass. In order to calculate the force acting on a particle, two ways can be followed:

1) calculating the force acting on the nearest mesh-point;

2) calculating the interpolation of the forces on the mesh-points in the particle position.

In Figure (2.9) there is an example grid for PM.

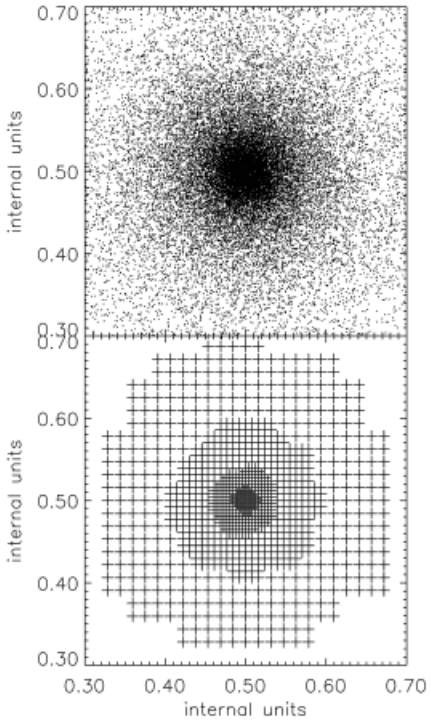

Figure 2.9: *Multi-Level Adaptive Particle Mesh* (MLAPM) from Knebe et al. (2001). *Upper panel*: projected distribution of particles in a simulation (the box measures 0.40 x 0.40 in units internal to the simulation). *Lower panel*: adaptive grid for the MLAPM method. Differently from classical PM, the grid employed here is defined following the morphology of the structures simulated in the code.

This method is faster than tree-codes. In fact, if $G < N$ is the number of cells in the mesh, the problem of calculating the gravitational potential scales as $GlogG$. Given the fact that we have a total number of N particles per simulation, the complexity of the method scales as $NGlogG \sim N$.

2.6.2 Particle-Particle/Particle-Mesh

The PP/PM method is a hybrid method which combines the direct calculation of the force of gravity for nearby particles (PP) with the PM method for long-distance interactions. Let A be again the test particle. Let s be the size of the cell in which A is contained. If some particles $B, ..., M$ are distant less than $2\,s$ or $3\,s$ from A, the direct force of gravity on A due to each of them is calculated. For the interaction of A with the other particles, the PM method is applied in order to interpolate the potential from the distribution of mesh-points in the simulation volume, and then to calculate the force acting on A as described in Subsection 2.6.1.

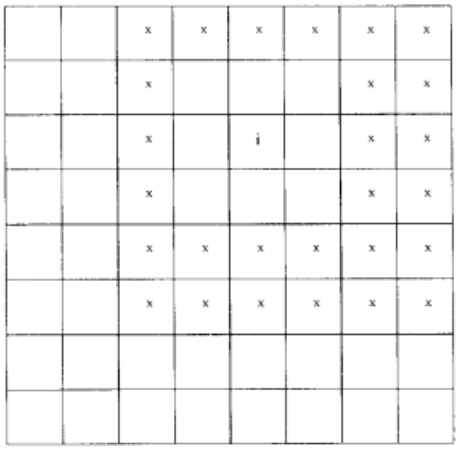

Figure 2.10: FMM method. Illustration of the division of the whole box sub-cells. There are 4^l sub-cells at node level $l = 0, 1, 2, ...$ (given a level of subdivision in cells, each cell is in turn divided in four sub-cells to obtain the following level of subdivision). The test box is marked i and it is at level 3. The empty boxes next to i are the *nearest neighbours* to i. The box at level 2 containing i is the parent box to i. Boxes marked x are children to the nearest neighbours to i's parent. Gravitational potential expansion terms are calculated taking this subdivision of the simulation volume into account. This Figure is taken from Greengard & Rokhlin (1987).

2.6.3 Fast-Multipole-Moment

As the name suggests, FFM is based on the expansion in series of the gravitational potential field (Greengard & Rokhlin 1987). This series is written using angles of spherical coordinates, and it is truncated at a certain order.

FFM is similar to a tree-code, but instead of evaluating forces acting on particles, it evaluates gravitational potential on particles. It is similar to a tree-code because of the division in sub-cells of the simulation volume. It is different from a tree-code for the following reasons:

1) leaves can have more than one particle. This reduces the number of sub-cells for the subdivision of the volume;

2) the multipole expansion of the potential is more accurate than the use of the centre of mass for distant particles. However, the procedure of calculating the multipole expansion of the potential is heavier and requires more work by computers (Figure 2.10);

3) the calculation of forces is done only at leaf level.

2.7 Computer clusters

Computer clusters are groups of computers used to do calculation in parallel in order to integrate a system. A computer cluster is used instead of a single computer when the

number of particles N of a system is very big. A single CPU (*Central Processing Unit*, or processor) of a computer does not have the required performance to integrate these kinds of systems. Instead, using a computer cluster permits to redistribute work load and processes between different CPUs, with the advantage of fastening the entire simulation.

An example of computer cluster (or "supercomputer") is Galileo, at the italian numerical computing centre CINECA. Galileo uses up to 8256 cores, with a maximum number of 16 cores per node, and has a RAM (*Random Access Memory*) of 128 GB per node (i.e. 8 GB per core)[3].

2.7.1 Computer clusters: general properties

Given a N-body simulation and a cluster of p processors, an algorithm can be chosen to distribute the N particles between the processors. For example, the simplest algorithm is the equal distribution of particles between processors, that is having N/p particles per processor. Generally, particles are distributed according to their position in the simulation volume: near particles are associated to the same computer in the cluster, while distant particles are associated to different computers in the cluster. Since gravity is a long-range force, all the computers in a cluster must interact and communicate in order to exchange information about the interaction between distant particles.

Communication between processors must be fast and rapid, otherwise the simulation is slowed-down. While $p << N$, increasing p is convenient, since more processors are available and operations in parallel are made easier. But for $p \sim N$, too much computers are available and they must exchange too much information about gravity, if compared to the number of particles N. Because communication is extremely important, computer clusters must have a very fast internal network with a high transmission velocity between the cluster components (typically higher than 10 Gbit sec^{-1}) and a low latency (that is, the time delay between the stimulation sent to the system and its response).

How do computers exchange their information? *Message Passing Interface* (MPI) is one of the most used libraries to do so. It consists of a series of libraries useful to many of the different programming languages in which codes for simulations may be written. A particular version of MPI is the open-source Open-MPI, which consists of a merger between four MPI libraries: FT-MPI, LA-MPI, LAM-MPI and, partly, PACX-MPI[4]. This protocol was created to be compatible with high performance and efficiency requirements by computers clusters.

2.7.2 Computer clusters: scaling and speed-up

The *scaling* is defined as the way time for running a simulation changes as a function of the number of cores used in the cluster. At the same time, we define *speed-up* the ratio

[3]More information about supercomputer Galileo can be found at `http://www.hpc.cineca.it/hardware/galileo` .

[4]From the University of Tennessee, the Los Alamos National Laboratory, the Indiana University and the University of Stuttgard, repsectively. More information about Open-MPI can be found in the webpage `http://www.open-mpi.org` .

between the sequential execution time of a code and the parallel execution time of the code. Sequential execution means that the code is processed and executed by only one CPU, while parallel execution means that the code is processed and executed using a cluster of CPUs. The ratio of the speed-up to the number of processors determines the *efficiency* or *linearity* of the executed code.

In the ideal case, by increasing the number of processors the time required for the simulation decreases linearly, while the speed-up increases linearly. This is a consequence of parallel computing which is fastened as more processors are used to run the simulation. However, in the real case, both the time required to run a simulation and the speed-up start to deviate from the ideal linear fashion at large numbers of processors. In particular, computation times tend to be higher than the ones predicted by the linear behaviour and speed-up tends to be lower than its value as predicted by the linear behaviour. This change in behaviour of time and speed-up at large numbers of processors is a consequence of the need of CPUs for inter-communication and for exchanging information about gravity force. The greater is the number of processors, the higher the quantity of information is exchanged between them. Moreover, if gas physics, SF and other physical processes are added to the system, the communication between processors is slowed-down.

2.8 ChaNGa

ChaNGa (*CHArm* N-*body* *GrAvity solver*) is a N-body SPH code used to integrate collisionless systems. It was first developed and presented by Jetley et al. (2008; 2010). ChaNGa is a modified version of the N-body SPH code *Gasoline* (Wadsley et al. 2004). The code is executed in parallel thanks to the use of the parallel programming language CHARM ++, a derivation of C++.

2.8.1 From Gasoline to ChaNGa: inherited properties

As already noted in the introduction to this Section, ChaNGa is similar to Gasoline, so it inherits a lot of properties from this code. These properties are discussed in this Subsection.

For differences between the two codes I refer the reader to Subsection 2.8.2 and to Chapter 3.

2.8.1.1 Gasoline: introduction

Gasoline is an N-body cosmological code first developed and presented by Wadsley et al. (2004). It represents a further development from a previous code, PKDgrav (Stadel 2001). In particular, like PKDgrav before it, Gasoline is written as a parallelized code. This means that it is optimized to be executed by many CPUs that work in parallel and between which the workload is redistributed.

The Barnes-Hut tree code, already discussed in Section 2.5, has been implemented in Gasoline in order to calculate gravity. The tree is a binary tree, and the partition of

the cells is similar to the one in the K-D tree by Bentley (1979). Gasoline employs hexadecapole moment expansion in series to calculate the gravitational interaction between distant particles. The *buckets* (i.e. the leaves of the tree) can have up to a maximum number of 8 or 16 particles. Moreover, it is the whole bucket, not the single particles whitin it, that interacts with the environment. This last point has the consequence to fasten calculations of gravitational interactions.

2.8.1.2 Gasoline: Smoothing length and SPH

In Gasoline, SPH is implemented as described in Section 2.3.3, with some clarifications needed.

The number of neighbours that define the smoothing length h_i of the i-th particle is generally 32 or 64 and it is extabilished and fixed before running a simulation.

As for the smooting kernel, given two particles i and j, W_{ij} is calculated as:

$$W_{ij} = \frac{1}{2}w(|\vec{r_i} - \vec{r_j}|/h_i) + \frac{1}{2}w(|\vec{r_i} - \vec{r_j}|/h_j), \tag{2.36}$$

with $w(x)$ being a spline defined as in Monaghan (1992) and with the other quantities defined as in Section 2.3.3.

The viscosity acceleration of the i-th particle in Equation (2.26) is:

$$\vec{a}_{visc,i} = \sum_{j \neq i} \vec{a}_{visc,ij}\,, \tag{2.37}$$

where each term in the series is:

$$\vec{a}_{visc,ij} = \begin{cases} \frac{-\alpha\frac{1}{2}(c_i+c_j)\mu_{ij}+\beta\mu_{ij}^2}{\frac{1}{2}(\rho_i+\rho_j)} & \text{for } \vec{v}_{ij}\cdot\vec{r}_{ij} < 0\,, \\ \\ 0 & \text{otherwise}\,, \end{cases} \tag{2.38}$$

where

$$\mu_{ij} = \frac{h(\vec{v}_{ij}\cdot\vec{r}_{ij})}{\vec{r}_{ij}^{\,2} + 0.01(h_i+h_j)^2} \tag{2.39}$$

and where $\alpha = 1$ and $\beta = 2$ are the shear coefficient and the viscosity coefficient respectively, c_i and c_j are the sound speed terms, $\vec{v}_{ij} = \vec{r_i} - \vec{r_j}$ and $\vec{v}_{ij} = \vec{v_i} - \vec{v_j}$ (Wadsley et al. 2004).

2.8.1.3 Integration

Gasoline employs the leapfrog scheme with the KDK method - already discussed in Section 2.1 - to integrate systems (Wadsley et al. 2004). Multiple time-stepping is available for gas treatment, with the presence of *sub-stepping rungs* that are submultiples of the base time-step by factors of two.

2.8.2 From Gasoline to ChaNGa: differences in the code

In the previous Subsection I have presented the properties of Gasoline inherited by ChaNGa. Many similarities are present between the two codes. Moreover, both of them are mostly written as sequential codes that have to be parallelized with particular routines.

However, there are some differences in the way Gasoline and ChaNGa are parallelized. According to Wadsley et al. (2004), Gasoline code is organized with a four-layer structure:

1) the first layer is the *Master Layer* (ML) and it organizes the general progress of a simulation;

2) the second layer is the *Processor Set Tree Layer* (PSTL) and it distributes work between the different processors;

3) the third layer is the *Machine Dependent Layer* (MDL) and it organizes remote calls between processors, parallel diagnostics and memory organization;

4) the fourth layer is the *Parallel-KD Layer* (PKDL) and it implements physics and local trees management.

The MDL is the part of the code which has the role to parallelize Gasoline. In contrast, in the case of ChaNGa, the routine which parallelizes the code is external to it. As already said, this routine is CHARM++ and it provides for all the operations in parallel such as remote calls between different CPUs, memory sharing and workload distribution between the processors.

2.8.3 ChaNGa: scaling and other properties

Menon et al. (2015) have demonstrated that, running simulations with a 25 Mpc box, in gravity only mode, ChaNGa works well with more than 128000 cores with 2 billion particles and with multi-stepping enabled. Furthermore, they show that the code scales well up to 512000 cores for two datasets of 12 and 24 billion particles (Figure 2.11).

In addition to this, according to Menon et al. (2015), ChaNGa adopts a cubic spline for the calculation of softening length. Furthermore, as to the SPH implementation in the code, ChaNGa adopts a Barnes-Hut algorithm to identify the nearest neighbours to each gas particles and to define its smoothing length.

2.8.4 ChaNGa: parameter file

Before running a simulation with ChaNGa, a parameter file needs to be edited. This file contains all the information about the general settings of the simulation and about the way particles are treated and physics is implemented. See Figure (2.12) for an example of how parameters are written in the parameter file. If both a parameter and its corresponding value are omitted, a default value of the parameter is selected by the code.

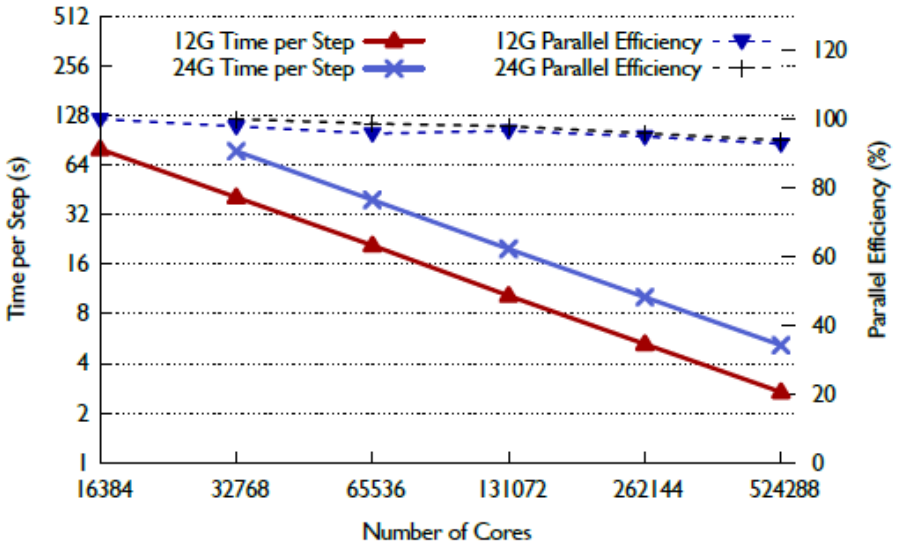

Figure 2.11: Requested time per step (in s) and parallel efficiency as functions of the number of cores used in a simulation run with ChaNGa and using 24 billion particles (thick blue line and thick blue crosses for values of requested time; black dashed line and black crosses for values of parallel efficiency) and 12 billion particles (thick red line and thick red triangles for values of requested time; blue dashed line and blue triangles for values of parallel efficiency) on supercomputer Blue Waters (supported by the National Science Foundation and the University of Illinois). More information about Blue Waters can be found at `http://www.ncsa.illinois.edu/enabling/bluewaters`. Figure from Menon et al. (2015).

Values can be *boolean data*, *signed integers*, *float numbers*, *unsigned integers* or *strings*:

1) boolean data: they can only assume values equal to `0` or `1`. The corresponding parameters are preceded by the prefix `b`;

2) signed integers: they can assume signed integer values, such as `-1`, `3`,... The corresponding parameters are preceded by the prefix `i`;

3) float numbers: they can assume floating values and they are compatible with scientific notation. The corresponding parameters are preceded by the prefix `d`;

4) unsigned integers: they can only assume unsigned integer values, such as `1`, `2`,... The corresponding parameters are preceded by the prefix `n`;

5) strings: their corresponding parameters are preceded by the prefix `ach`.

The order in which parameters are put in the parameter file is not relevant in ChaNGa.

The parameters used to run simulations for this thesis will be discussed in Chapter 3.

```
bPeriodic       = 0     # periodic boundaries: use only for cosmo (usually)
bParaRead       = 0     # read input file in parallel (usually safe)
bParaWrite      = 0     # write outputs in parallel (use only on lustre filesyste
m!)
#iDirector      = 3      # MOVIE: tells Director how many movies to make

#dDumpFrameStep = 0.25

dTheta          = 0.55  # opening angle for gravity (standard value)
dTheta2         = 0.7   # idem (standard value)
#nReplicas       = 1
nBucket         = 16    # number of particles in a "bucket", i.e. leaf of the gr
avity tree


iStartStep      = 1     # starting step number of simulation (for output numberi
ng)
achInFile       = /a_directory/out.000001
achOutName      = /a_directory/out
dDelta  = 0.01          # length of base timestep ("Rung 0") in Gyr
```

Figure 2.12: Extract of the parameter file used with ChaNGa. White characters can be interpreted by the code, blue ones are commented and therefore are not read. On the left, there is the name of each parameter, preceded by the letters `b`, `d`, `n`, `i` and `ach`. After the = sign, there is the value associated to the parameter. The two string parameters are followed by the name of the directories in which input files are read (`achInFile`) and in which output files are written (`achOutName`, respectively).

Chapter 3

N-body simulations of a minor merger between a disk galaxy and a dwarf galaxy

In this Chapter I first discuss the models I used to generate the galaxies.

I also discuss the initial conditions and the main parameters set as input for a minor merger test run with ChaNGa. Then, I present a study of the properties of the code that I could deduce from the test run. This analysis includes the comparison with another simulation done by M. Mapelli using Gasoline code and adopting the same initial conditions and the same galactic models as in the test run with ChaNGa. This simulation performed by M. Mapelli is a low-resolution scaling of a simulation of retrograde co-planar minor merger discussed in MRM15. It is important to have in mind that all the comparisons done between ChaNGa and Gasoline with the test run refer to low resolution performances of both codes.

Finally, I present the initial conditions and the galactic models used to run the main simulations for this thesis.

3.1 Density profiles and distribution functions

How is it possible to describe the distribution of matter - in our case, of a discrete system of particles - in phase-space within a galaxy?

To this purpose, a *distribution function* (DF) can be introduced.

A DF is a function f of the phase-space coordinates ($\vec{x}$,$\vec{v}$) defined so that the quantity:

$$p = f(\vec{x}, \vec{v}) d^3\mathbf{x} d^3\mathbf{v} \tag{3.1}$$

expresses the probability to find a particle within the 6-volume $d^3\mathbf{x}d^3\mathbf{v}$ around position $\vec{x}$ and velocity $\vec{v}$ (Binney & Tremaine 2008).

Once defined a DF, one can integrate over velocities to obtain the spatial density

distribution of particles:

$$\rho(\vec{x}) = \int f(\vec{x}, \vec{v}) d^3\mathbf{v}\,. \tag{3.2}$$

According to the Jeans Theorem[1], given the collisionless Boltzmann equation (CBE):

$$\frac{df}{dt} = \frac{\partial f}{\partial t} + \vec{v} \cdot \frac{\partial f}{\partial \vec{x}} + \dot{\vec{v}} \cdot \frac{\partial f}{\partial \vec{v}}\,, \tag{3.3}$$

f' is a steady-state solution of the CBE, if and only if f' can be expressed as a function of integrals of motions $I_1, ..., I_n$:

$$f' = f'(I_1, ..., I_n), \tag{3.4}$$

where the intergrals of motion in turn depend on $\vec{x}$ and $\vec{v}$:

$$I_i = I_i(\vec{x}, \vec{v}),\ i = 1, ..., n\,. \tag{3.5}$$

3.2 Generating the galactic models and the initial conditions for the test run

In MRM15 both the S0 galaxy and the dwarf companion were modeled as three-component systems, each of them consisting of a dark matter halo, a stellar bulge and a disk of stars and gas. In that particular case, only the dwarf galaxy had gas particles in the disk. Following MRM15, I adopted the three-component models to build the galaxies used in this thesis.

3.2.0.1 Disk density profile

The disk was built following previous models by Kuijken & Dubinski (1995). The DF is:

$$f_d(E_p, L_z, E_z) = \frac{\Omega(R_c)}{(2\pi^3)^{1/2}\kappa(R_c)} \frac{\rho_d(R_c)}{\sigma_R^2(R_c)\sigma_z^2(R_c)} exp\big[- \frac{E_p - E_c(R_c)}{\sigma_R^2(R_c)} - \frac{E_z}{\sigma_z^2(R_c)}\big]\,, \tag{3.6}$$

where R_c and E_c are the radius and the energy of a circular orbit with angular momentum L_z, where Ω and κ are the circular and epicyclic frequencies, respectively, and where σ_z, σ_R and ρ_d are the vertical dispersion of velocities, the radial dispersion of velocities and the disk density, respectively. So, f is a function of three integrals of motion (the energy associated to vertical oscillations E_z, the energy associated to the planar oscillations E_p and the z-component of the angular momentum of the system L_z, respectively). While it is clear that the z-angular momentum of the system is an integral of motion, since total angular momentum is conserved and the disk rotates around its symmetry axis, in the case of E_z and E_p it should be kept in mind that z-dispersion and horizontal dispersion of motions are not the same in the solar neighbourhood (Wielen 1974) and in

[1] Derived by Jeans in 1915.

other galactic disks (Bottema 1993). Hence the necessity of using two more integrals of motion in addition to L_z. I refer the reader to Kuijken & Dubinski (1995) for further details about the disk DF.

The disk mass density is a function of the cylindrical coordinates R and z:

$$\rho_d(R,z) = C_d \exp\left(-\frac{R}{R_d}\right) \mathrm{erf}\left(\frac{R-R_{out}}{\sqrt{2}\delta R_{out}}\right) \exp\Big[-0.8676\frac{\Psi_z(R,z)}{\Psi_z(R,z_d)}\Big], \tag{3.7}$$

where:

$$C_d = \frac{M_d}{8\pi R_d^2 z_d}, \tag{3.8}$$

where R is the radial cylindrical coordinate, z is the vertical cylindrical coordinate, M_d is the disk mass, R_d disk scale length, z_d is the disk scale height, R_{out} is the disk truncation radius, δR_{out} is the sharpness of the truncation and Ψ_z is the vertical potential:

$$\Psi_z(R,z) = \Psi(R,z) - \Psi(R,0). \tag{3.9}$$

The origin of the cylindrical coordinate frame is the galactic centre, while the symmetry axis of the frame is the disk symmetry axis. This equation represents the distribution of mass density in a disk which is truncated at radius R_d and has a $sech^2(z)$ dependence on vertical coordinate.

3.2.0.2 Bulge density distribution

The DF for the bulge is given by the following expression for spherical systems (Widrow et al. 2008):

$$f_b(\epsilon') = \frac{1}{\sqrt{8}\pi^2}\int_0^{\epsilon'} \frac{d^2\rho_b}{d\Psi_{tot}^2}\frac{d\Psi_{tot}}{\sqrt{\epsilon'-\Psi_{tot}}}, \tag{3.10}$$

where ρ_b is the density distribution of the bulge, where $\epsilon' = -E$, being E the energy of the system, and where ψ_{tot} is the potential of the system.

The density profile is:

$$\rho_b(r) = \sigma_b\left(\frac{r}{R_e}\right)^{-p} \exp\left[-b\left(\frac{r}{R_e}\right)^{1/n}\right], \tag{3.11}$$

where R_e is the effective radius of the bulge (i.e. the radius which includes half the total projected mass or light), n and p are free parameters, b is fixed according to the definition of R_e and σ_b is given by:

$$\sigma_b = \{4\pi n b^{n(p-2)}\Gamma R_e^2 \rho_b\}^{1/2}, \tag{3.12}$$

being Γ a function of n and p, $\Gamma = \Gamma[n(2-p)]$. This density profile reproduces the Sérsic profile for the projected surface density Σ (Sersić 1963):

$$\Sigma(r) = \Sigma_0 \exp\left[-b\left(\frac{r}{R_e}\right)^{1/n}\right], \tag{3.13}$$

assumed that $p = 1 - 0.6097/n + 0.05563/n^2$ (Terzić & Graham 2005).

Previous bulge density profiles were proposed by Kuijken & Dubinski (1995), using a King model for the bulge, and by Widrow & Dubinski (2005), in the form of a Hernquist bulge.

3.2.0.3 Halo density distribution

The DF for the halo is given similarly to Equation (3.10; Widrow et al. 2008):

$$f_h(\epsilon') = \frac{1}{\sqrt{8}\pi^2}\int_0^{\epsilon'} \frac{d^2\rho_h}{d\Psi_{tot}^2}\frac{d\Psi_{tot}}{\sqrt{\epsilon' - \Psi_{tot}}}, \tag{3.14}$$

where ρ_h is the density distribution of the halo.

The halo density profile is then:

$$\rho_h(r) = \frac{2^{2-\gamma}\sigma_h^2}{4\pi a_h^2}\frac{1}{(r/a_h)^\gamma(1+r/a_h)^{3-\gamma}}C(r, r_h, \delta r_h), \tag{3.15}$$

where a_h is the scale radius of the bulge, σ_h is the scale velocity, γ is the cusp parameter of the halo, r_h and δr_h are the halo truncation radius and truncation interval, and C is the truncation function, defined as

$$C(r, r_h, \delta r_h) = \begin{cases} \frac{1}{2}\mathrm{errf}(\frac{r-r_h}{\sqrt{2}\delta r_h}) & \text{if } r < r_h; \\ 0 & \text{if } r \geq r_h\ . \end{cases} \tag{3.16}$$

Previously, Kuijken & Dubinski (1995) modeled the halo using a lowered Evans model, while Widrow & Dubinski (2005) adopted a modified version of the Navarro-Frenk-White (NFW) halo (Navarro et al. 1996):

$$\rho_{NFW}(r) = \frac{\rho_h}{(r/a_h)(1+r/a_h)^2}, \tag{3.17}$$

where all the quantities are defined as in Equation (3.15). The NFW halo has the advantage to be related to the theoretical cosmological predictions about the formation of galaxies[2]. However, this model does not take into consideration cuspier cores, such as those obtained by Moore et al. (1999)[3].

[2]The more general framework in which one finds NFW halos is the so-called Λ-*cold-dark-matter* Universe or ΛCDM Universe.

[3]Furthermore, there is evidence that in elliptical galaxies such as NGC 1281 a NFW halo could not always be the best model to describe the dark matter density profile (Yildirim 2016).

3.2.0.4 Combining the three components

Each of the three models described above is independent from the others. Modeling an equilibrium three-component galaxy requires to substitute the original DFs f_d, f_b and f_h with the new DFs f'_d, f'_b and f'_h, respectively, that are modified from the previous ones in order to obtain a total DF f_{tot}:

$$f_{tot} = f'_d + f'_b + f'_h \,, \tag{3.18}$$

that is as much as possible near to equilibrium. An iterative process can be used to find the f_{tot} that better approximates the equilibrium condition and that minimizes the error.

3.2.1 Filling the models with particles

In practice, the DFs described above and the corresponding N-body models are implemented as follows[4]. First of all, for each model one chooses the parameters that describe the different DFs. Then, the gravitational potential is calculated taking these parameters into account. From the potential, using Poisson Equation (2.35), one derives the corresponding DF for the three galactic components. At this point, it is possible to fill the phase-space with particles so that they reproduce the obtained DFs of disk, bulge and halo.

3.2.1.1 Acceptance-rejection method

Before describing the process of particle filling, it is useful to quickly revise what the acceptance-rejection method is. The method works as follows:

1) given a quantity x and a generic DF $g(x)$, this DF is substituted with a corresponding DF $f(x)$ which is simpler to integrate, with $f(x) > g(x)$;

2) the new DF is integrated to give the corresponding cumulative distribution function $F(x)$ for x in the range $[x_1, x_2]$:

$$F(x) = \int_{x_1}^{x} f(x)dx \,; \tag{3.19}$$

3) for the i-th particle of the system, a random number F_i is generated between the maximum and the minimum value of F in the given range. The corresponding value of the variable (x_i) is obtained from F_i inverting $F(x)$, i.e. $x_i = F_i^{-1}$. Repeating this for all particles, it is possible to sample the distribution function $f(x)$;

4) for the i-th particle, a second random number is generated between a minimum and a maximum value of f. If this number is larger than the original DF evaluated at x_i, then the particle is rejected. Otherwise, the particle is accepted. In this way, the remaining particles follow the distribution dictated by the original DF.

[4]The routine used to generate the models was `GalactICS`, with its last update by J. Dubinski.

3.2.1.2 Sampling the three components

The bulge and the halo of a galaxy are axisymmetric and the DF is a function of R and z. These two components are filled as follows (Kuijken & Dubinski 1994; 1995):

1) first, the density is sampled by calculating the spatial coordinates of each particle;

2) once the density is sampled, the local maximum of the DF is calculated at the position of each particle (and at a corresponding zero velocity of the particle itself);

3) the velocities of each particle are calculated by inversion of the corresponding potential. The corresponding total energy is calculated and in turn the DF is calculated for that value of total energy. This value of DF, DF', is compared with a random number generated between 0 and the local maximum value of DF. The particle is finally accepted if DF' is larger than the random number, otherwise the particle is rejected.

As to the disk, the previous iteration is repeated with some differences. In fact, in order to calculate the local maximum for the DF, not only is the density sampled starting from the spatial coordinates of the particles, but also the tangential velocity v_ϕ is used to find this local maximum. In fact, this maximum occurs for tangential velocities different from zero and for radial and vertical velocities equal to zero. Once done this, the proceeding is the same as described above.

3.3 Test run: comparison between ChaNGa and Gasoline

Before discussing my simulations, I am going to present a preliminary test run executed with ChaNGa. In this test I used the same initial galactic models and the same initial conditions of a previous test run made in Gasoline[5]. What is the importance of this comparative test? In Chapter 2 I have already discussed the basic differences and similarities between the two codes. The idea is that, by comparing and studying the outputs of a simulation performed with the same initial conditions for the two codes, one can deduce other relevant differences in the way ChaNGa and Gasoline work. The galactic models and the initial orbital conditions for the dwarf galaxy in the test run are discussed in Subsections (3.3.2) and (3.3.3), respectively.

3.3.1 ChaNGa: relevant parameters

I have already discussed the general properties of the parameter file used to run simulations with ChaNGa. I am going to add further details about the parameters used for the code.

[5]The test run made with Gasoline was performed by M. Mapelli, as a low resolution version of the simulation of co-planar retrograde minor merger in MRM15

1) the maximum number of particles in each leaf of the tree was put equal to 16. As mentioned in Chapter 2, CHANGA permits in fact to choose the maximum number of particles per leaf;

2) I choose a base time-step of 0.01 Gyr between two subsequent outputs. A maximum number of 21 subdivisions in sub-time-steps was selected;

3) as already discussed, it is possible to attribute a different behaviour to gas (cooling mechanism, adiabatic behaviour and isothermal behaviour). I activated the cooling option for the test run. However, no limit was imposed to gas temperatures;

4) as to the implementation of the SPH method, I used a number of neighbours $N = 32$;

5) the maximum temperature allowed to activate SF is $T_{max} = 3 \times 10^4$ K;

6) in strongly rotating systems, it is better to let the code use a viscosity limiter (Balsara switch; Balsara 1995) that diminishes the viscosity acceleration for particles i and j by the factor $f_{ij} = |f_i + f_j|/2$, where f_i is defined as:

$$f_i = \frac{\nabla \dot{\vec{v}_i}}{|\nabla \dot{\vec{v}_i}| + |\nabla \times \vec{v_i}| + 0.0001 c_{s,i}/h_i}\,, \tag{3.20}$$

with all the quantities defined as in the previous Chapter. The curl at denominator better regulates viscosity in shearing and obliquely shocked flows (Steinmetz 1996).

7) The energy released by SN explosions is 0.8×10^{51} erg. The *blastwave* mechanism (Stinson et al. 2006) is implemented to avoid gas overcooling while star particles release energy through SN events. In this way the released energy is not dramatically lost by the system.

3.3.2 Galactic models for the test run

In Table (3.1) I write the main parameters that define the galactic models of the main galaxy and the dwarf galaxy for the test run. For both simulations, these parameters are nearly the same as the ones used in MRM15. As already said, there is no gas mass in the main galaxy. Furthermore, this simulation is at an intermediate/low resolution, with 600.000 disk particles, 100.000 bulge star particles and 200.000 dark matter particles for both galaxies. In the main galaxy, all disk particles are star particles, while in the dwarf galaxy 1/10 of disk particles is actually represented by gas particles and the remaining part is represented by star particles. In the main galaxy, dark matter particles have a mass of $\sim 10^5\ M_\odot$, while star particles have a mass of $\sim 10^4\ M_\odot$. In the dwarf galaxy, dark matter particles have a mass of $\sim 10^4\ M_\odot$, while star and gas particles have a mass of $\sim 10^3\ M_\odot$.

model parameter	main galaxy	dwarf galaxy
M_{DM} (10^{11} $M_\odot$)	7.0	0.3
M_s (10^{10} $M_\odot$)	7.0	0.2
$f_{b/d}$	0.25	0.25
M_G (10^8 $M_\odot$)	0	1.38
R_s (kpc)	6.0	3.0
R_d(kpc)	3.7	3.0
h_d (kpc)	0.37	0.30
r_b (kpc)	0.6	0.6

Table 3.1: Parameters defining the models of the two galaxies in the test run (from MRM15). The names of the parameters are in the *left-hand* column. In the *central* column and in the *right-hand* column the corresponding values for the main galaxy and the dwarf galaxy are written, respectively. M_{DM} is the dark matter mass, M_s is the stellar mass, $f_{b/d}$ is the bulge-to-disk mass ratio, M_G is the gas mass, R_s is the halo scale radius, R_d is the disk scale length, h_d is the disk scale height and r_b is the bulge scale radius.

3.3.3 Initial conditions for the test run

In Table (3.2) I present the parameters for the initial orbit of the dwarf galaxy for the test run (again, similar for both simulations to the ones used in MRM15). The dwarf galaxy is in a parabolic orbit, slightly hyperbolic ($e \sim 1.003$). The orbit is retrograde, as some of the runs performed in MRM15. The halos of both galaxies penetrate a bit one each other at their outer edges, but this fact is irrelevant since no tidal deformation is observed in the two models.

In Figure (3.1) I show some screens capturing the initial configuration of the system for the test run.

3.3.4 Gas temperature and density

I sampled the distribution in temperature and density of all gas in the two simulations every 0.5 Gyr, starting at time $t = 0.1$ Gyr and going to time $t = 4.1$ Gyr. Figure (3.2) captures the two galaxies approaching the merger at the epoch of 0.6 Gyr from the beginning of the simulation with ChaNGa.

3.3.4.1 Average temperature and density

Figure (3.3) shows the average values of temperature T and density ρ and their relative difference for the selected outputs of both runs. Mean values of temperature are higher in ChaNGa than in Gasoline. However, this is a modest difference. Also, the general trend of the two temperature values is similar for both simulations, with an increase in the mean value of T from $t = 0.6$ Gyr to $t = 4.1$ Gyr. This difference in temperatures

D (kpc)	b (kpc)	v_{rel} (km s^{-1})	θ	ϕ	ψ	E_s (10^4 km^2 s^{-2})	L_s (10^3 km s^{-1} kpc)	e
200	10	200	-π/2	0	0	0.38	2.0	1.003

Table 3.2: Parameters defining the initial orbit of the dwarf galaxy in both test runs. D is the distance between the mass centres of the two galaxies, b is the impact parameter, v_{rel} is the modulus of the relative velocity vector $\vec{v}_{rel}$, θ, ϕ and ψ are the angles of the orbit, E_s is the specific energy (i.e. per unit reduced mass), L_s is the modulus of the specific orbital angular momentum of the dwarf galaxy, e is the eccentricity of the orbit. The three angles are defined as in MRM15 and in Hut & Bahcall (1983): θ is the angle between $\vec{v}_{rel}$ and the symmetry axis of the main galaxy; ϕ is the orientation of $\vec{v}_{rel}$ projected on the plane of the primary galaxy, ψ is the orientation of the distance vector $\vec{D}$ projected on the plane perpendicular to $\vec{v}_{rel}$. The reduced mass is $\mu = m_1 m_2/(m_1 + m_2)$, with m_1 and m_2 the mass of the main galaxy and of the dwarf galaxy, respectively. The specific energy is $E_s = -GM/D + {v_{rel}}^2$, with $M = m_1 + m_2$. The orbital eccentricity is $e = [1 + 2E_s {L_s}^2/(GM)^2]^{1/2}$.

may be due to the fact that the cooling algorithm in ChaNGa is less effective than that in Gasoline. This means that gas tends to cool less and to dissipate less energy in the case of ChaNGa.

As to the density, the corresponding values have a more marked half-difference-to-mean-value ratio, with a maximum of 0.9 at 3.1 Gyr. What is a possible explanation for this divergence in density values for ChaNGa and Gasoline? Let us consider the evolution of the distance between the mass centres of the two galaxies through time for both simulations (Figure 3.4). The first passage at periapsis (i.e. the first instant of minimum distance between the two galaxies) occurs at $t \sim 0.7$ Gyr for both runs. After this epoch, the distance values tend to be slightly different. In particular, in Gasoline the other passage to periapsis occurs before the corresponding one in ChaNGa. At time $t \sim 3.1$ Gyr, while in ChaNGa the dwarf galaxy has just approached its second passage to periapsis, in Gasoline the dwarf galaxy has already passed for the second time through the periapsis about ~ 0.1 Gyr before. This explains the fact that the average values of gas density are so different at 3.1 Gyr between the two runs: in the case of ChaNGa at this epoch there is another passage of the dwarf at peripasis, so gas is forced to stay in denser regions and is more compressed. Hence the higher value of density at 3.1 Gyr. In contrast, in the case of Gasoline at 3.1 Gyr the passage at periapsis has just happened, so now gas is far from the condition of compression and its densities are lower than in ChaNGa. Furthermore, the fact that the subsequent passages at periapsis happen later in ChaNGa than in Gasoline can be explained by considering that on average gas has higher temperatures in the case of ChaNGa. As a consequence, gas dissipates less energy in cooling and the whole system loses less energy in general. This acts in favor of a delay in the epochs of the subsequent periapsis passages.

3.3.4.2 Anomalous gas cooling at low temperatures and densities

One of the biggest problems in the behaviour of gas is represented by the cooling mechanism.

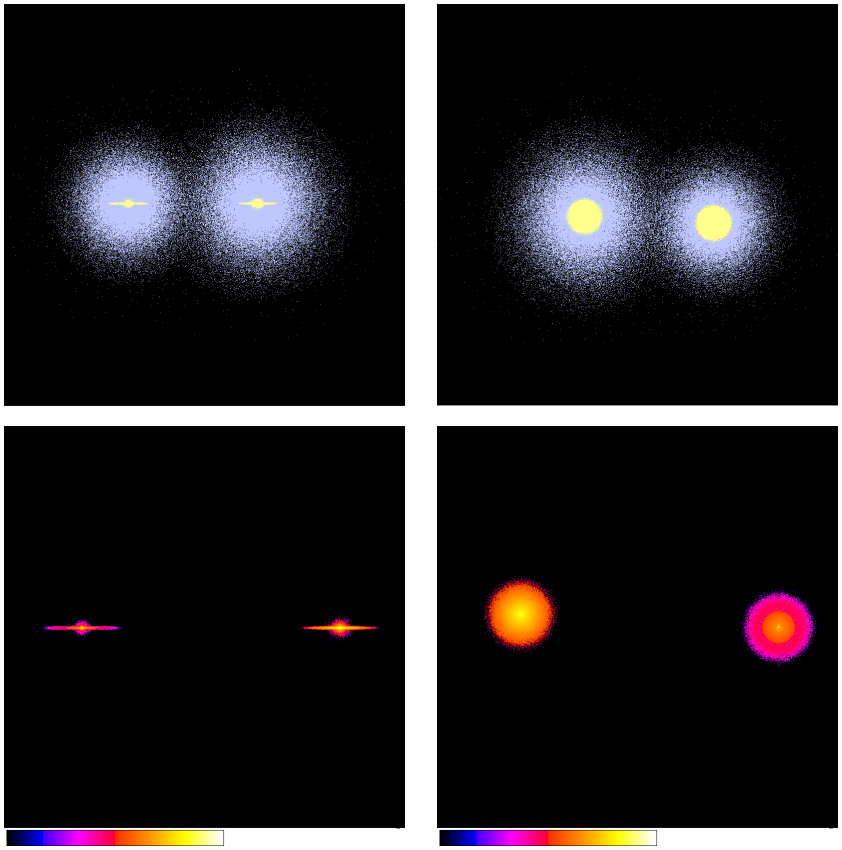

Figure 3.1: *Top* panels: y-projected view (*left*) and z-projected view (*right*) of the initial condition of the test run. The light-grey particles are dark matter particles and the yellow particles are star particles. *Bottom* panels: y-projected (*left*) and z-projected (*right*) logarithmic contour plot of stellar densities of the initial condition of the test run. Each top panel measures $\sim 600 \times 600$ kpc^2, while each bottom panel measures 300×300 kpc^2. For each output, axes in its z-projected view are always oriented as follows: the x axis is rightward oriented, the y axis is upward-oriented. As to the y-projected view, the x-axis is leftward-oriented and the z axis is upward oriented. The color codes for these logarithmic maps go from black to white (lower and higher values of the plotted quantity, respectively).

Given a virialized system like the dwarf galaxy used for both simulations, gas is initially in equilibrium with the system at a given temperature T. For a system such as a galaxy, gas equilibrium temperatures are of the order of $\sim 10^4$ K. As the dwarf galaxy is tidally stripped because of the gravity exerted by the main galaxy, gas is heated and its temperatures tend to increase towards higher values. By doing this, the less dense gas regions will be distributed around the main galaxy to form a new halo in thermal equilibrium with the main galaxy at temperatures of the order of $10^5 \div 10^6$ K. Meanwhile, another part of gas tends to cool and to accrete on possibly different structures (a disk, a ring, ecc.) on the main galaxy. These structures are denser ($\rho \sim 10$ atoms cm^{-3}) than the halo in which gas is distributed ($\rho << 1$ atoms cm^{-3}) . This gas component is expected to have temperatures near $10^3 \div 10^4$ K, because no recipes for molecular

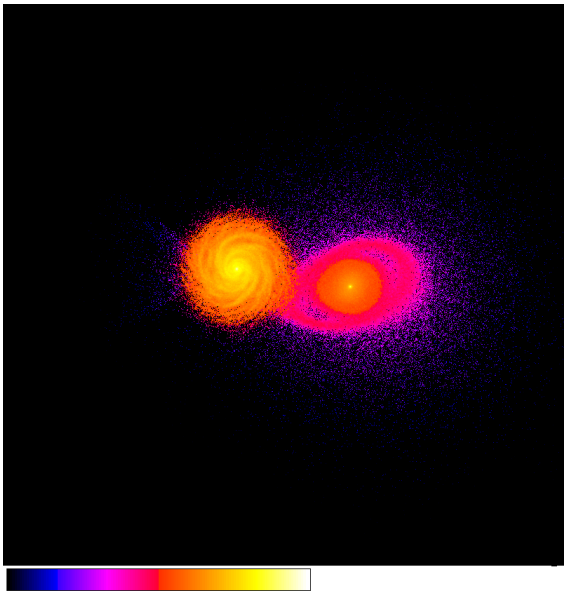

Figure 3.2: z-projected logarithmic contour plot of the spatial distribution of stellar densities at time 0.6 Gyr, about 0.1 Gyr before the first periapsis passage. The disk of the dwarf galaxy is being deformed by the tidal interaction with the main galaxy. The panel measures 233 x 233 kpc^2.

and dust cooling are included. As it was said in the previous Chapter, in galaxy-size simulations the most relevant gas cooling processes happen above a limit temperature of 10^4 K. This means that, even allowing gas to cool below 10^4 K as a limit situation, one cannot expect any process permitting further cooling below $\sim 10^3$ K, especially at low densities ($\lesssim 1$ atoms cm^{-3}).

The test simulations however show a different cooling behaviour of gas. Gas masses cooling down to temperatures $T < 10^3$ K are compared for the two codes (Figure 3.5). As it is possible to see, in both cases gas shows an anomalous cooling below these temperatures. In particular, apart from the time interval between 0.9 Gyr and 2.0 Gyr, in which gas cooling in ChaNGa dominates, it is Gasoline that produces more cooling, especially at 3.4 Gyr. In Table (3.3) I show which percentage the number of gas particles

t (Gyr)	0.1	0.6	1.1	1.6	2.1	2.6	3.1	3.6	4.1
$f_{T<10^3\mathrm{K,ChaNGa}}$	0.00	0.01	12.87	17.44	19.01	20.34	21.76	22.75	23.60
$f_{T<10^3\mathrm{K,Gasoline}}$	0.00	0.08	9.34	14.95	19.27	24.59	29.46	32.24	31.53

Table 3.3: Fraction $f_{T<10^3\mathrm{K}}$ of gas particles with temperatures below 10^3 K for both simulations at different epochs. *First raw*: output times; *second raw*: fraction of particles in ChaNGa with temperatures below 10^3 K; *third raw*: fraction of particles in Gasoline with temperatures below 10^3 K.

below 10^3 K corresponds to.

It is clear that the gas particles that cool down to $T < 10^3$ K are also the ones that are placed in less dense environments (Figure 3.6). Furthermore, one can observe from both

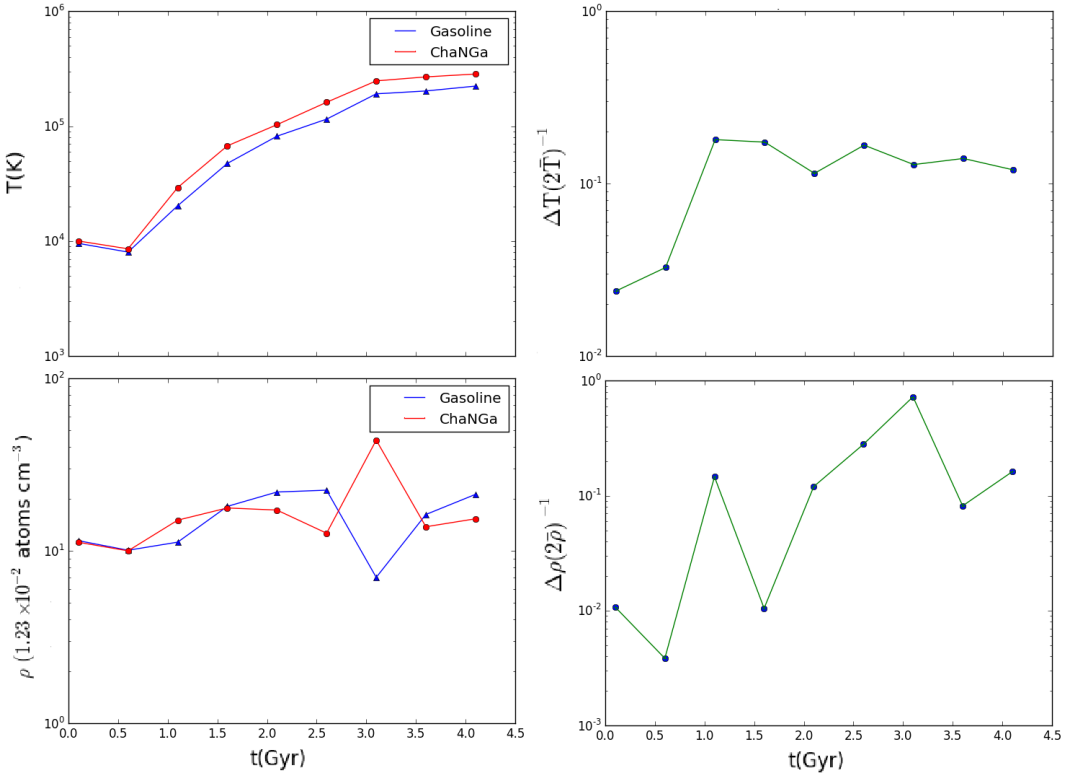

Figure 3.3: Evolution in time of gas temperature and density for both simulations from 0.1 Gyr to 4.1 Gyr with time interval of 0.5 Gyr. *Top-left* panel: average gas temperatures. *Top-right* panel: relative difference in the average temperatures of the two codes divided by their mean value. *Bottom-left* panel: average gas densities. *Bottom-right* panel: relative difference in the average densities of the two codes divided by their mean value.

histograms and contour plots that gas is heated even at $10^7 \div 10^8$ K. These temperatures are higher than the ones expected for a simulation involving galaxies only (that are of the order of $\sim 10^6 \div 10^7$ K). Given these results and considered that gas is not expected to cool below 10^3 K, what is a possible explanation for this behaviour? Probably, the code does not work perfectly at galactic-scale simulations. While at cosmological scales this type of cooling would be avoided thanks to the generally higher temperatures of the simulated system, at galactic scales the code may have problems in keeping gas above the expected limit of 10^3 K. Later in this Chapter I discuss a simple solution to avoid the anomalous behaviour of gas at lower and higher temperatures.

3.3.5 Energy and angular momentum

I compared kinetic energy $E_{kin} = \sum_{i=1}^{N} \frac{1}{2} m_i {v_i}^2$, potential energy $E_{pot} = \sum_i E_{pot,i}$ and total energy $E_{tot} = E_{kin} + E_{pot}$ of the whole system for both simulations at the same

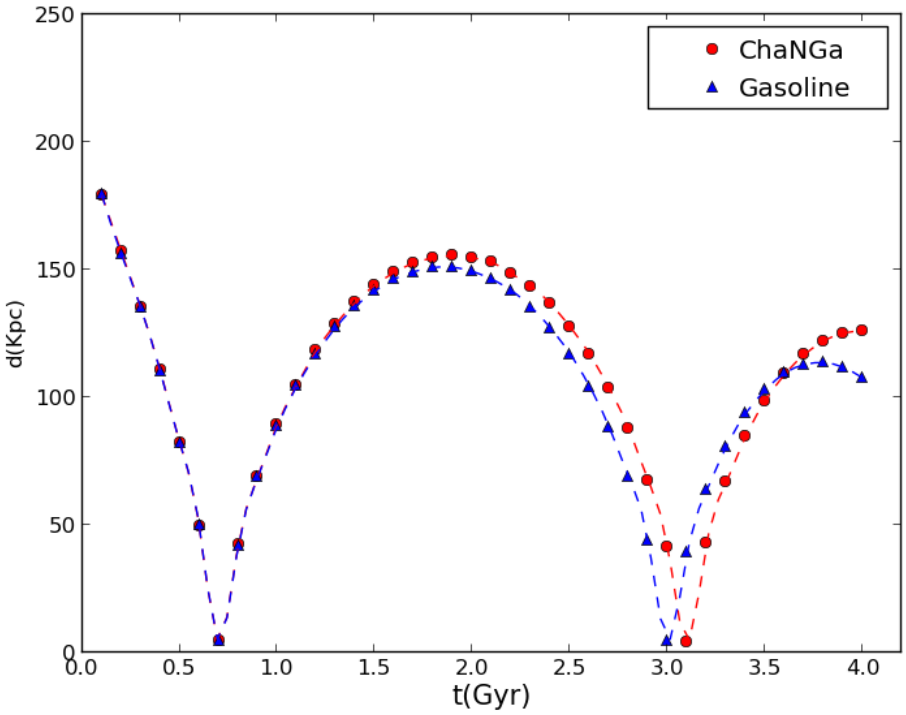

Figure 3.4: Distance between the mass centers of the main galaxy and of the dwarf galaxy as a function of time for both simulations. The time interval between a value and another is of 0.1 Gyr. The points were interpolated with a cubic spline.

outputs considered previously (Figure 3.7), with $i, j = 1, ..., N$, with m_i and v_i the mass and velocity of the i-th particle, respectively, and with $E_{pot,i}$ the potential energy of the single particle.

For the same times, I also calculated the differences between these values relative to their mean value (Figure 3.8). For the case of the kinetic energy, this relative difference is < 0.01, while for the case of potential and total energy this value is a bit larger at $t = 3.1$ Gyr. In fact, as already said, at this epoch there is the third passage to periapsis in ChaNGa, while the same situation has happened at time t =3.0 Gyr in Gasoline. Hence, potential and total energy are lower in ChaNGa because the corresponding system is more bound.

I isolated particles with a kinetic energy larger than 6.5×10^{60} erg, to check whether they represented or not a substantial part of the whole system of particles. In both ChaNGa and Gasoline this fraction of particles accounts for no more than $\sim 9\%$ of the whole particles. This means that there is no relevant fraction in the number of particles that are spuriously scattered. In Table (3.4) I write the fraction of particles having high energies for each of the considered epochs.

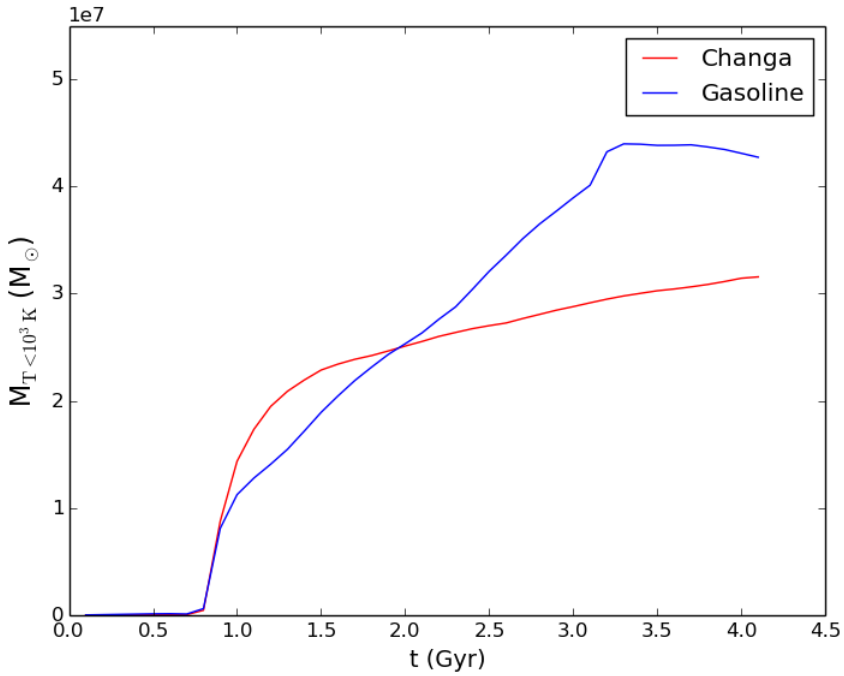

Figure 3.5: Gas mass that cools below 10^3 K plotted as a function of time for both simulations. The time-step from an output to the other is equal to 0.1 Gyr.

As to the total angular momentum, a similar analysis shows that no great differences emerge between the two runs (Figure 3.9).

What about the conservation of total energy and of total angular momentum in ChaNGa?

I plotted the relative difference in the values of E_{tot} and L^2 (Figure 3.10) between many consecutive outputs in the test run. While angular momentum does not show any relevant variation through the evolution of the system, in the case of the total energy it is possible to observe a variation in its value at the times corresponding to the two passages at periapsis. However, this variation is counter-balanced at the following outputs and the previous value of total energy is nearly restored. It is also possible to observe that total energy decreases a bit from one output to the other because of energy dissipation via gas cooling.

3.3.6 Star Formation and Star Formation Rate

I compared the SF and SFR produced by both codes. In Figure (3.11) I show the trend of SFR and of cumulative SF as functions of time for a set of 11 snapshots, with a time interval $\Delta t = 0.4$ Gyr from one output to the other. This temporal binning was selected in order to smooth the excessive fluctuations in the values of SFR and cumulative SF. The

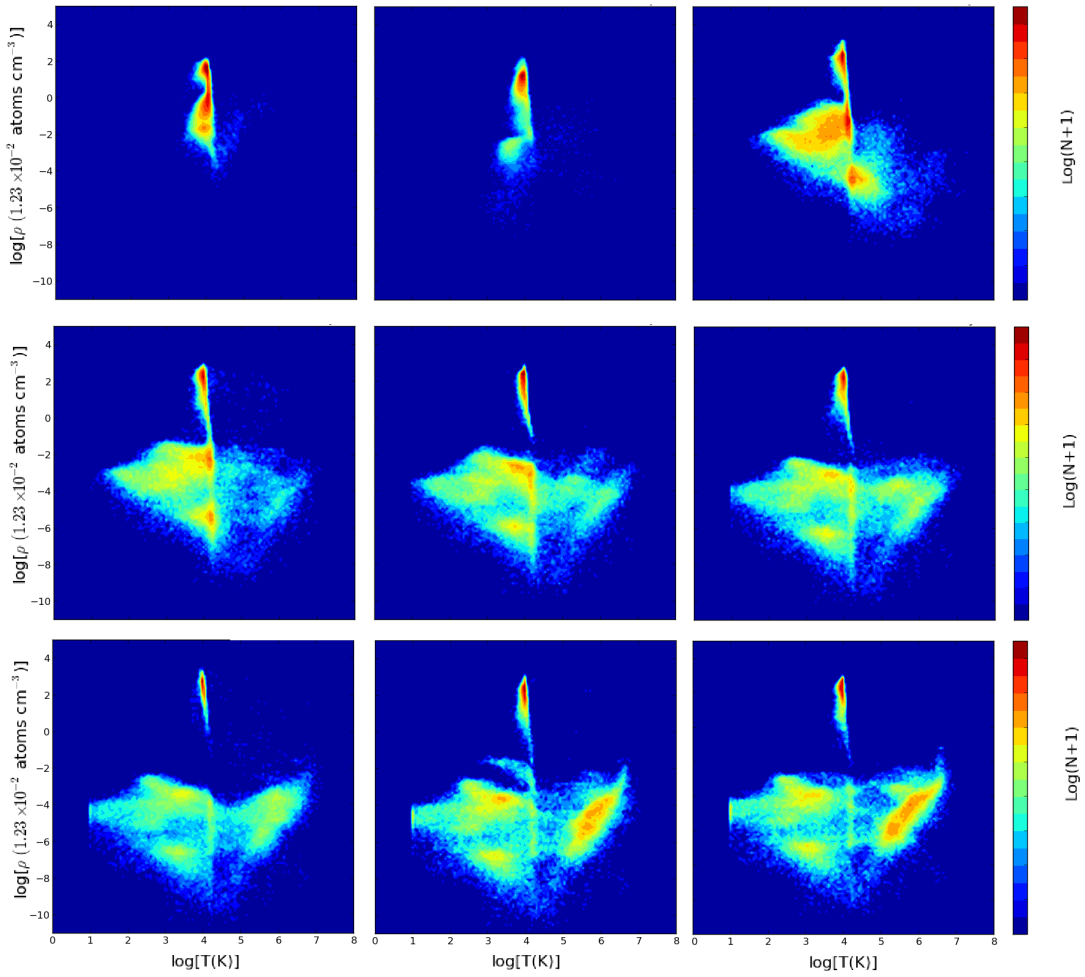

Figure 3.6: Color-coded logarithmic contour maps showing the distribution of gas particles in the logarithmic temperature-density plane for the simulation run with ChaNGa at different epochs from the beginning of the simulation, from (*top-left*) 0.1 Gyr to 4.1 Gyr with a time interval of 0.6 Gyr. The color code goes from lower numbers of particles (dark blue) to higher numbers of particles (red/brown).

conclusion is that ChaNGa produces more SF than Gasoline, and that both simulations produce most SF at time $t = 0.6$ Gyr (first periapsis passage). Why such a greater value of SF at the first periapsis passage? For certain, the first passage at periapsis activates SF by compressing gas. Maybe, once the first impact has happened and now that gas is accreting on the main galaxy, the survived nucleus of the dwarf galaxy has not such a large remaining mass to impact violently again on SF when the dwarf galaxy approaches the main galaxy again. Consequently, the subsequent episodes of SF are less intense.

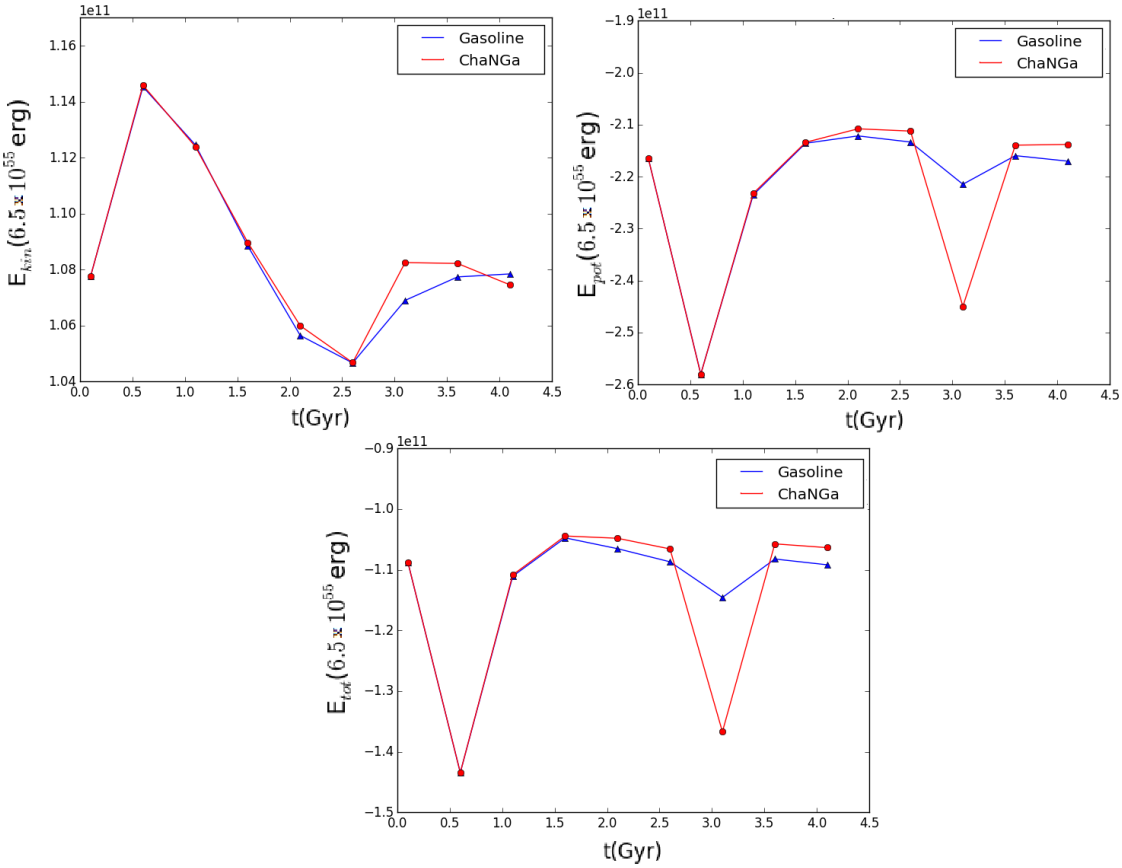

Figure 3.7: Kinetic energy (*top-left* panel), potential energy (*top-right* panel) and total energy (*bottom* panel) as functions of time for both simulations, from 0.1 Gyr to 4.1 Gyr with a time-step of 0.6 Gyr.

3.4 Generating the models for the 4 runs

Now that I have discussed some of the differences in the outputs produced by ChaNGa and Gasoline, I will turn to the presentation of the models and the initial conditions generated for the simulations discussed in this thesis.

I ran a total number of four simulations. Each of them reproduces a minor merger between a disk galaxy and a dwarf galaxy. I varied initial conditions and/or properties of the galactic models to test how these variations produce differences in the final results. In particular, the relevant difference with respect to MRM15 is the presence of gas in the disk of the main galaxy. In MRM15, on the contrary, the disk galaxy was completely gas-depleted. So, this thesis considers the more realistic case of dealing with disk galaxies that have different quantities of gas in their disk. Also, this is done in order to study gas accretion and the possibility to form counter-rotation via retrograde minor mergers.

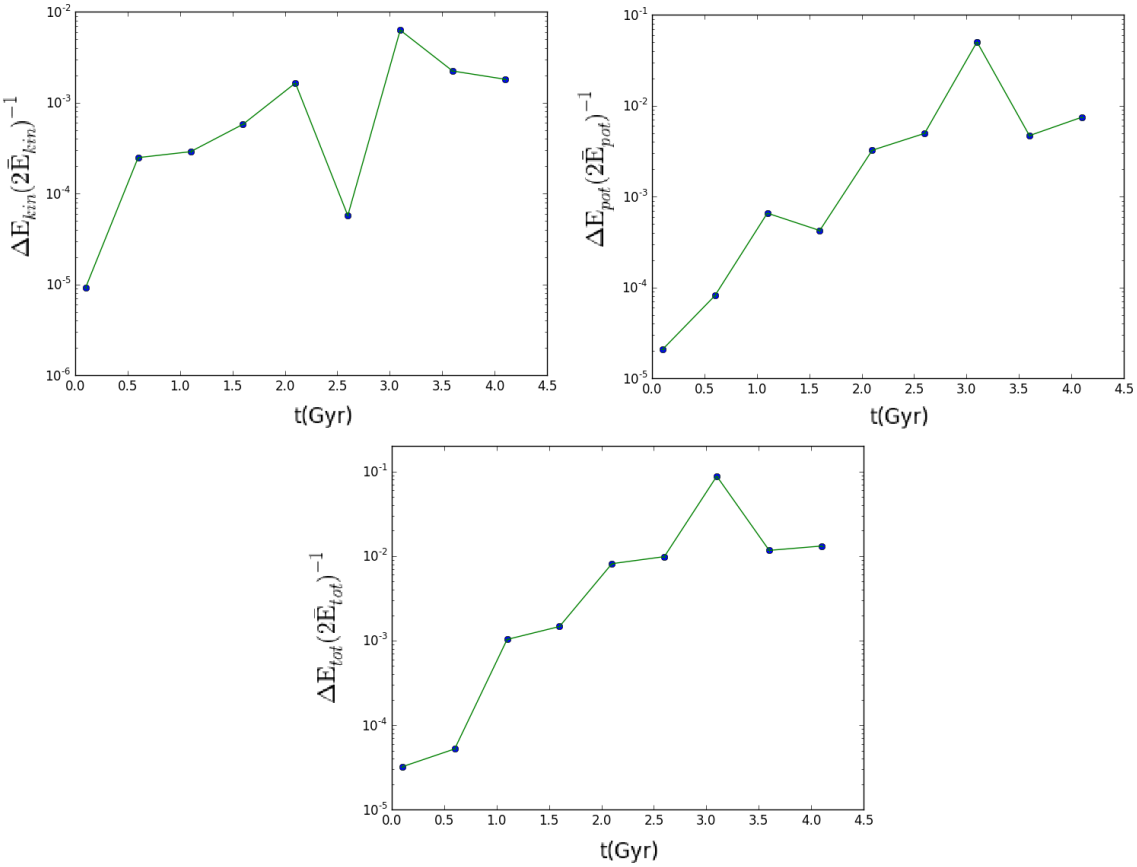

Figure 3.8: Relative errors between the two simulations for kinetic energy (*top-left* panel), potential energy (*top-right* panel) and total energy (*bottom* panel) as functions of time, from 0.1 Gyr to 4.1 Gyr with a time-step of 0.6 Gyr.

3.4.1 Selection of galactic models

As I previously said, in order to build a complete galactic model, one has to combine DFs for halo, disk and bulge. Gas is introduced by simple conversion from stellar particles in the disk. In my case, the stellar particles are converted in gas particles as follows:

1) one chooses a number f corresponding to the fraction of disk particles to be converted in gas particles;

2) a random number m between 0 and 1 is generated for each star particle. The particle is then converted into a gas particle if $m < f$.

This is done until the requested number of gas particles is not obtained. Also, since the conversion of star particles into gas particles is randomly generated, in this way one avoids biases in the distribution of gas particles. Which galactic models were used for

t (Gyr)	0.1	0.6	1.1	1.6	2.1	2.6	3.1	3.6	4.1
f_h(ChaNGa)	9.08	9.30	9.32	9.32	9.07	8.98	9.45	9.27	9.33
f_h (Gasoline)	9.08	9.31	9.31	9.31	9.07	8.98	9.14	9.34	9.42

Table 3.4: Fraction f_h of particles at kinetic energies greater than 6.5×10^{60} erg for both simulations at different epochs. *First raw*: times of the considered outputs; *second raw*: fraction of particles with kinetic energies greater than 6.5×10^{60} erg in ChaNGa; *third raw*: fraction of particles with kinetic energies greater than 6.5×10^{60} erg in Gasoline.

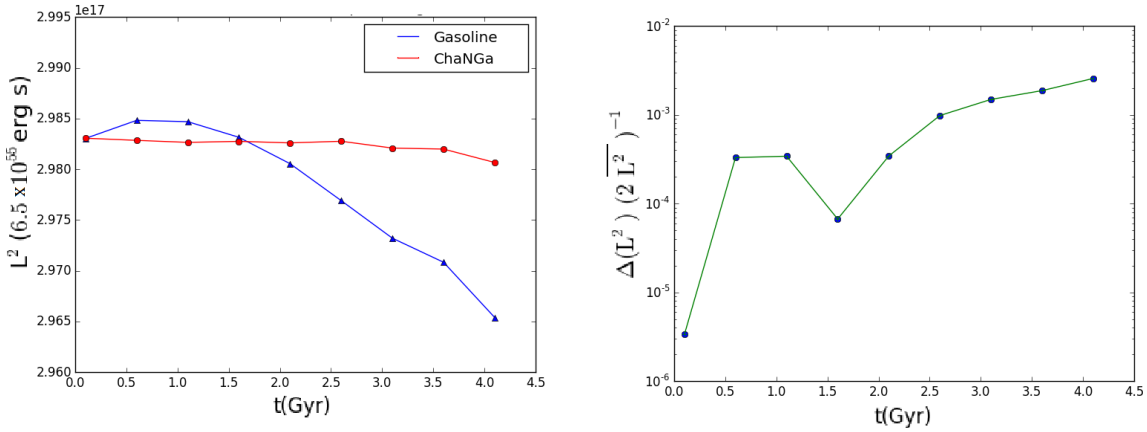

Figure 3.9: *Left* panel: square angular momentum as a function of time for both simulations. *Right* panel: relative difference between two outputs of the two simulations with respect to their mean value as a function of time.

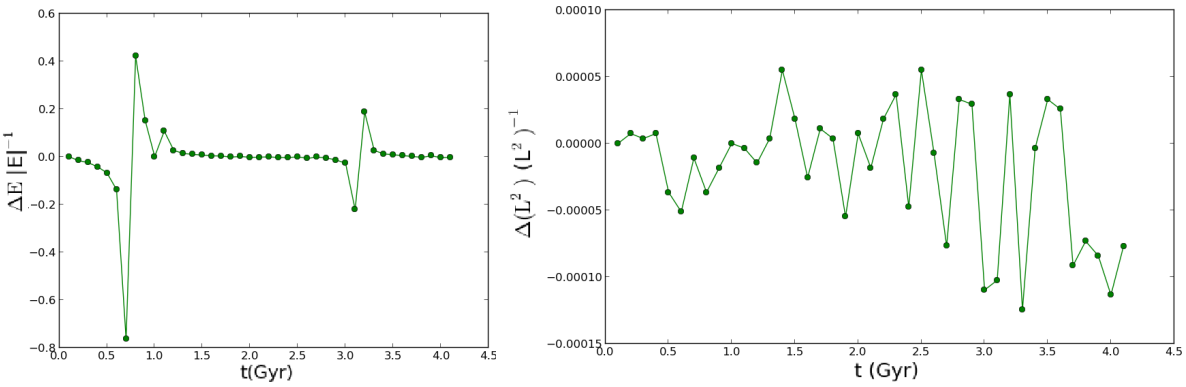

Figure 3.10: Variation of total energy (*left* panel) and of square angular momentum (*right* panel) between consecutive outputs in the test run with ChaNGa.

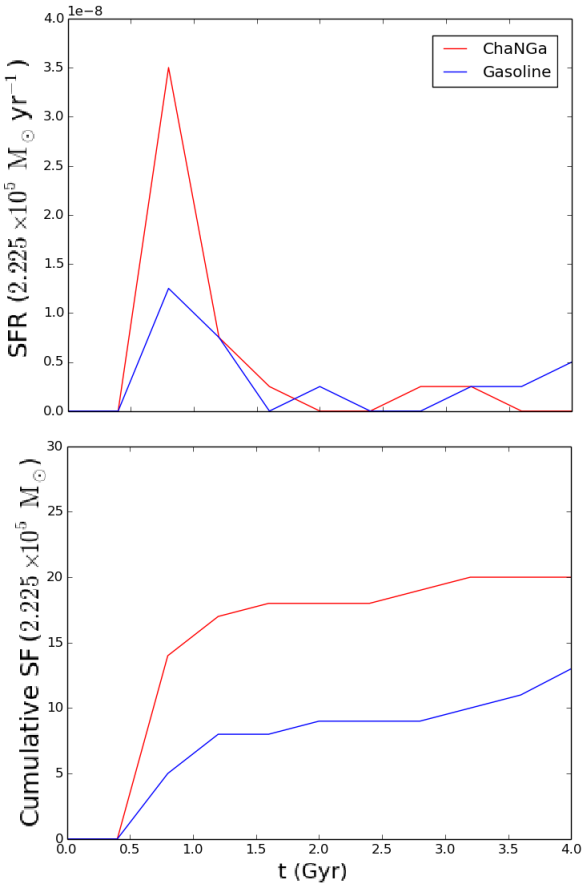

Figure 3.11: SFR (*top* panel) and Cumulative SF (*bottom* panel) as functions of time for both codes.

my simulations? In the first run (hereafter R1) I simulated a disk galaxy and a dwarf galaxy. Both of them have a bulge, a disk and a halo. The main galaxy is much more massive than the dwarf galaxy, but the dwarf galaxy is more rich in gas (i.e the gaseous disk is more massive in the dwarf galaxy than in the main galaxy).

In the second run (R2) I simulate the same galaxies as in R1, except that the main galaxy has more gas than the dwarf galaxy.

In the third run (R3) the main galaxy is chosen to be equal to the one in R2. However, the dwarf galaxy is composed of a halo and a bulge, without a disk. No gas is added in it. So, in R3 the dwarf galaxy is a dwarf spheroidal.

Finally, for the last run (R4) I use the same models as in R1.

In all simulations, there are 2M dark matter halo particles, 2M disk particles (some of them were converted in gas particles as for the test run) and 400.000 bulge particles. Dark matter particles in the main galaxy have a mass of $\sim 10^5\ M_\odot$, while star particles and gas particles have a mass of $\sim 10^4\ M_\odot$. For the dwarf galaxy, the dark particles have

a mass of $\sim 10^4\ M_\odot$, while gas and star particles have a mass of $\sim 10^3\ M_\odot$. In Table

	R1		R2		R3		R4	
model parameter	main	dwarf	main	dwarf	main	dwarf	main	dwarf
M_{DM} ($10^{11}\ M_\odot$)	7.7	1.1	7.7	1.1	7.7	1.1	7.7	1.1
M_s ($10^{10}\ M_\odot$)	9.0	0.4	8.0	0.4	8.0	0.05	9.0	0.4
$f_{b/d}$	0.126	0.157	0.139	0.157	0.139	n.a.	0.126	0.157
M_G ($10^9\ M_\odot$)	0.4	1.7	8.0	1.7	8.0	0	0.4	1.7
R_s (kpc)	6.0	4.5	6.0	4.5	6.0	4.5	6.0	4.5
R_d(kpc)	3.72	4.0	3.72	4.0	3.72	n.a.	3.72	4.0
h_d (kpc)	0.38	0.40	0.38	0.40	0.38	n.a.	0.38	0.40
r_b (kpc)	0.83	0.53	0.83	0.53	0.83	0.53	0.83	0.53

Table 3.5: Parameters defining the models of the two galaxies in the four runs. All parameters are defined as in Table (3.1). The ratio $f_{b/d}$ is relative to the stellar content in disk and bulge for each model. In the case of R3, where the dwarf has just a bulge and a halo and there is no disk at all, some parameters were not calculated for obvious reasons. They are substituted with "n.a." (not available). The second and the third column from *left* contain the corresponding values of the parameters for the main galaxy and for the dwarf galaxy in R1, respectively. Going *rightward* in the Table, the other couples of columns contain the same type of information for the main galaxy and the dwarf galaxy in R2, R3 and R4, respectively.

(3.5) I write the main parameters of the galactic models used in the four simulations.

Are the generated galactic disks stable against collapse before the star particles are converted into gas particles? The Toomre Q parameter (Toomre 1964) quantifies this stability. It is expressed as:

$$Q = \frac{\kappa \sigma_R}{3.36 G \Sigma}\,; \tag{3.21}$$

here κ is the epicyclic frequency and σ_R is the radial dispersion of the stellar motions and Σ is the stellar disk surface density. If Q is larger than 1, then the disk is stable against collapse. This parameter generally increases towards the centre and towards the outer edges of a disk. In the four simulations, the disk of the main galaxy has $Q \sim 1.025$ at $r = 2.5R_d$, with R_d the scale radius of the disk. In all simulations but R3 (where no disk was included in the dwarf galaxy), the disk of the dwarf galaxy has $Q \sim 5.70$ at $r = 2.5R_d$.

3.4.2 Initial conditions

The initial orbit of the dwarf galaxy in each simulation was chosen to study counter-rotation.

One of the main goals was to find counter-rotation via retrograde minor merger of two galaxies. So, I set the dwarf galaxy in R1 to be in retrograde motion with respect to the main galaxy. This means that the orbital angular momentum of the dwarf galaxy is

Run	D (kpc)	b (kpc)	v_{rel} (km s^{-1})	θ	ϕ	ψ	E_s (10^4 km^2 s^{-2})	$L_{z,s}$ (10^3 km s^{-1} kpc)
R1	200	10	200	-$\pi/2$	0	0	-0.141	-2.0
R2	200	10	200	-$\pi/2$	0	0	-0.141	-2.0
R3	200	10	200	-$\pi/2$	0	0	-0.128	-2.0
R4	200	10	200	+$\pi/2$	0	0	-0.141	+2.0

Table 3.6: Parameters describing the initial conditions for the orbit of the dwarf galaxy in each run. The first column reports the names of the four runs. The other parameters are defined as in Table (3.2), except for $L_{z,s}$, that is the z-component of the specific orbital angular momentum of the dwarf galaxy. For the sake of simplicity I wrote only the parameters that were changed between the outputs. In fact, for all simulations, the initial relative velocity is $\vec{v}_{rel} = 200$ km s^{-1}, the initial impact parameter is $b = 10$ kpc, $\phi = 0$, $\psi = 0$ and the initial orbital eccentricity is $e = 0.994$, so in all cases the dwarf galaxy is on an elliptical, quasi-parabolic orbit.

opposite to the spin of the main galaxy itself. Bearing in mind that there is more gas in the dwarf galaxy than in the main galaxy, this should in principle permit the formation of counter-rotation in the main galaxy.

In R2 I adopted the same initial orbital conditions as in R1. So, the difference between these two runs resides in the different quantities of gas in the main and in the dwarf galaxy. In particular, since more gas is present in the main galaxy, one should not expect counter-rotation in this case to form.

Again, in R3 the same initial parabolic retrograde orbit was chosen for the dwarf galaxy. Since in this case the dwarf galaxy is gas-free, this run helps studying whether or not the merger event itself triggers SF in the main galaxy, even if no gas is accreted.

Last, in R4 the dwarf galaxy is initially on a prograde parabolic orbit. Again, as in R2, in this case one should not expect counter-rotation to form, since the orbital angular momentum of the dwarf galaxy is parallel to the spin of the main galaxy.

In Table (3.6) I present the main orbital parameters used to generate the initial conditions of the four runs (Figure 3.12).

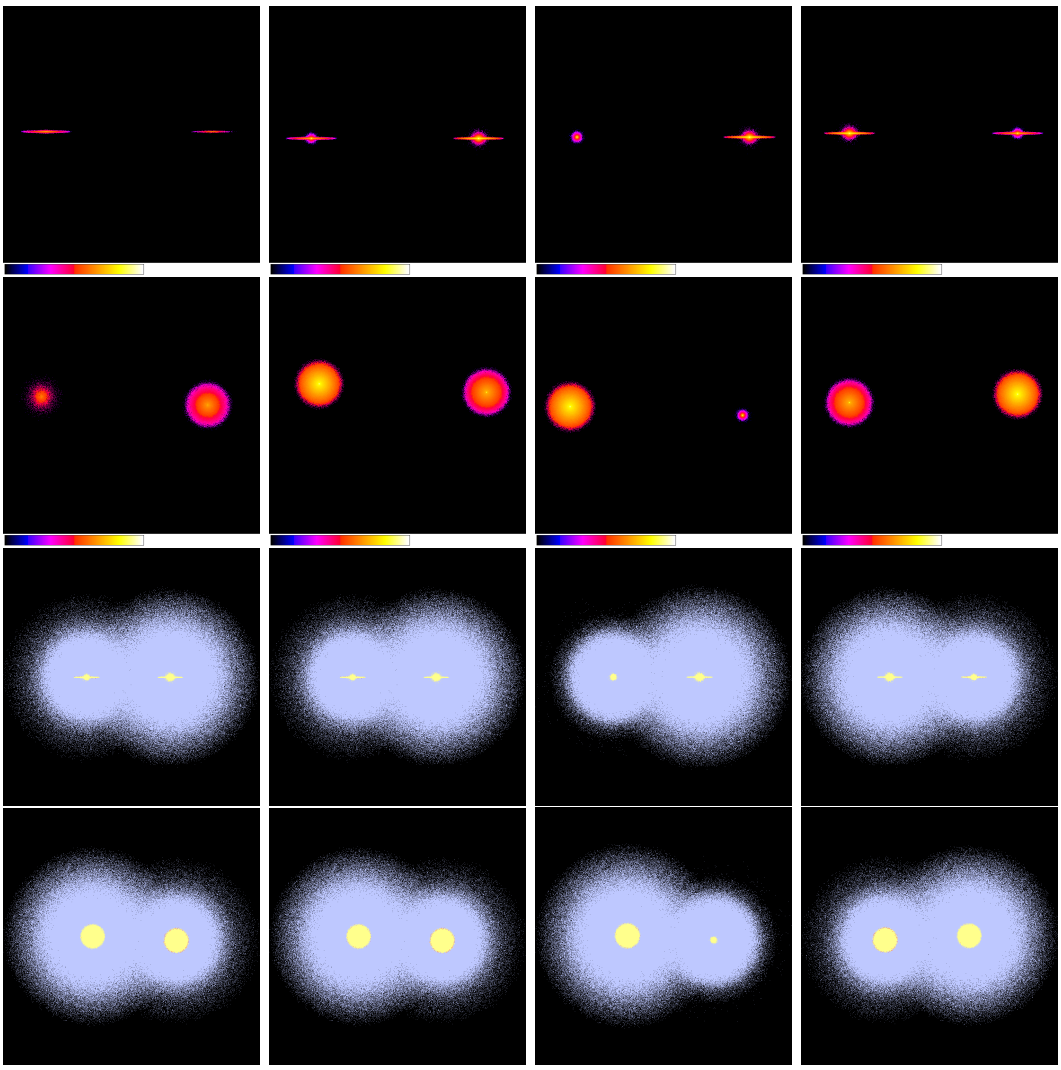

Figure 3.12: Snapshots of the initial epoch of the four simulations, from R1 (panels in the *left* column) to R4 (panels in the *right* columm). For each column, from *top* to *bottom*: y-projected and z-projected logarithmic contour plots of stellar densities (except for R1, for which I show the logarithmic contour plots of gas densities at time 0.01 Gyr from the beginning of the simulation), each measuring $\sim 300 \times 300$ kpc^2; y-view of all particles and z-view of all particles at time 0 Gyr, each measuring $\sim 600 \times 600$ kpc^2. Colors in the maps and colors in the views are defined as in the previous Figures.

Chapter 4

Results

In the end of Chapter 3 I discussed the galactic models and the initial conditions used to perform the four simulations. Now, I am going to discuss the results obtained from these simulations. For R1, R2 and R4 I will mainly focus on the rotation curve of the prograde and retrograde gas components around the nucleus of the main galaxy, and I am going to study the process of gas accretion. R3 will be used for a comparison with the other simulations in terms of triggering SF. For each simulation, I analyzed some outputs, up to 3.0 Gyr.

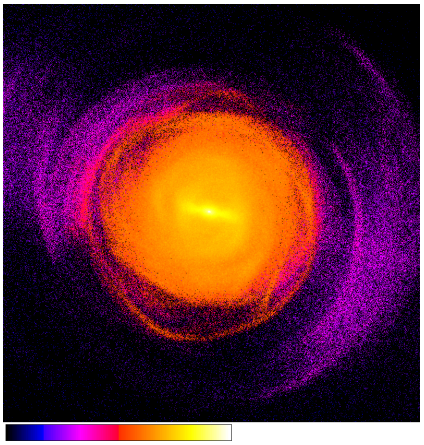

Figure 4.1: Snapshot of the z-projected logarithmic stellar density distribution around the nucleus of the main galaxy at 2.4 Gyr in R3. The color-code is the same as previously. The panel measures 100×100 kpc^2.

In each run, the main galaxy forms a bar roughly in the last Gyr (Figure 4.1). I will take the bar into consideration in the following Sections, in particular when discussing gas accretion in R1 and R4.

What is the evolution in time of the radial distance between the two galactic nuclei in each simulation (Figure 4.2)? In all cases the dwarf galaxy undergoes 3 periapsis

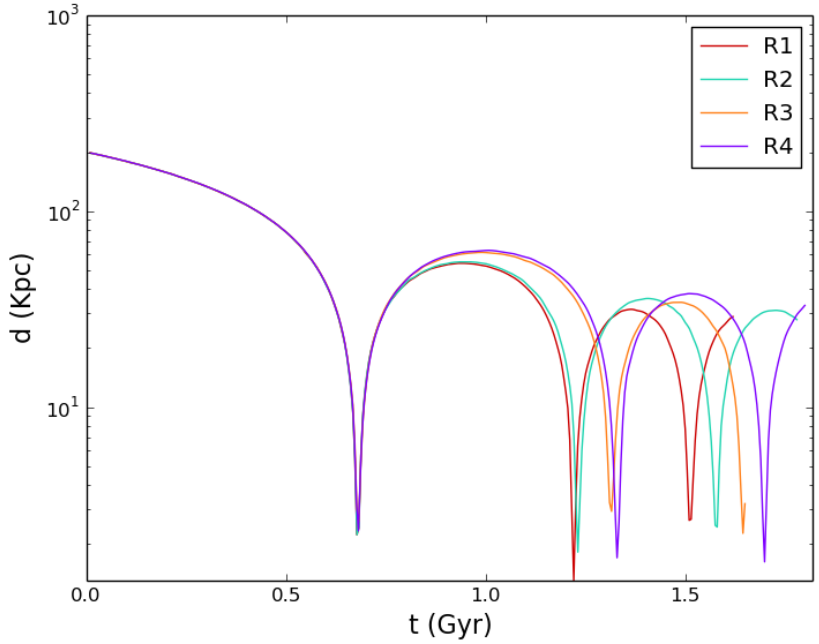

Figure 4.2: Distances between the mass centres of the two galaxies as functions of time in all four simulations.

passages. The first of them, that corresponds to the initial merger, happens at ~ 0.7 Gyr from the beginning of the simulation. After $1.6 \div 1.8$ Gyr from the beginning of each simulation, the stellar nucleus of the dwarf galaxy dissolves as the end result of tidal stripping with the main galaxy.

4.1 Rotation curves of gas

One of the most direct evidences of the presence of counter-rotation in galaxies is based on the analysis of the velocity curve of gas that is distributed around the nucleus of the host galaxy (for example by means of the kinematics of gas along the major axis of the host galaxy). How to obtain a rotation curve for gas in a simulation? The idea is to calculate, for each radial distance from the nucleus of the main galaxy, the corresponding average *tangential velocity* of gas particles falling in that radial bin.

In a cartesian frame of reference centered on the nucleus of the main galaxy, the radius vector describing the position of a particle is $\vec{r} = (x,y,z)$ and the corresponding velocity vector is $\vec{v} = (v_x,v_y,v_z)$. Given the axial symmetry of the disk of a galaxy, one can adopt cylindric coordinates to describe positions and velocities of particles. In this case, the position of the particle is $\vec{r} = (r,\phi,z)$, where r is the distance of the particle from O and ϕ is the azimuthal angle (the angle between the x-axis of the old cartesian coordinate

system and the direction of the vector linking O with the particle, counter-clockwise from the positive z direction). The corresponding, new coordinates (v_r,v_ϕ,v_z) of the velocity vector $\vec{v}$ can be written starting from the coordinates in the cartesian frame:

$$\begin{cases} v_r = v_x cos(\phi) + v_y sin(\phi)\,; \\ v_\phi = -v_x sin(\phi) + v_y cos(\phi), \end{cases} \tag{4.1}$$

being v_r the *radial velocity*, being v_ϕ the tangential velocity, and with v_z being defined as in the cartesian frame.

For the simulations R1, R2 and R4 I calculated the average velocity $\bar{v}_\phi(r)$ as a function of the distance r from the nucleus of the main galaxy. In particular, I truncated the selection of particles considering only particles with height less than 2 kpc from the equatorial plane of the main galaxy ($\sim$ 5 scale heights of the original main disk). In this way, I could concentrate on gas accretion on the host galactic disk. Consequently, I calculated the dispersion of the tangential velocities:

$$\sigma_\phi = \sqrt{\frac{\sum_{i=1}^{N} m_i}{[\sum_{i=1}^{N} m_i]^2 - \sum_{i=1}^{N} {m_i}^2} \sum_{i=1}^{N} m_i [v_{\phi,1} - \bar{v}_\phi(r)]^2}\,, \tag{4.2}$$

where m_i is the mass of the i-th particle in the radial bin of radius r and N is the number of particles in the given radial bin.

In Figures (4.3; 4.4; 4.5) I show the rotation curves and the tangential velocity dispersions of gas in the beginning and in the end of R1, R2 and R4, respectively.

In Figure (4.6) I show the mass distribution of gas in the r-v_ϕ space around the nucleus of the main galaxy in R1 and R4. In both simulations an amount of counter-rotating component forms, even in R4 where the dwarf galaxy was originally put on a prograde orbit.

In Figure (4.7) I show the gas mass distribution in the $r - v_\phi$ plane for R2. In this case no counter-rotation forms at all, except for the presence of a retrograde gas component that resides in the nucleus of the main galaxy. This is expected, since there is more gas mass in the main galaxy than in the dwarf galaxy, and therefore it is in agreement with the predictions by Lovelace & Chou (1996) mentioned before.

At the end of R1 and R4, the velocities of gas are very low, especially if they are compared with their corresponding dispersions (that, in turn, are not high). Why are the initially well-defined rotation curves of gas destroyed in the epochs following the merger in R1 and R4? One should expect energy conservation and, at least, a transfer of energy associated to ordered motions of gas into energy associated to the dispersion of these motions. If one compares the initial and final distribution of gas mass in the $r - v_\phi$ space around the nucleus of the main galaxy with that of the stellar mass (Figure 4.8), it is possible to observe that the original stellar rotation curve is not destroyed by the arrival of the external stellar component. Given this result, it is possible to conclude that gas behaves differently from stars during the process of accretion again because of the presence of viscous forces that act between the gaseous components. This ends

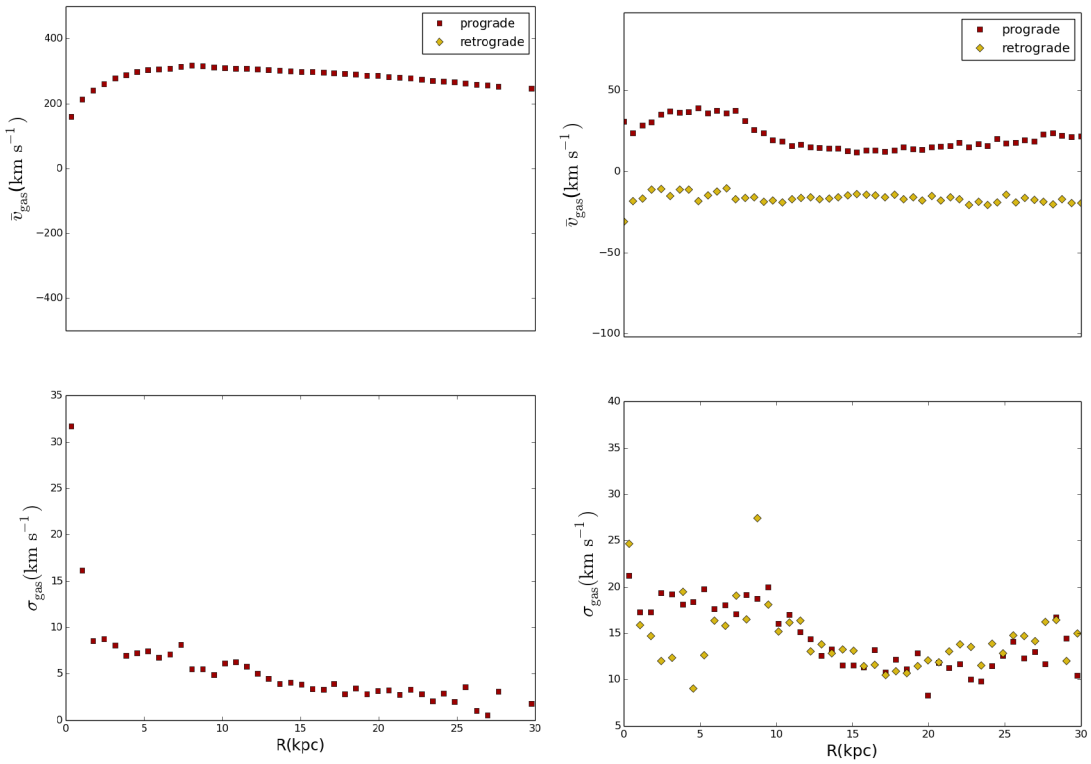

Figure 4.3: Average tangential velocity $\bar{v}_\phi$ (*top* plot for each panel) and tangential velocity dispersion σ_ϕ (*bottom* plot for each panel) of prograde and retrograde gas as functions of radial distance from nucleus in the main galaxy, for times 0.3 (*left* panel) and 3.0 (*right* panel) Gyr in R1.

up in the destruction of the previous kinematics. Furthermore, if we consider that gas cooling is active in all simulations, additional energy loss may be attributed to the cooling mechanism.

4.2 Properties of the counter-streaming gas

What is the spatial distribution of counter-rotating gas within 2 kpc height from the galactic plane of the main galaxy in R1, R2 and R4? In Figure (4.9) I show how gas is distributed around the nucleus of the main galaxy in R1, R2 and and R4, respectively, for the same outputs as before. In the case of R2, no gas accretes around the nucleus of the main galaxy.

In the case of R1, gas starts to accrete with continuity only after the second periapsis passage, so that for the first Gyr there is no net accretion of counter-streaming gas on the disk of the main galaxy. At 3.0 Gyr the final distribution of counter-streaming gas is not homogeneous through the disk of the main galaxy. Part of the retrograde gas component accretes on the nucleus of the main galaxy, while the remaining components accrete on a disk-like or ring-like structure. This structure may be still in a building phase, since

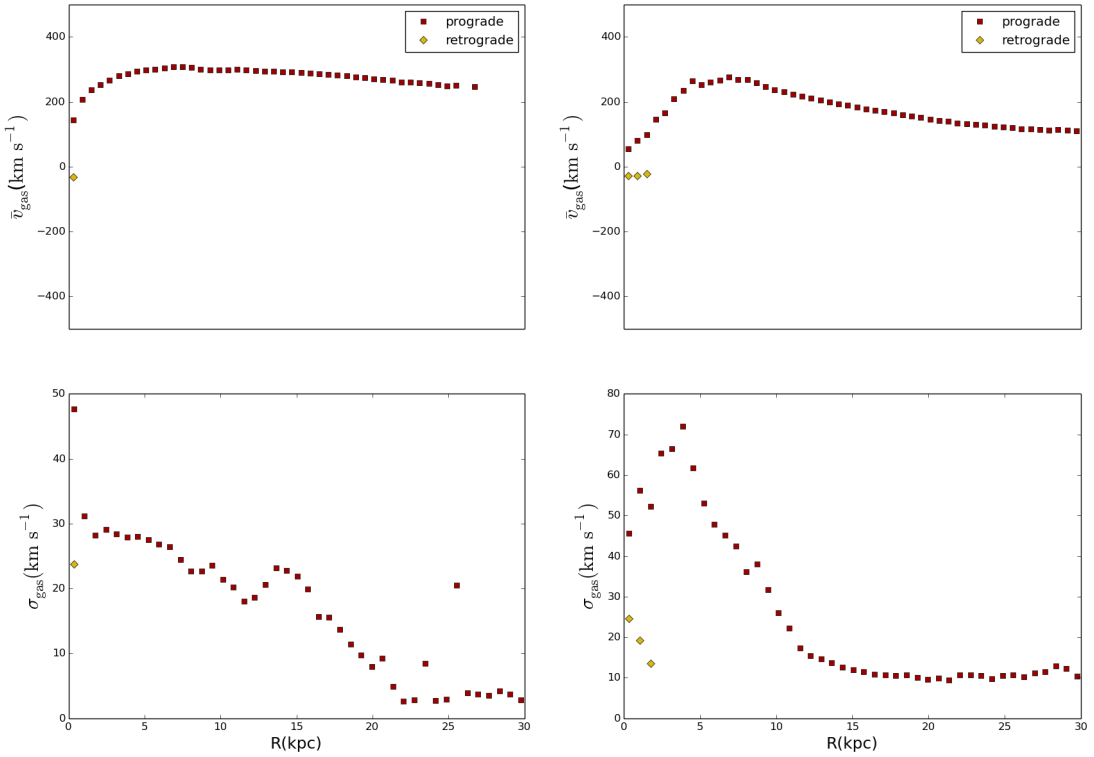

Figure 4.4: Average tangential velocity $\bar{v}_\phi$ (*top* plot for each panel) and tangential velocity dispersion σ_ϕ (*bottom* plot for each panel) of prograde and retrograde gas as functions of radial distance from nucleus in the main galaxy, for times 0.3 (*left* panel) and 3.0 (*right* panel) Gyr in R2.

no closed, symmetric shape seems to have formed. As already said, the bar in the main galaxy forms at ~ 2 Gyr. The development of this bar may drive this counter-streaming gas towards a resonance, so that a ring could form in the very end.

Interestingly, in R4 the quantity of retrograde gas mass that accretes on the main galactic disk at 3.0 Gyr is not irrelevant with respect to the quantity of gas that accretes in R1 around the nucleus of the main galaxy at the same epoch. So, counter-streaming gas can successfully accrete on the disk of the main galaxy thanks to the prograde minor merger. The reason for this result will be discussed in Chapter 5, by comparing it with the results obtained from the prograde minor merger simulated in MRM15.

What is the distribution of the radial and vertical motions of retrograde gas at 3.0 Gyr in R1 and in R4 (Figures 4.10; 4.11)? In R1, retrograde gas is not much radially heated. The average radial velocities are mostly positive (gas escaping from galactic nucleus) and $< 20 \div 30$ km s^{-1}. Some regions show higher radial velocities, of the order of 40 km s^{-1} in the very inner regions, and of the order of 80 km s^{-1} in the outer regions, but they are not dominant. The corresponding dispersions are not large, and only show some peaks in correspondence with the nucleus of the main galaxy (~ 40 km s^{-1}). In R4 the situation is similar. Even, the hottest regions do not reach more than ~ 50 km

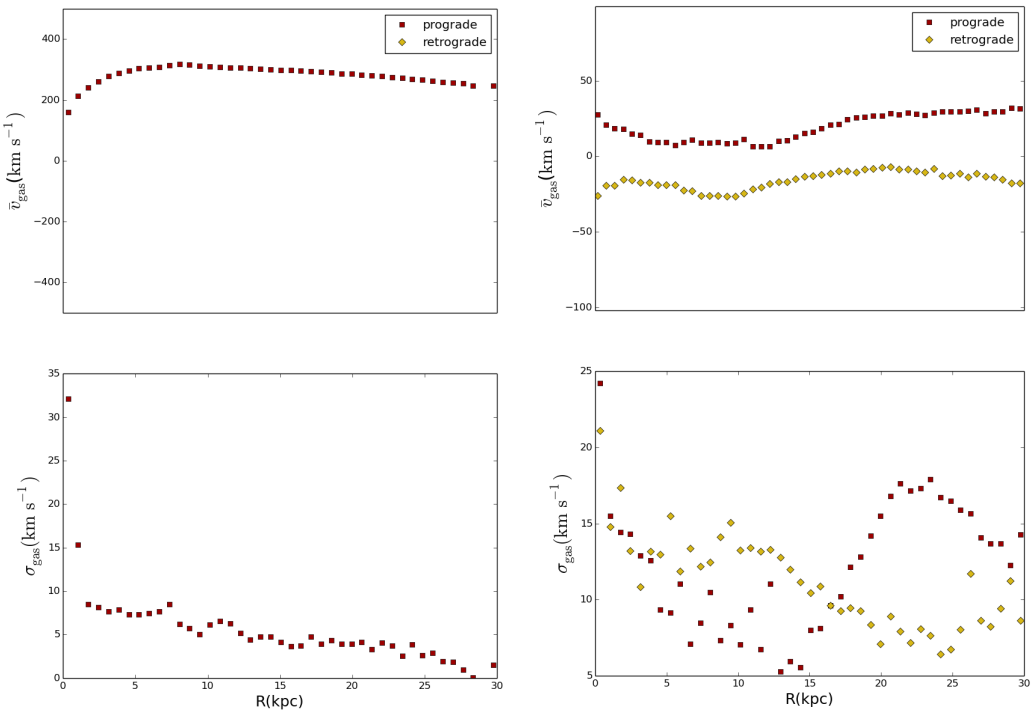

Figure 4.5: Average tangential velocity $\bar{v}_\phi$ (*top* plot for each panel) and tangential velocity dispersion σ_ϕ (*bottom* plot for each panel) of prograde and retrograde gas as functions of radial distance from nucleus in the main galaxy, for times 0.3 (*left* panel) and 3.0 (*right* panel) Gyr in R4.

s^{-1} far from the nucleus. Their dispersion peaks near the nucleus, reaching a maximum of $50 \div 60$ km s^{-1}.

As to the vertical heating of counter-streaming gas, the average z-velocities in R1 are mostly < 30 km s^{-1}, with some minor peaks in the inner region of the ring-like structure and some others far from nucleus, and with more dispersion in the nuclear region of the galaxy ($50 \div 60$ km s^{-1}). In R4 these values are again small, with many regions within the accreted structure reaching no more than ~ 10 km s^{-1} on average, except for an elongated structure. Again, this gas is not strongly dispersed in the vertical direction, and peaks at the centre of the main galaxy.

If we compare again this result with Figure (4.8), we find once more that, in contrast to the original stellar kinematics, the original gas kinematics in the main galaxy has been destroyed by the impact with retrograde gas in R1 and in R4.

In contrast, in R2 the final gas kinematics is nearly the same as in the beginning, because the prograde gas mass is much more than the retrograde gas mass.

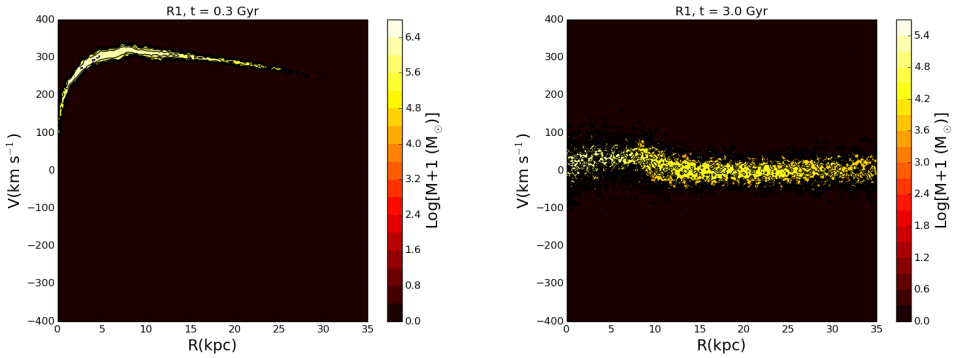

Logarithmic color-coded contour plots of the distribution of gas in r-v_ϕ space in the main galaxy, for times 0.3 (*left* panel) and 3.0 (*right* panel) Gyr in R1.

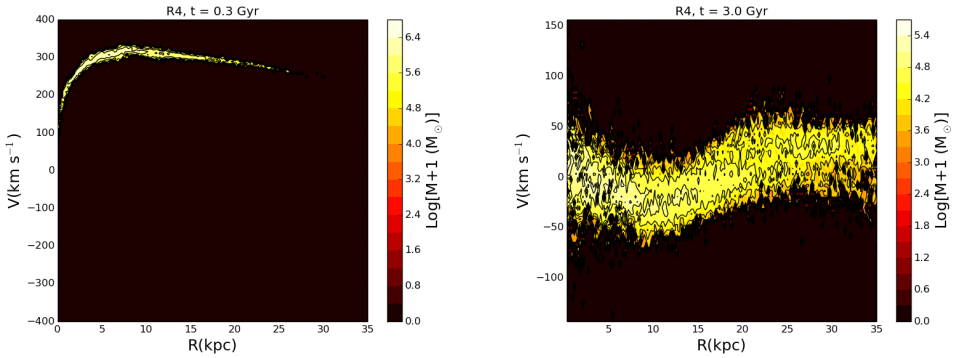

Logarithmic color-coded contour plots of the distribution of gas in r-v_ϕ space in the main galaxy, for times 0.3 (*left* panel) and 3.0 (*right* panel) Gyr in R4.

Figure 4.6: Contour plots of the rotation curve of gas for R1 and R4

4.3 Mass accretion history

Now, I compare the accretion history of counter-rotating gas in R1 with that in R4. For different times going from 0.3 to 3.0 Gyr, I calculated the fraction of counter-rotating gas mass as a function of radius R around the nucleus of the main galaxy in R1 and in R4 (Figure 4.12). I recall that this is not a cumulative mass profile from $r = 0$ to $r = R$; instead, it shows how much retrograde gas is contained in each radial bin centered around a radius R. In both plots, since there is no counter-streaming gas mass at 0.3 Gyr, the corresponding profile is plain. In R1, the final distribution of retrograde gas gives most of its contribution on a radial interval between 15 and 25 kpc from nucleus, reaching peaks of mass fraction equal to 0.6.

In R4, the accretion seems to be more relevant, reaching roughly the totality of gas

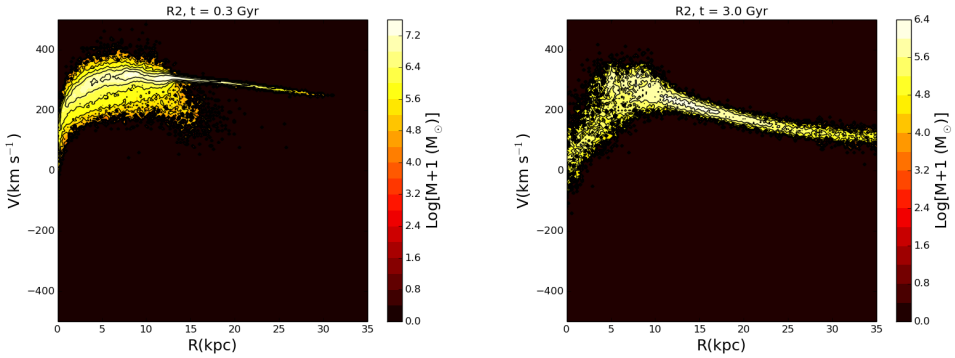

Figure 4.7: Logarithmic color-coded contour plots of the distribution of gas in r-v_ϕ space in the main galaxy, for times 0.3 (*left* panel) and 3.0 (*right* panel) Gyr in R2.

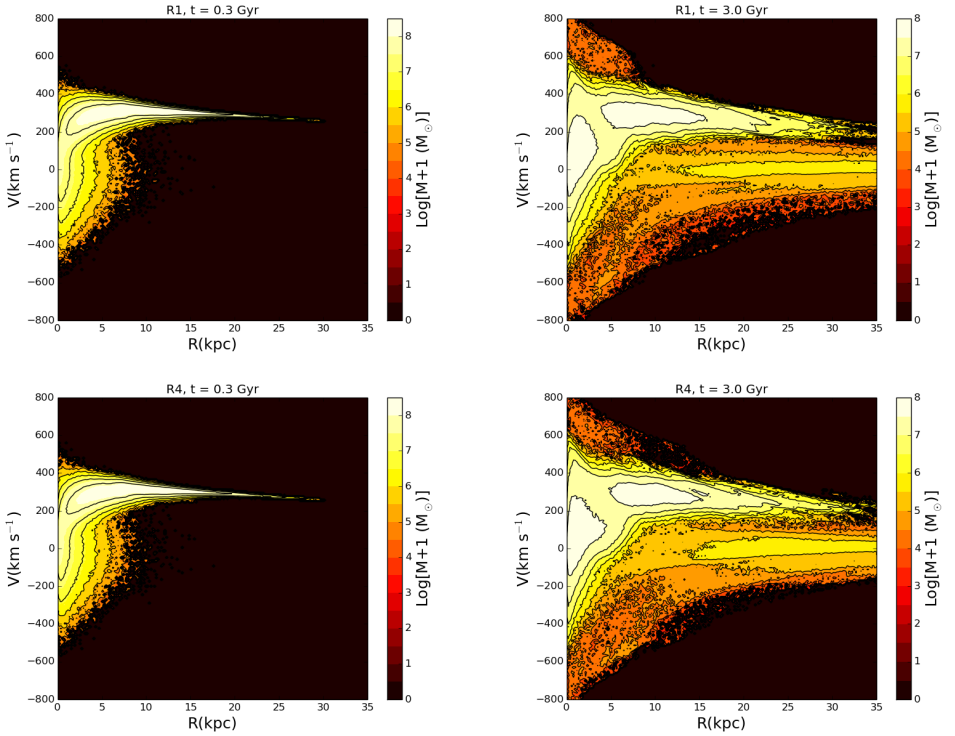

Figure 4.8: *Top* panels: logarithmic color-coded contour plot of the stellar mass distribution in the $r - v_\phi$ space around the nucleus of the main galaxy for times 0.3 Gyr (*left*) and 3.0 Gyr (*right*) in R1. *Bottom* panels: the same color-coded contour plots for R4.

mass in the inner 15 kpc at 2.7 Gyr from the beginning of the simulation, and finally representing a fraction $f \sim 0.9$ at 3.0 Gyr. In the outer regions, the prograde gas seems to dominate.

Considering the last outputs in R1 and R4, the fact that in both simulations there are

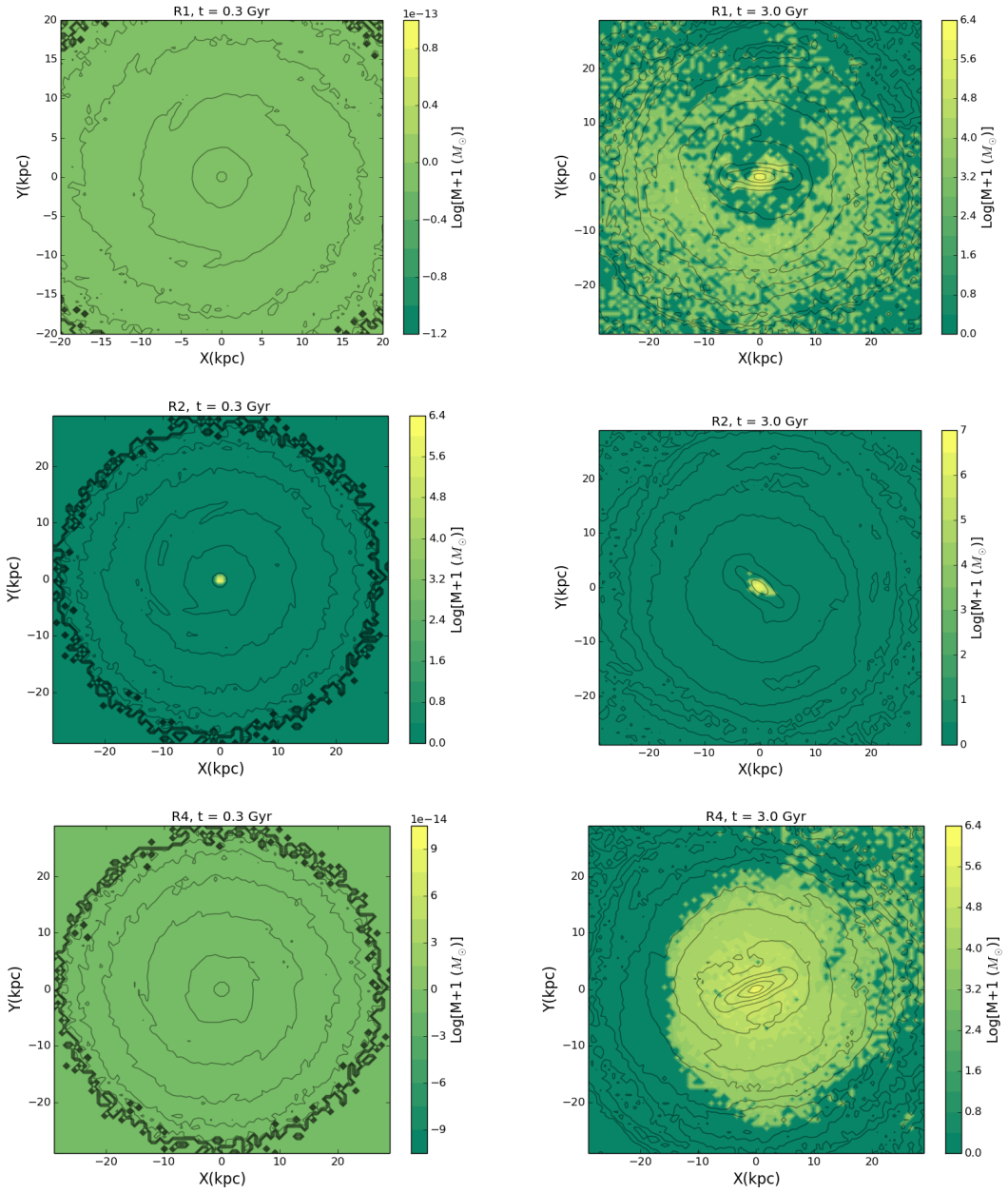

Figure 4.9: z-projected logarithmic color-coded contour plots of the distribution of gas mass around the nucleus of the main galaxy for times 0.3 Gyr (*left* panels) and 3.0 Gyr (*right* panel) in R1 (*top* panels), R2 (*central* panels) and R4 (*bottom* panels).

still fractions of both prograde and retrograde gas coexisting at the same radial distance is not surprising. In fact, when both components have the same radial distance, mostly they occupy different regions in the disk. Furthermore, when they overlap, their masses

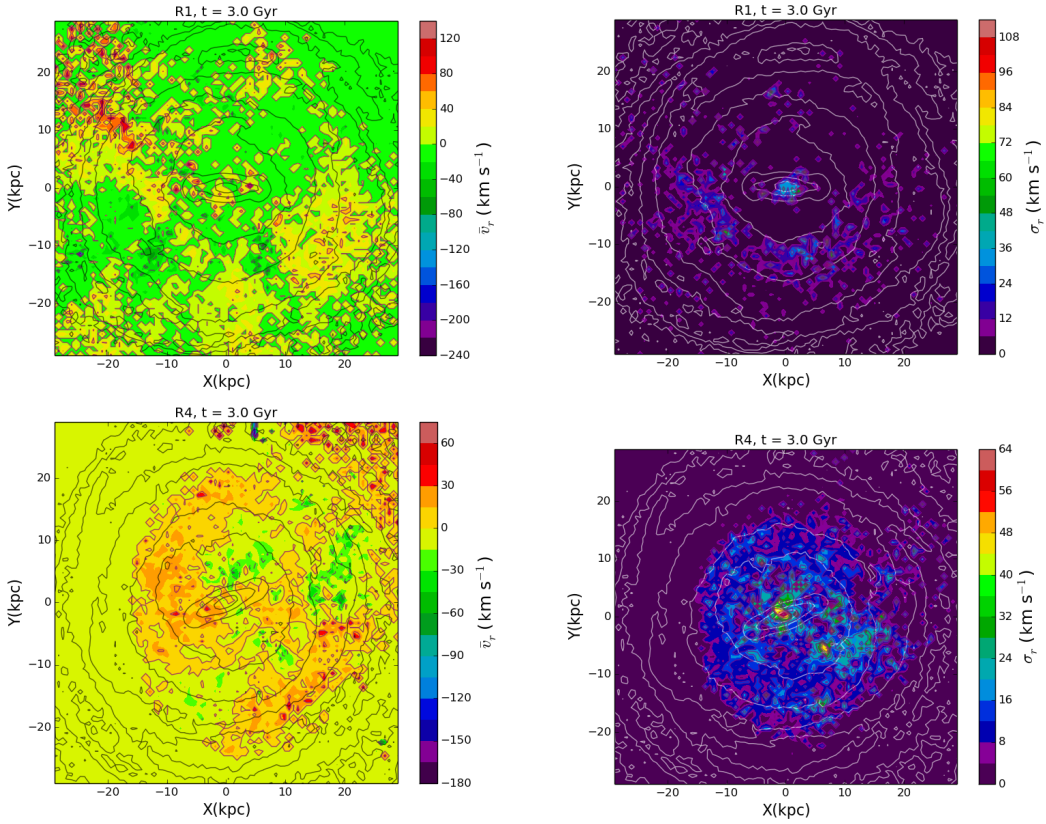

Figure 4.10: z-projected color-coded contour plots of the distribution of average values of radial motions of counter-rotating gas (*left* panel) and of their dispersions (*right* panels) plotted against single-color empty contours of the stellar density distribution around the nucleus of the main galaxy at 3.0 Gyr in R1 (*top* panels) and in R4 (*bottom* panels).

are not of the same order of magnitude, so that much smaller quantities of one component co-exist with larger masses of the other (Figure 4.13). In any case, the mechanism of accretion seems to be still in progress and some other fractions of gas mass could possibly accrete from the environment after 3.0 Gyr, since gas is diffused both above and below the disk of the main galaxy. This dispersion is in part a consequence of gas fountains in the original dwarf galaxy (Figure 4.14; see also Mac Low & Ferrara 1999). It is probable that after more than 3.0 Gyr the prograde gas mass in both R1 and R4 will be confined in the inner region (R1) or in the very outer region (R4) of the main galactic disk.

On the other side, the fact that no counter-rotation has been found after 3.0 Gyr from the beginning of R2 is a good confirmation that the accreted retrograde gas mass must overcome the pre-existing, prograde gas mass in order to successfully build a counter-rotating structure in the disk of the main galaxy.

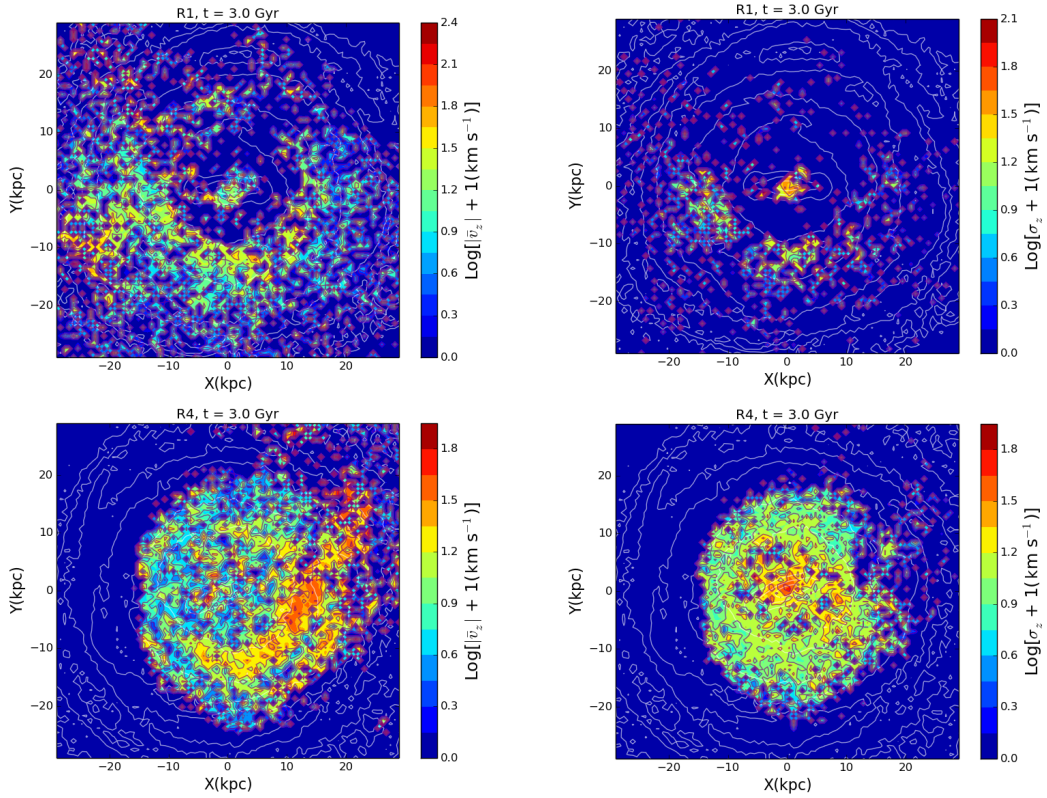

Figure 4.11: z-projected color-coded logarithmic contour plots of the distribution of average values of vertical motions of counter-rotating gas (*left* panel) and of their dispersions (*right* panels) plotted against single-color empty contours of the stellar density distribution around the nucleus of the main galaxy at 3.0 Gyr in R1 (*top* panels) and in R4 (*bottom* panels).

4.4 Star Formation Rate and cumulative Star Formation

I calculated SFR and cumulative SF in all simulations (Figure 4.15). I used all the spatial volume in each simulation, in order to avoid loss of information about total SF.

SFR is similar in R1 and R4. In R2 and in R3 it is higher, reaching peaks of $5 \div 6 M_{\odot}$ yr $^{-1}$ at 0.3 Gyr. In contrast, in R1 and R4 the SFR peaks are modest, reaching no more than $\sim 0.5 M_{\odot}$ yr $^{-1}$ in general. In R1 and R4, where more gas is in the dwarf galaxy and less gas is in the main galaxy, the merger contributes to trigger SF. In fact, in these simulations, between 0.6 and 0.9 Gyr (around the epoch of the merger), cumulative SF (SF$_{cum}$) has a relative increase:

$$\mathrm{SF}_{0.9-0.6}/\mathrm{SF}_{cum,0.6} \sim 1\,. \tag{4.3}$$

This is twice its relative increase from 0.3 to 0.6 Gyr:

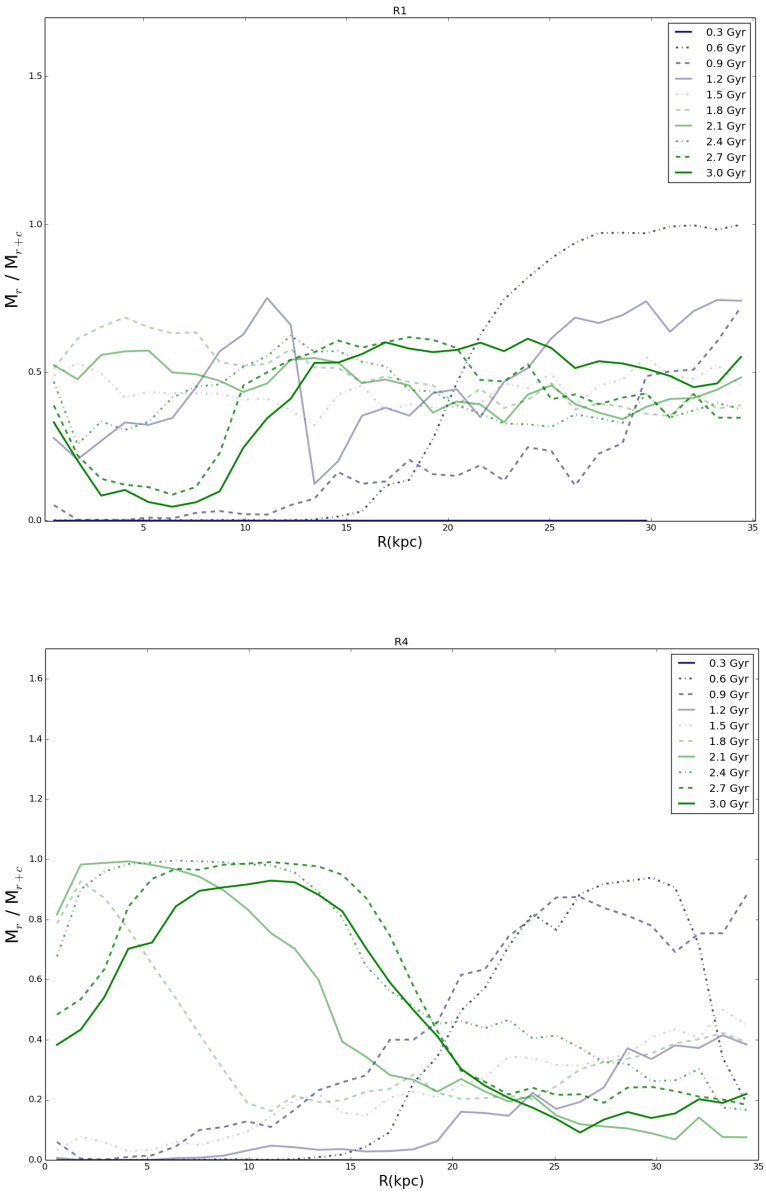

Figure 4.12: Counter-streaming gas mass accretion history around the nucleus of the main galaxy for R1 (*top* panel) and for R4 (*bottom panel*). M_r is the retrograde gas mass, M_{r+c} is the sum of the co-rotating and retrograde gas masses, i.e. it is the total gas mass.

$$\mathrm{SF}_{0.6-0.3}/\mathrm{SF}_{cum,0.3} \sim 0.04\,. \tag{4.4}$$

In contrast, in R2 and in R3, since there is much more gas mass than in the other

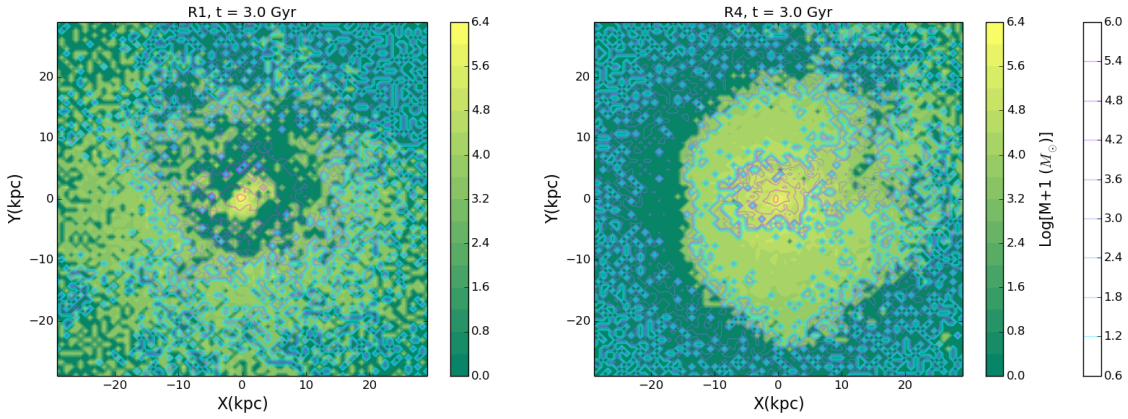

Figure 4.13: z-projected logarithmic contour plots of the counter-streaming gas mass (filled map) and of the prograde gas mass (empty contours) around the nucleus of the main galaxy at time 3.0 Gyr in R1 (*left* panel) and in R4 (*right* panel).

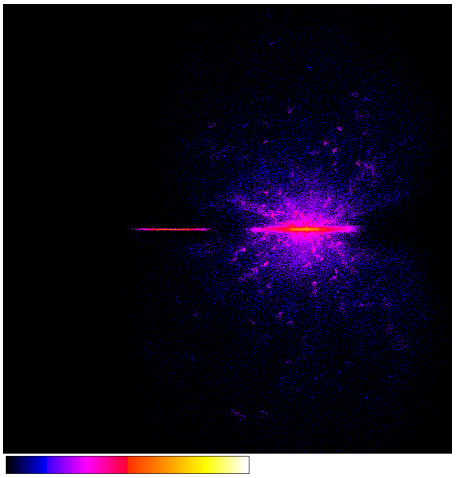

Figure 4.14: Example of gas fountains in R4 at 0.5 Gyr. The dwarf galaxy is on the right and it shows streams of gas escaping from the disk. However, most of the gas mass is still on the disk. This is a y-projected logarithmic contour plot of the gas density distribution. The panel measures 260×260 kpc^2. The color code is the same as in the previous panels.

simulations (the main galaxy is way richer in gas), the merger does not significantly contribute to SF. In particular, in this case the cumulative SF has an increase:

$$\mathrm{SF}_{0.9-0.6}/\mathrm{SF}_{cum,0.6} \sim 0.3\,, \tag{4.5}$$

that is less than its relative increase from 0.3 to 0.6 Gyr:

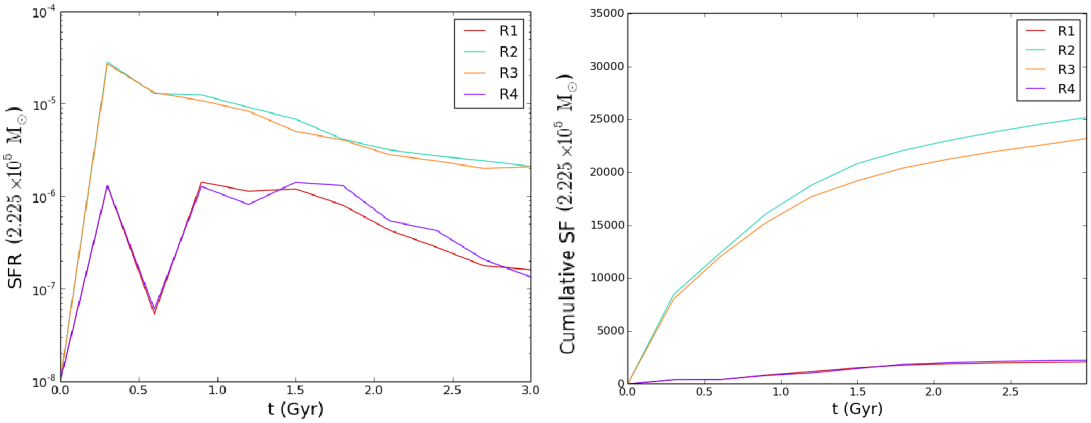

Figure 4.15: SFR (*left-hand* panel) and cumulative SF (*right-hand* panel) in the four simulations as functions of time, from 0 Gyr to 3.0 Gyr and with a time interval of 0.3 Gyr. The values of SFR at 0 Gyr were put equal to 10^{-8} (in units of $2.225 \times 10^5 M_\odot$) by default.

$$\mathrm{SF}_{0.6-0.3}/\mathrm{SF}_{cum,0.3} \sim 0.4 \div 0.5\,. \tag{4.6}$$

The fact is that in R2 and R3 the mechanism is already triggered by the larger amounts of gas that reside in the disk of the main galaxy. So, here the minor merger does not change too much SF.

4.5 Gas temperatures

Last, I checked the distribution of gas mass in temperature and density for some outputs of the simulations. In Chapter 2 I discussed the cooling problem and I showed a direct, simple solution to the problem, that is to put a constraint on gas cooling in the parameter file before launching the simulations.

Differently from the test run in ChaNGa and in Gasoline, these constraints avoided gas cooling below 10^3 K in all four simulations. As an example, I show this for R1 in Figure (4.16), by comparing the initial and the final distributions of gas in the ρ-T plane. No gas cools below 10^3 K in the end. Even if I put the maximum limit temperature at 10^7 K, there are still some particles that have higher temperatures than 10^7 K. These particles do not represent a relevant fraction of the total gas mass. In any case, this indicates that the regulation of gas temperatures is not perfect and that while running a simulation some gas particles may escape the limits imposed to them in terms of thermal properties.

At 3.0 Gyr, the hottest ($10^6 \div 10^7$ K) and densest ($\sim$ 1 atom cm^{-3}) regions in the ρ-T plane correspond roughly to the inner region around the nucleus of the main galaxy. However, there are other hot regions ($\sim 10^6$ K) that correspond to a larger gas distribution around the main galaxy.

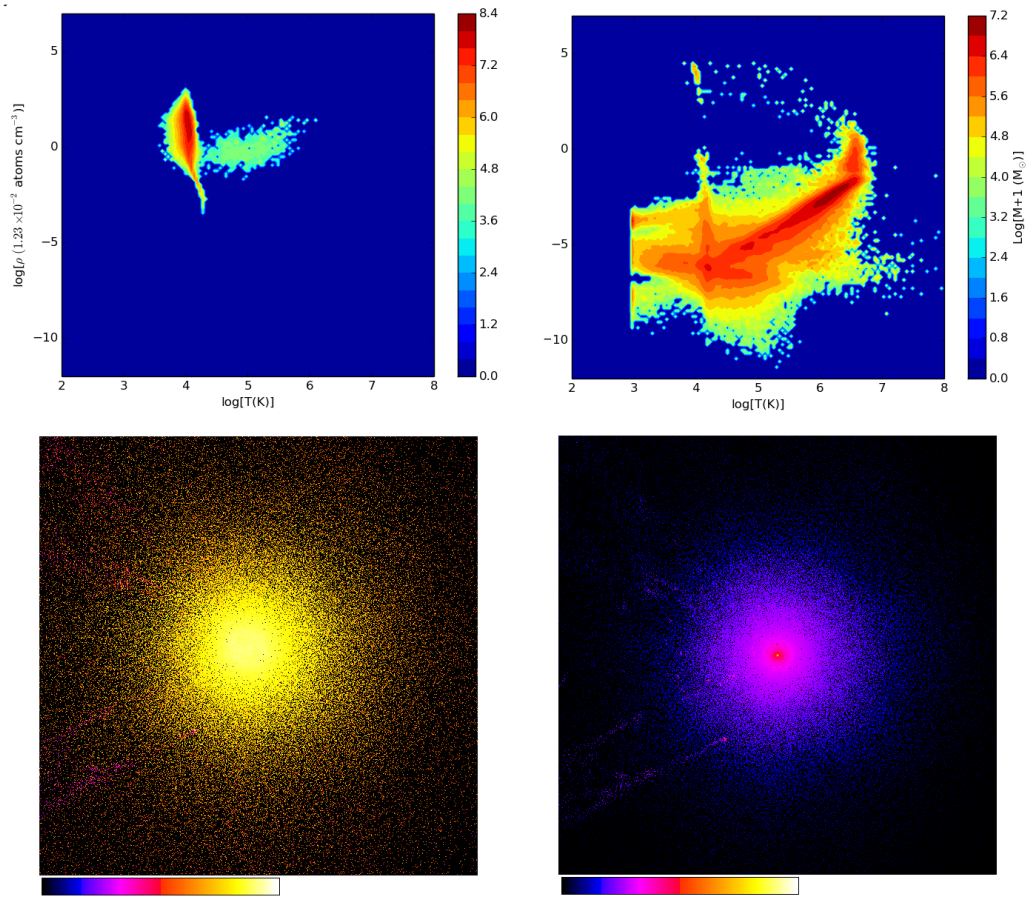

Figure 4.16: *Top* panels: logarithmic contour plots of the distribution of gas mass in the ρ-T plane at 0.01 Gyr (*left* panel) and at 3.0 Gyr (*right* panel) for R1. *Bottom* panels: z-projected logarithmic contour plots of the distribution of gas temperatures (*left* panel) and densities (*right* panel) at 3.0 Gyr. The color code is the same as previously. The bottom panels measure 250×250 kpc^2.

Chapter 5

Conclusions and comparison with literature

5.1 Summary and conclusions

I performed four minor merger simulations (R1, R2, R3 and R4) to study counter-rotation and gas accretion in a disk galaxy. I used the N-body SPH code ChaNGa. In the first three simulations the dwarf galaxy was initially put on a retrograde parabolic orbit, while in R4 it was initially put on a prograde parabolic orbit. I varied the quantities of gas in both galaxies. In R1 and R4 the gas mass in the dwarf galaxy is ~ 4 times the gas mass in the main galaxy, while in R2 it is ~ 0.25 times the gas mass in the main galaxy. In R3 I used a dwarf spheroidal with no gas. In each run, the total simulated time was 3 Gyr.

I calculated the rotation curve of gas around the nucleus of the main galaxy in R1, R2 and R4. Counter-rotation is found in R1 and in R4, where the previous rotation curve of gas in the main galaxy is destroyed by the impact with the dwarf galaxy, and radial and vertical velocities of retrograde gas are not high, nor highly dispersed. This is due to shocks between gas in the main galaxy and gas in the dwarf galaxy. These shocks trigger stronger gas cooling, so that most of the energy associated to the original circular motions is dissipated after the merger. In R2, in contrast, the prograde gas mass is more than the retrograde gas mass and it survives the impact. In fact, its rotation curve is not destroyed.

I analyzed the properties of counter-rotating gas mass in the disk of the main galaxy and I have studied the retrograde gas accretion history. In R1 retrograde gas successfully accretes on the disk of the main galaxy. In R2, no counter-streaming structure can successfully accrete. In R4, a non-negligible fraction of counter-rotating gas mass forms in the inner regions of the main galaxy, representing the 80% of the whole gas mass there. In Section 5.2 I will discuss the counter-rotation obtained in R4. In contrast, at the end of R1, the are more modest levels of counter-rotating gas mass in the main galaxy, though reaching most of the gas fraction ($\sim 60\%$) between 15 and 25 kpc distance from nucleus, in a ring-like or disk-like structure. This structure may be driven by a resonance with the

bar in the main galaxy (maybe a outer Lindblad resonance, since gas is counter-rotating). Thus, it is probable that it will form a ring after more than 3 Gyr. In R4 the bar has not contributed to the formation of the retrograde gas structure yet. Maybe, it is necessary to wait for more than 3 Gyr before a ring can form.

I compared SF in all simulations. In R1 and R4, where there is less gas than in R2 and R3, SF levels are generally lower and the minor merger can contribute more to SF. In R2 and R3, in contrast, the minor merger can give only a small contribution to SF because of the larger gas reservoir in the main galaxy.

I checked the distribution of gas in density and temperature as a control test for gas cooling at low densities. Gas does not cool below 10^3 K. This means that the constraints put on gas cooling prior to running the simulations were successful.

5.2 Comparison with literature

5.2.1 Counter-rotation via prograde minor merger

In MRM15 only prograde gas accreted on the main galaxy via the prograde minor merger. In R4, after the prograde merger, there is accretion of retrograde gas. This could be

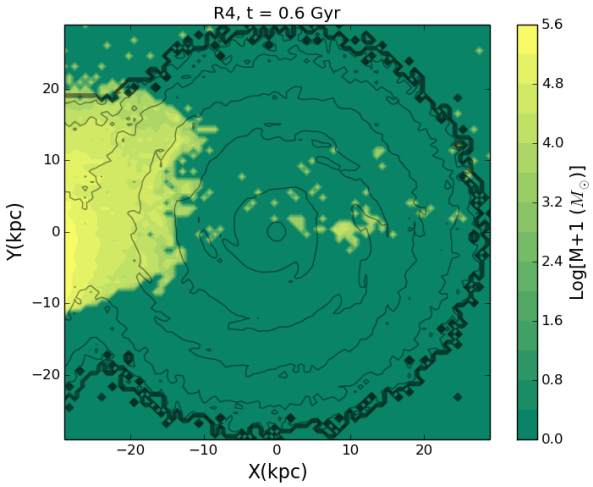

Figure 5.1: z-projected logarithmic contour plot of the counter-streaming gas mass (filled map) and of the stellar mass (black contours) around the nucleus of the main galaxy at time 0.6 Gyr in R4. There are some amounts of gas that have positive values of y position and negative tangential velocities with respect to the nucleus of the main galaxy, even if the dwarf galaxy was originally put on a prograde orbit.

explained considering two differences between the minor merger simulated in R4 and the one simulated in MRM15. First, the dwarf galaxy in R4 has a lager scale radius ($\sim$ 4 kpc) than in MRM15 ($\sim$ 3 kpc). Thus, the gaseous disk in the dwarf galaxy is more expanded and reaches the regions in the host disk opposite to the ones from

which the nucleus of the dwarf is coming (Figure 5.1). Second, in R4 the dwarf galaxy is initially on an elliptical/parabolic orbit ($e \sim 0.99$), while in MRM15 the initial orbit was hyperbolic/parabolic ($e \sim 1.003$). The combination of the different scale radius and orbital eccentricity with respect to MRM15 may permit retrograde gas accretion even via prograde merger.

5.2.2 SF: comparison with previous results

In R1 and in R4, both minor mergers contribute substantially to SF processes, since the main galaxy is less rich in gas. In R2 and in R3, in contrast, more gas reservoir is initially available in the main galaxy and the minor merger can increase SF only by a small fraction. In MRM15, since no gas was included in the main galaxy, the minor mergers had a good impact in terms of triggering SF in the host galaxy, reaching peaks of $\sim 5 \times 10^{-3} M_{\odot}$ yr^{-1}. This confirms that in early-type disk galaxies the introduction of external gas reservoirs (for instance, through a minor merger) can substantially contribute to SF, while in late-type disk galaxies the mechanism is less relevant because of larger, pre-existing gas reservoirs. This is in agreement with what Sancisi et al. (2008) and Di Teodoro & Fraternali (2014) found about SF in S galaxies (see Chapter 1).

One point must be stressed: in MRM15 the total gas mass is only $1.38 \times 10^8\, M_{\odot}$ and initially resides all in the dwarf galaxy. Among the four simulations run in this thesis, R1 and R4 are the most similar ones to MRM15, because of the lower levels of gas mass in the main galaxy. Thus, considering that in R1 and R4 the total gas mass is $M_g \sim 2.1 \times 10^9\ M_{\odot}$, considering the Schmidt law (with $n = 1.5$ as suggested by Kennicutt 1998) and normalizing M_g to the value obtained in MRM15, one obtains, at the epoch of the merger and as a rough estimate, a SFR$_n$ normalized to the masses in MRM15 equal to:

$$\mathrm{SFR}_{R1,n} \propto \mathrm{SFR}_{R1} \times \left(\frac{1.38 \times 10^8}{2.1 \times 10^9}\right)^{1.5} = 0.31 \times 0.66^{1.5} \sim 5.2 \times 10^{-3}\, M_{\odot}\,\mathrm{yr}^{-1}\,; \quad (5.1)$$

$$\mathrm{SFR}_{R4,n} \propto \mathrm{SFR}_{R4} \times \left(\frac{1.38 \times 10^8}{2.1 \times 10^9}\right)^{1.5} = 0.28 \times 0.66^{1.5} \sim 4.7 \times 10^{-3}\, M_{\odot}\,\mathrm{yr}^{-1}\,. \quad (5.2)$$

Also, taking into account that at the moment of the merger SF in ChaNGa is roughly f times higher than in Gasoline, with $f \sim 2 \div 3$ (see Chapter 3), and dividing SFR$_{R1,n}$ and SFR$_{R4,n}$ for f, the obtained values are of the same order of magnitude as the peak levels of SFR in MRM15.

5.3 Possible developments

Considering the kinematic and dynamical scenario obtained in the disk of the main galaxy at the end of R1 and R4, the natural prosecution to this work is to study the evolution of gas accretion on the main galaxy for more than 3 Gyr. The idea is to check whether or not the counter-rotating gas structure formed in the main galaxy in R1 can finally

evolve into a well-defined structure after more than 3 Gyr. At the same time one can obtain a final answer to the problem of the final distribution of retrograde gas in R4. In addition, after more than 3 Gyr it is expected that the accreted counter-streaming gas can generate a counter-streaming stellar structure. This would permit to study the long-term SF in galaxies that undergo minor mergers and to study the kinematics of the younger, retrograde stellar population.

Furthermore, *mock observations* (i.e. simulated observations) of gas kinematics along the projected major axis of the main galaxy could permit to match the results of R1 and R4 with real observations of gas counter-rotation in disk galaxies. To do this, it is again necessary to wait for more than 3 Gyr before a clear kinematic scenario can emerge around the nucleus of the main galaxy in R1 and R4.

The results obtained in this thesis could be compared with simulations of minor mergers in which the dwarf galaxy is initially put on different types of orbits, not only parabolic. Hopefully, this would help understand the efficiency of minor mergers in building counter-streaming structures with more general, initial orbital conditions for the dwarf galaxy.

Finally, to which extent do minor mergers compete with other processes (such as filamentary gas accretion on disk galaxies or major mergers) in forming counter-rotation? Only on a cosmological scale, the comparison of the different formation mechanisms permits to understand which of them could have dominated the past gas accretion history on disk galaxies, at different redshifts z. This could also extend at high z the results obtained in previous literature on minor mergers, such as in Bertone & Conselice (2009). In fact, they predicted a frequency of minor mergers $f \sim 10\% - 30\%$ at $z = 0$.

Acknowledgements

I thank Prof. A. Pizzella and Prof. M. Mapelli for their useful comments and for all the help they gave me to better understand the many aspects of the topics related to this thesis. Also, I thank the referee Prof. G. Galletta for additional comments and Prof. E. M. Corsini and Dott. M. Spera for some further suggestions and support.

To analyze the outputs of the simulations, I made use of the software `TIPSY`, by N. Katz and T. R. Quinn. It is available at `http://www-hpcc.astro.washington.edu/tools/tipsy/tipsy.html`. All the simulations were performed with the supercomputer Galileo, at CINECA. I made use of part of the 198000 CPU hours granted to M. Mapelli and R. Rampazzo for a class C project intended to perform numerical simulations of minor mergers.

Bibliography

Alladin, S. M. 1965, ApJ, 141, 768

Balcells, M., & González, A. C. 1998, ApJ, 505, L109

Balsara, D. S. 1995, JCoPh, 121, 357

Barnes, J., & Hut, P. 1986, Nature, 324, 446

Bate, M. R., Bonnell, I. A., & Price, N. M. 1995, MNRAS, 277, 362

Bentley, J. L. 1979, IEEE Transactions on Software Engineering SE-5 (Washington, DC: IEEE Computer Society), 333

Bertola, F., Buson, L. M., & Zeilinger, W. W. 1992, ApJ, 401, L79

Bertola, F., Cinzano, P., Corsini, E. M., et al. 1996, ApJ, 458, L67

Bertola, F., & Corsini, E. M. 1999, IAU Symp. 186, Galaxy Interactions at Low and High Redshift, ed. J. E. Barnes, & D. B. Sanders (Dordrecht: Kuwler Academic Publisher), 145

Bertone, S., & Conselice, Ch. J. 2009, MNRAS, 396, 2345

Bettoni, D. 1984, Msngr, 37, 17

Bettoni, D. 1989, AJ, 97, 79

Bettoni, D., & Galletta, G. 1997, A&AS, 124, 61

Bettoni, D., Galletta, G., & Prada, F. 2001, A&A, 374, 83

Binney, J., & Tremaine, S. 2008, Galactic Dynamics (Princeton, NJ: PUP)

Bottema, R. 1993, A&A, 275, 16

Braun, R., Walterbos, R. A. M., & Kennicutt, R. C. 1992, Nature, 360, 442

Braun, R., Walterbos, R. A. M., Kennicutt, R. C., & Tacconi, L. 1994, ApJ, 420, 558

Caldwell, N., Kirshner, R. P., & Richstone, D. O. 1986, ApJ, 305, 136

Ciri, R., Bettoni, D., & Galletta, G. 1995, Nature, 375, 661

Coccato, L., Morelli, L., Corsini, E. M., et al. 2011, MNRAS, 412, L113

Coccato, L., Morelli, L., Pizzella, A., et al. 2013, A&A, 549, A3

Corsini, E. M. 2014, ASPCS 486, Multi-Spin Galaxies, ed. E. Iodice, & Corsini E. M. (San Francisco, CA: PASP), 51

Davis, T. A., Alatalo, K., Sarzi, M., et al. 2011, MNRAS, 417, 882

Dehnen, W. 2001, MNRAS, 324, 273

de Vaucouleurs G., de Vaucouleurs A., Corwin, H. G. Jr., et al. 1991, Third Reference Catalogue of Bright Galaxies (New York, NY: Springer)

di Teodoro, E. M., & Fraternali, F. 2014, A&A, 567, A68

Duc P.-A., Cuillandre, J.-C., Serra, P., et al. 2011, MNRAS, 417, 863

Evans, N. W., & Collett, J. L. 1994, ApJ, 420, L67

Fisher, D., Illingworth, G., & Franx, M. 1994, AJ, 107, 160

Galletta, G. 1987, ApJ, 318, 531

Galletta, G. 1996, IAUC 157, Barred Galaxies, ed. R. Buta, D. A. Crocker, & B. G. Elmegreen, (San Francisco, CA:ASP), 429

Gerhard, O. E. 1993, MNRAS, 265, 213

Greengard, L., & Rokhlin, V. 1997, JCoPh, 135, 280

Haynes, M. P., Jore, K. P., Barrett, E. A., Broeils, A. H., & Murray, B. M.

2000, AJ, 120, 703

Hockney, R. W., & Eastwood, J. W. 1988, Computer simulation using particles (Bristol: Hilger)

Hohl, F. 1978, AJ, 83, 7

Hut, P., & Bahcall, J. N. 1983, ApJ, 268, 319

Jetley, P., Gioachin, F., Mendes, C., Kale, L. V., & Quinn., T. R. 2008, IEEE International Parallel and Distributed Processing Symp. 2008, Massively parallel cosmological simulations with ChaNGa (Whashington, DC: IEEE Computer Society)

Jetley, P., Wesolowski, L., Gioachin, F., Kale, L. V., & Quinn, T. R. 2010, 2010 ACM/IEEE International Conference for High Performance Computing, Networking, Storage and Analysis, Scaling Hierarchical N-body Simulations on GPU Clusters (Washington, DC: IEEE Computer Society)

Johnston, E. J., Merrifield, M. R., Aragón-Salamanca, A., & Cappellari, M. 2013, MNRAS, 428, 1296

Jore, K. P., Broeils, A. H., & Haynes M. P., 1996, AJ, 112, 438

Kannappan, S. J., & Fabricant, D. G. 2001, AJ, 121, 140

Katz, N. 1992, ApJ, 391, 502

Kaviraj, S., Peirani, S., Khochfar, S., Silk, J., & Kay, S. 2009, MNRAS, 394, 1713

Kennicutt, R. C. 1998, ApJ, 498, 541

Knebe, A., Green, A., & Binney, J. 2001, MNRAS, 325, 845

Kuijken, K., & Dubinski, J. 1994, MNRAS, 269, 13

Kuijken, K., & Dubinski, J. 1995, MNRAS, 277, 1341

Kuijken, K., Fisher, D., & Merrifield, M. R. 1996, MNRAS, 283, 543

Lovelace, R. V. E., & Chou, T. 1996, ApJ, 468, L25

Mac Low, M.-M., & Ferrara, A. 1999, ApJ, 513, 142

Mapelli, M., Rampazzo, R., & Marino, A. 2015, A&A, 575, A16

Menon, H., Wesolowski, L., Zheng, G., et al. 2015, ComAC, 2, 1

Merrifield, M. R., & Kuijken, K. 1994, ApJ, 432, 575

Monaghan, J. J. 1992, ARA&A, 30, 543

Moore, B., Quinn, T. R., Governato, F., Stadel, J., & Lake, G. 1999, MNRAS, 310, 1147

Navarro, J. F., Frenk, C. S., & White, S. D. M. 1996, ApJ, 462, 563

Pizzella, A., Corsini, E. M., Vega Beltrán, J. C., & Bertola, F. 2004, A&A, 424, 447

Pizzella, A., Morelli, L., Corsini, E. M., et al. 2014, A&A, 570, A79

Puerari, I., & Pfenniger, D. 2001, Ap&SS, 276, 909

Querejeta, M., Eliche-Moral, M., Tapia, T. et al 2015, Galax, 3, 202

Quinn, T., Katz, N., Stadel, J., & Lake, G. 1997, arXiv:astro-ph/9710043

Rix, H-W., Franx, M., Fisher, D., & Illingworth, G. 1992, ApJ, 400, L5

Rix, H-W. R., Kennicutt, R. C., Braun R., & Walterbos, R. A. M. 1995, ApJ, 438, 155

Rubin, V. C., Graham, J. A., & Kenney, J. D. P. 1992, ApJ, 394, L9

Rubin, V. C. 1994a, AJ, 107, 173

Rubin, V. C. 1994b, AJ, 108, 456

Salim, S., Fang, J. J., Rich, R. M., Faber, S. M., & Thilker, D. A. 2012, ApJ, 755, 105

Sancisi, R., Fraternali, F., Oosterloo, T., & van der Hulst, T. 2008, A&ARv, 15, 189

Sandage, A., & Tammann, G. A. 1981, A Revised Shapley-Ames Catalog of

Bright Galaxies (Washington, DC: Carnegie Institution of Washington Publ.)

Schmidt, M. 1959, ApJ, 129, 243

Sérsic, J. L. 1963, BAAA, 6, 41

Silćhenko, O. K., Moiseev, A. V., & Shulga, A. P. 2010, ApJ, 140, 1462

Stadel, J. G. 2001, Ph.D. Thesis, University of Washington

Steinmetz, M. 1996, MNRAS, 278, 1005

Stinson, G., Seth, A., Katz, N., et al. 2006, MNRAS, 373, 1074

Sutherland, R. S., & Dopita, M. A. 1993, ApJS, 88, 253

Terzić, B., & Graham, A. W. 2005, MNRAS, 362, 197

Teyssier, R. 2002, A&A, 385, 337

Thakar, A. R., & Ryden, B. S. 1996, ApJ, 461, 55

Thakar, A. R., Ryden, B. S., Jore, K. P., & Broeils, A. H. 1997, ApJ, 479, 702

Thakar, A. R., & Ryden, B. S. 1998, ApJ, 506, 93

Vergani, D., Pizzella, A., Corsini, E. M., et al. 2007, A&A, 463, 883

Wadsley, J. W., Stadel, J., & Quinn, T. R. 2004, NewA, 9, 137

Widrow, L. M., & Dubinski, J. 2005, ApJ, 631, 838

Widrow, L. M., Pym, B., & Dubinski, J. 2008, ApJ, 679, 1239

Wielen, R. 1974, HiA, 3, 395

Wozniak, H., & Pfenniger, D. 1997, A&A, 317, 14

Yildirim, A., van den Bosch, R. C. E., van de Ven, G., et al. 2016, MNRAS, 456, 538